Final Technical Report

Full 3-D Waveform Tomography and Rapid Seismic Source Parameter Inversion for San Francisco Bay Region

PI: Po Chen
Department of Geology and Geophysics, University of Wyoming
Laramie, Wyoming 82071
Phone: (307)-766-3086
Email: pchen@uwyo.edu

Award Number: G10AP00032

Award Amount: $142,130

Award Duration: January 2010 through December 2014

Abstract

In this project, full-3D seismic waveform tomography (F3DT) has been successfully applied to image the crustal and upper-most mantle structure in Northern California. The 3D starting model NCF3D00 was created by embedding the 3D USGS Bay Area seismic velocity model inside the regional 3D ray-travel-time tomography model of Lin et al. (2010). A discontinuous-mesh finite-difference code was used to carry out the wave-propagation simulations for generating synthetic seismograms and the 3D sensitivity kernels. The inversion utilized both seismograms generated by local small to medium-sized earthquakes and also the ambient-noise Green's functions retrieved by cross-correlating and stacking ambient-noise recordings from local seismic networks, USArray TA stations and temporary PASCAL deployments. The misfits between observed seismograms and the corresponding synthetic seismograms were quantified using frequency-dependent phase and amplitude measurement. The inversion was carried out using a combination of the adjoint-wavefield method (F3DT-AW), which back-propagates the misfit information from the receivers to image the earth structure, and the scattering-integral method (F3DT-SI), which explicitly sets up the approximate Hessian of the objective function and solves the optimization problem using the Gauss-Newton algorithm. At the current stage, 9 iterations have been carried out. The first 5 iterations were based on F3DT-AW and the last 4 iterations were based on F3DT-SI. The updated model, NCF3D09, reveals many 3D small-scale structural features in the crust. Deep-seated large-scale 3D structural features are imaged with more clarity. In general, NCF3D09 is highly consistent with previous 3D models obtained using ray-theoretic methods. In addition to P-wave velocity, NCF3D09 provide also the S-wave velocity and the Poisson's ratio, which might be useful for a more thorough interpretation. The velocity models in NCF3D09 appear to have good correlation with known fault systems in Northern California, which is still under examination.

1. Introduction

Northern California (NC) is a region with high seismic risk (WGCEP, 2003; Field, 2007). Physics-based seismic hazard analysis aims to quantify ground motion from potential damaging earthquakes through computer simulations of earthquake rupture and dynamic wave-propagation processes. To carry out these simulations, we need a seismic velocity model. Experiences from past large earthquakes, such as the Northridge earthquake and the Kobe earthquake, have underscored the importance of 3D variations of the seismic velocities in controlling the propagation and amplification of seismic waves. Previous studies have demonstrated the importance of mapping out 3D seismic structures, in particular deep sedimentary basins, for strong ground-motion predictions (e.g., Olsen & Archuleta, 1996; Iwata et al., 1996; Pitarka et al., 1996; Kawase, 1996; Hartzell et al., 1997; Wald & Graves, 1998; Graves et al., 1998). The purpose of this study is to develop a detailed 3D crustal seismic velocity model for NC through full-3D seismic waveform tomography (F3DT).

Seismic tomography has been one of the most effective means for imaging the internal structure of the Earth in the past few decades and F3DT represents the latest development in seismic tomography techniques. F3DT removes the high-frequency approximation in the conventional ray-theoretic travel-time tomography (e.g., Cerveny, 2001) and finite-frequency tomography based on paraxial (asymptotic) ray theory (e.g., Dahlen et al., 2000). It accounts for the physics of wave propagation by solving the 3D (visco)elastic wave equation using purely numerical methods, such as finite-difference (e.g., Graves, 1996; Olsen, 1994), finite-element (e.g., Bao et al., 1998), spectral-element (e.g., Komatisch & Tromp, 1999) and discontinuous-Galerkin (e.g., Kaser et al., 2006) methods. It allows the entire seismogram, including body waves, surface waves and any classic seismic phases, to be utilized in the inversion in a unified theoretical and computational framework. The nonlinearity in the structural inversion is accounted for through iterations. Seismic waveform observations are assimilated into the 3D seismic velocity model through an iterative cycle of quantifying the misfits between observed and model-predicted (synthetic) seismograms, calculating the sensitivity (Fréchet) kernels, inverting the misfits for perturbations to the seismic velocity model and updating the seismic velocity model. This iterative cycle is highly similar to the variational data assimilation technique that has been driving rapid progresses in atmospheric and ocean sciences (e.g., Chen, 2011).

In a previous study, my student and I have successfully applied F3DT to construct a 3D crustal seismic velocity model for Southern California and our model is named “CVM-S4.26” (Lee et al., 2014ab). This model brings out many 3D small-scale structural features that were not imaged in previous crustal-scale tomography studies. Synthetic seismograms computed using CVM-S4.26 provide substantially better fit to observed waveforms for frequencies up to 0.2 Hz than the other two regional seismic velocity models, CVM-S4 and CVM-H11.9 (Lee et al., 2014ab). In the past few years, my students and I have been applying F3DT to NC with a few modifications to the methodology. The purpose of the modifications was to accommodate the highly uneven distributions of seismic sources and stations in NC and also to account for the multi-scale

nature of the seismic velocity model. To address issues related to the uneven distribution of useful broadband waveform data, we are placing more emphasis on ambient-noise Green's functions retrieved from both CISN stations and the transportable array (TA) stations. To address the multi-scale problem, we are using two different meshes: a uniform mesh with 500-m grid spacing for structures above 40 km and a uniform mesh with 1500-m grid spacing for structures below 40 km and above 96 km.

2. Methodology

F3DT is usually implemented using gradient- and/or Hessian-based iterative optimization algorithms. The discretized earth structural model **m** is iteratively updated through a finite series of perturbations,

$$\mathbf{m}_{k+1} = \mathbf{m}_k + \Delta\mathbf{m}_k,\ k = 0,1,2,\ldots,K \tag{1}$$

where k is the iteration index. The perturbation for the kth iteration, $\Delta\mathbf{m}_k$, is obtained using either the scattering-integral method (F3DT-SI) or the adjoint-wavefield method (F3DT-AW). At the current stage, we have carried out 9 iterations for our NC F3DT inversion. The first 5 iterations were carried out using F3DT-AW and the last 4 iterations were carried out using F3DT-SI.

2.1 F3DT-SI

In F3DT-SI, $\Delta\mathbf{m}_k$, is obtained by minimizing an objective function of the following form,

$$\chi^2\left(\mathbf{m},\mathbf{m}_k\right) = \mathbf{d}^T\left(\mathbf{m},\mathbf{m}_k\right)\mathbf{C}_d^{-1}\mathbf{d}\left(\mathbf{m},\mathbf{m}_k\right) + \left(\mathbf{m}-\mathbf{m}_k\right)^T\mathbf{C}_m^{-1}\left(\mathbf{m}-\mathbf{m}_k\right), \tag{2}$$

where **m** is the "target" structural model, $\mathbf{d}\left(\mathbf{m},\mathbf{m}_k\right)$ is a column-vector composed of misfit measurements that quantify the discrepancies between the ith-component observed seismogram generated by the sth seismic source and recorded at the rth receiver, $\bar{u}_i^s\left(\mathbf{x}_r,t\right)$, and the corresponding synthetic seismogram $u_i^s\left(\mathbf{x}_r,t\right)$ computed using the latest structural model $\mathbf{m}_k$, $\mathbf{C}_d$ and $\mathbf{C}_m$ are respectively the data and model covariance matrices. The objective function in eq. (2) is minimized using the Gauss-Newton algorithm, which requires the solution of the following Gauss-Newton normal equation

$$\begin{bmatrix} \mathbf{C}_d^{-1/2}\mathbf{A}_k \\ \mathbf{C}_m^{-1/2} \end{bmatrix}\Delta\mathbf{m}_k = \begin{bmatrix} \mathbf{C}_d^{-1/2}\mathbf{d}_k \\ \mathbf{0} \end{bmatrix}, \tag{3}$$

where $\mathbf{A}_k = \partial\mathbf{d}_k/\partial\mathbf{m}_k$ is the Jacobian matrix for the kth iteration. In F3DT-SI, the Jacobian matrix is explicitly constructed and equation (3) is solved using an optimized LSQR algorithm (Lee et al., 2013).

Each row of the Jacobian matrix is a data sensitivity (Fréchet) kernel of one misfit measurement with respect to the structural model. Equations for constructing the data sensitivity kernels using the RSGTs have been given in (e.g., Zhao et al., 2005; Zhao et al., 2006; Chen et al., 2007ab; Chen & Lee, 2015). For an isotropic elastic earth structural model parameterized using the two Lamé parameters, $\lambda(\mathbf{x})$ and $\mu(\mathbf{x})$, the data sensitivity kernels are given by

$$K_{d^{sn}}^{\ln\lambda}(\mathbf{x}) = -\lambda(\mathbf{x})\int_V \mathrm{d}V(\mathbf{x}')\int_0^T \mathrm{d}t\mathbf{J}_{sn}(\mathbf{x}',t)\cdot\left\{\left[\nabla\cdot\mathbf{G}(\mathbf{x},t;\mathbf{x}',0)\right]*\left[\nabla\cdot\mathbf{u}^s(\mathbf{x},t)\right]\right\}, \tag{4}$$

$$K_{d^{sn}}^{\ln\mu}(\mathbf{x}) = -\mu(\mathbf{x})\int_V \mathrm{d}V(\mathbf{x}')\int_0^T \mathrm{d}t\mathbf{J}_{sn}(\mathbf{x}',t)\cdot\left\{\nabla\mathbf{G}(\mathbf{x},t;\mathbf{x}',0):\left[\nabla\mathbf{u}^s(\mathbf{x},t)+\left(\nabla\mathbf{u}^s(\mathbf{x},t)\right)^T\right]\right\}, \tag{5}$$

where s is the source index, n is the measurement index, $\mathbf{J}_{sn}(\mathbf{x}',t)$ is the wavefield perturbation kernel (WPK) of the misfit measurement d_{sn} with respect to the synthetic wavefield from the sth source $\mathbf{u}^s(\mathbf{x},t)$, $\mathbf{G}(\mathbf{x},t;\mathbf{x}',0)$ is the Green's tensor for a point impulsive source located at $\mathbf{x}'$, "$*$" represents temporal convolution and ":" represents double-contraction with temporal convolution. The calculation of the data sensitivity kernels therefore involves the spatial gradients of the Green's tensor from $\mathbf{x}'$ to $\mathbf{x}$, $\mathbf{G}(\mathbf{x},t;\mathbf{x}',0)$, and the spatial gradients of the forward wavefield from the sth source to $\mathbf{x}$, $\mathbf{u}^s(\mathbf{x},t)$. In practice, the WPK can often be written as

$$\mathbf{J}_{sn}(\mathbf{x}',t) = \mathbf{J}'_{sn}(t)\delta(\mathbf{x}'-\mathbf{x}_r), \tag{6}$$

where $\delta(\mathbf{x}'-\mathbf{x}_r)$ is the Dirac delta function centered at the location of the rth receiver $\mathbf{x}_r$. The spatial integral over $\mathbf{x}'$ is then resolved to replacing $\mathbf{G}(\mathbf{x},t;\mathbf{x}',0)$ with $\mathbf{G}(\mathbf{x},t;\mathbf{x}_r,0)$, which can be computed by placing a point impulsive source at the receiver location. Since the spatial gradients of the displacement field are the strain fields, the spatial gradients of $\mathbf{G}(\mathbf{x},t;\mathbf{x}_r,0)$ are named receiver-side strain Green's tensor (RSGT) in (Zhao et al., 2006). To construct the data sensitivity kernels for all misfit measurements, it is therefore necessary to store either the RSGTs of all receivers or the forward strain fields from all seismic sources. In passive-source F3DT problems, seismic sources often outnumber receivers; therefore it is more economical to store the RSGTs. The stored RSGTs can also be highly useful for very rapid seismic source parameter inversions (Chen et al., 2005; Zhao et al., 2006; Chen et al., 2010; Lee et al., 2011).

One drawback of F3DT-SI is its high disk storage cost for archiving the RSGTs and the associated I/O overhead. This cost can be significant in realistic F3DT applications involving many receivers. In Lindstrom et al. (2015), we show that by integrating a lossy compressor, code named "zfp", into our wave-propagation simulation code, we were able to reduce the RSGT disk storage by at least an order of magnitude and also improve the overall I/O performance significantly, thereby opening up the possibilities of

implementing F3DT-SI on small to medium-sized computer clusters that are not equipped with large fast disk arrays and powerful I/O sub-systems.

2.2 F3DT-AW

In the F3DT-AW, the adjoint wave-field for seismic source *s* can be expressed as,

$$\left[u_s^j\right]^\dagger(\mathbf{x},\tau) = \int dt \sum_{rin} G_{ji}\left(\mathbf{x},\tau - t;\mathbf{x}_r\right) J_{srn}^i(-t) d_{srn}^i \ . \tag{7}$$

This adjoint wave-field can be constructed without explicitly computing the receiver Green's tensor. In fact, if we solve the adjoint wave equation, which turns out to be identical to the forward wave equation under certain circumstances (e.g., Tarantola, 1989), using the adjoint source field, which is defined as

$$\left[f_s^i\right]^\dagger(\mathbf{x},t) = \sum_{rn} J_{srn}^i(-t) d_{srn}^i \delta\left(\mathbf{x} - \mathbf{x}_r\right), \tag{8}$$

the result is identical to the adjoint wave-field as expressed in equation (7). The adjoint source field is obtained by placing the time-reversed and misfit-weighted wavefield perturbation kernels at the receiver locations. Once the adjoint wave-field for the source *s* is obtain, the source-specific kernels with respect to density and elastic moduli can be computed as

$${}_sK_\chi^\rho(\mathbf{x}) = -\int d\tau \sum_j \partial_\tau^2 u_s^j(\mathbf{x},\tau)\left[u_s^j\right]^\dagger(\mathbf{x},-\tau) = -\int d\tau \sum_j \partial_\tau u_s^j(\mathbf{x},\tau)\partial_\tau\left[u_s^j\right]^\dagger(\mathbf{x},-\tau), \tag{9}$$

$${}_sK_\chi^{c_{jklm}}(\mathbf{x}) = -\int d\tau\, \partial_l u_s^m(\mathbf{x},\tau)\partial_k\left[u_s^j\right]^\dagger(\mathbf{x},-\tau). \tag{10}$$

And the gradients of the objective function can be obtained by summing the source-specific kernels over all sources used in a dataset,

$$K_\chi^\rho(\mathbf{x}) = \sum_{s=1}^{N_s} {}_sK_\chi^\rho(\mathbf{x}), \tag{11}$$

$$K_\chi^{c_{jklm}}(\mathbf{x}) = \sum_{s=1}^{N_s} {}_sK_\chi^{c_{jklm}}(\mathbf{x}). \tag{12}$$

In practice, the gradients computed in equations (11)-(12) are smoothed using a model covariance operator (e.g., Tape et al., 2009; Fichtner et al., 2009; Chen, 2011; Chen & Lee, 2015) before used in a conjugate-gradient algorithm or any other types of gradient-based optimization algorithms to minimize the objective function.

We denote the discretized and smoothed gradients as column vectors $\mathbf{K}^{\rho}$ and $\mathbf{K}^{c_{jklm}}$. The gradient vectors for different types of model parameters can be concatenated into a single column vector, which we denote as **K**. In a typical conjugate-gradient algorithm, the descent direction at the current iteration (i.e., iteration k), which we denote as $\mathbf{P}_k$, is computed from the descent direction at the previous iteration $\mathbf{P}_{k\text{-}1}$ and the gradient of the current iteration $\mathbf{K}_k$ as

$$\mathbf{P}_k = -\mathbf{K}_k + \beta_k \mathbf{P}_{k-1}, \tag{13}$$

where β_k is a scalar computed from the gradients of the previous and current iterations. There are a variety of formulas for computing β_k (Press et al., 1992). One of the most widely-used formulas, the Fletcher-Reeves' formula (Press et al., 1992), which is also used in our implementation, is

$$\beta_k = \frac{\mathbf{K}_k^T \mathbf{K}_k}{\mathbf{K}_{k-1}^T \mathbf{K}_{k-1}}, \tag{14}$$

where superscript T represents the transpose. Once the descent direction is obtained, a line search is performed to find the optimal step length α_k to walk in the descent direction. In practice, a quadratic interpolation is sufficient for finding the optimal step length. Once the line search is completed, the earth structure model vector **m** can be updated to the next iteration using the $\Delta\mathbf{m}_k$,

$$\Delta\mathbf{m}_k = \alpha_k \mathbf{P}_k, \tag{15}$$

and the algorithm proceeds until a pre-specified convergence criterion is met. There are several variations of equation (14) for computing β_k and each variation has its own strengths and weaknesses (Chen & Lee, 2015). In our NC F3DT inversion, we found that equation (14) gave sufficient misfit reductions for the first 5 iterations; therefore we did not implement the other variations.

2.3 Wave-equation solver

The synthetic seismograms used for computing the waveform misfits with the observed seismograms and also the data sensitivity kernels and the forward/adjoint wave-propagation simulations in F3DT-SI and F3DT-AW were carried out using our parallelized discontinuous-mesh fourth-order staggered-grid finite-difference code, which solves the 3D (visco)elastic wave-equation in the space-time domain.

For many earth structure models, the minimum S-wave speed close to the surface of the earth can be much smaller than that at larger depths. If this is the case, using a discontinuous mesh with finer grid in the upper part of the model and a coarser grid in the lower part of the model may significantly improve computational efficiency without sacrificing simulation accuracy.

Our finite-difference wave-equation solver uses the discontinuous grid to improve computational efficiency. In our implementation, we divide the whole computational domain into two separate layers (Figure 1). The upper layer uses a small grid to represent the near-surface part of the computational domain in order to maintain high accuracy, while the bottom layer uses a grid size that is three times as large. To avoid numerical instability caused by the discontinuity in the mesh, we increase the grid size along the *z*-axis smoothly (following a linear relation with depth) from the top layer to the bottom layer. The grid spaces in the two horizontal axes are tripled at the grid interface.

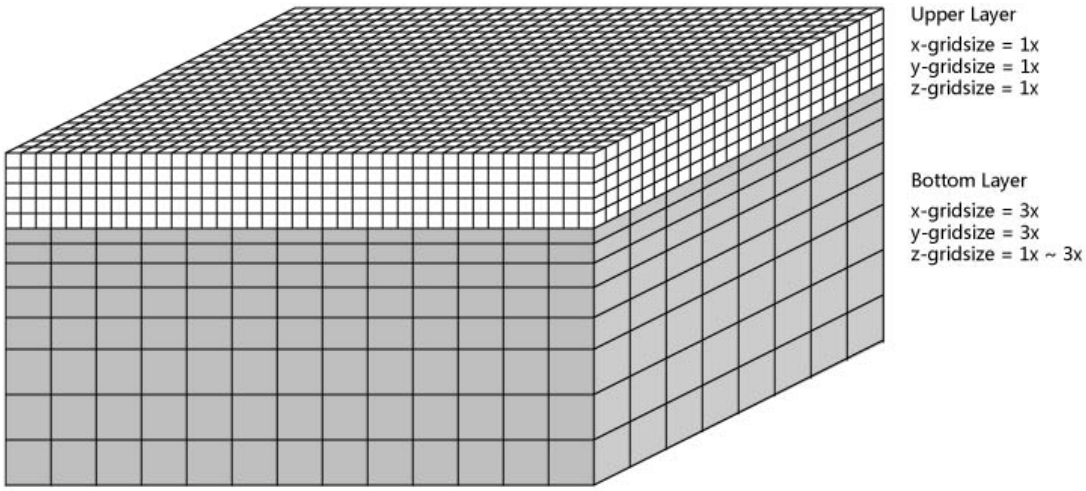

Figure 1. The dual-layered designed grid. The upper layer has a uniform, standard grid size in all three dimensions. The bottom layer's grid size is uniform only on its *x*- and *y*-axes, whose gradations are three times the size of those of the standard grid; along its *z*-axis, the grid size increases gradually from the standard grid size to the 3x size of the *x*- and *y*-axes.

As shown in Figure 2, the white squares are the grid points located in the upper layer and the grey square are the grid point located in the bottom layer. Those white squares with dash line are the grid points where we need to interpolate field variables. Through experimentation and extensive numerical tests, we have found that the 2D Bessel interpolation (Pengcheng Liu, personal communications; Triebel, 1978) gave us a stable and accurate discontinuous-mesh staggered-grid finite-difference scheme.

The conventional split-field perfectly matched layer (PML) boundary condition may not be effective for waves that are propagating at grazing angles. An effective remedy of this problem is to use the convolutional-PML (CPML) boundary condition. The CPML technique that we implemented in our FD code was introduced in Komatitsch & Martin, (2007), which was based on a previous study by Roden & Gedney (2000). The key feature of this scheme is that it is effective for waves propagating in all directions. The CPML scheme is easier to implement than the classical split-field PML, since we do not need to split the equations into parallel and perpendicular directions.

At the current stage, we have implemented and tested our parallel discontinuous-mesh finite-difference code for solving the 3D (visco)elastic wave equation on conventional CPU clusters. We have also successfully ported our codes to a GPU cluster and obtained a speedup of about 30. The NC F3DT inversion is still being carried out using our parallel CPU implementation.

Figure 2. The structure of discontinuous grid, those white squares represent the grid point located in the finer layer, while the grey square represents those grid point located in the coarser layer. Those white squares with dash line represent those grid points needed to be interpolated.

3. Data

Our F3DT inversion in Southern California (Lee et al., 2014ab) has shown that ambient-noise Green's functions (ANGF) obtained by cross-correlating and stacking noise recordings at station pairs can be used in F3DT inversions just like earthquake waveform

recordings. We have applied the technique of Bensen et al. (2007) to a set of ambient-noise data recorded by the USArray Transportable Array (TA) stations, the Berkeley Digital Seismic Network (BK) stations, and the PASSCAL stations deployed for the Sierra Nevada EarthScope Project (XE) (Figure 3) to extract ANGF data. The vertical-component continuous-time recordings for years 2006 and 2007 from those stations were downloaded from the IRIS data center and the Northern California Seismic Network. The yearly data were divided into about 8760 hour-long segments and then band-pass filtered to between 0.01 Hz and 5 Hz. To remove effects of earthquakes, we applied the running-absolute-mean normalization (Bensen et al., 2007) to the noise recordings. The cross-correlation and stacking processes were carried out in the frequency domain and the stacked cross-correlations back to the time-domain. The resulting cross-correlations are two-sided time functions with both positive and negative time lags and we converted the two-sided signals to one-sided signals by averaging the time-reversed acausal parts and the causal parts. Examples of our ANGF between TA station O07A and 48 other stations used in our study are shown in Figure 4. The coherent surface wave energy has an average group-velocity of about 3.3 km/s.

We have processed broadband waveform recordings from 88 earthquakes with local magnitude between 4 and 6 located within our tomography volume and occurred between year 2006 and 2015. Waveforms from many more earthquakes (>200) are still being processed and assimilated into our F3DT inversion process. As shown in Figure 5, most of the earthquakes are clustered along major faults, which is not ideal for tomography purposes. The ANGF data complements the earthquake data by providing additional path coverage in areas lacking earthquake sources. A second way for improving the sampling of the volume is to utilize as many waveforms as possible on the earthquake seismograms. The ANGF data are primarily dominated by the vertical-component Rayleigh waves. However, the earthquake seismograms have many more seismic phases usable for exacting misfit measurements. The data sensitivity kernels of those different types of seismic phases have different sampling patterns inside the 3D volume and provide independent constraints in our F3DT inversion. Our past experience in SC has shown that as the seismic velocity model improves gradually through iterations, synthetic seismograms generated using the velocity model are capable of fitting more and more waveforms on the observed seismograms. Since the waveform selection process happens in the time-domain in our F3DT workflow, the assimilation of more and more waveforms through iterations into our F3DT inversion is called “time bootstrapping”, which complements the “frequency bootstrapping” process that seeks to gradually increase the bandwidth of the waveforms through iterations.

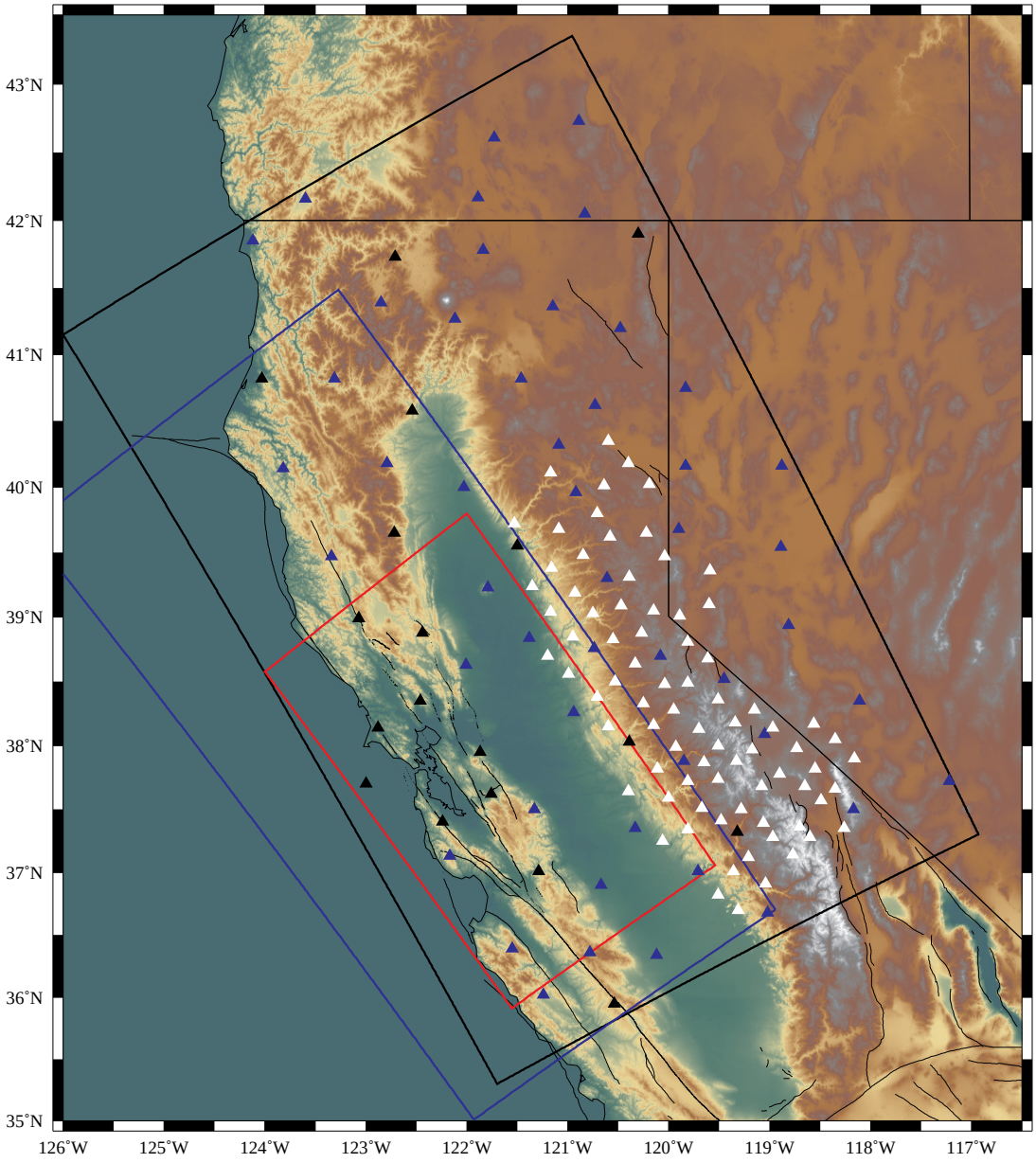

Figure 3. The geographic region of our F3DT inversion and the broadband seismic stations used in the inversion. Blue triangles: USArray Transportable Array (TA) stations; black triangles: Berkeley Digital Seismic Network (BK) stations; while triangles: PASSCAL stations in the Sierra Nevada EarthScope Project (XE). Black box: region of our F3DT inversion; blue box: region covered by the USGS Bay Area extended seismic velocity model; red box: region covered by the USGS Bay Area high-resolution model. Background color: regional topography. Black solid lines: major faults.

4. Starting Model

Our 3D starting model "NCF3D00" was constructed by embedding the 3D USGS Bay Area Velocity Model Version 08.3.0 (Brocher 2005b,a, 2008) into the 3D California statewide seismic velocity model of Lin et al. (2010). The USGS Bay Area model is based on detailed geological and geophysical mapping of the region and empirical relations for converting lithological properties to density, compressional and shear wave speeds and intrinsic attenuation quality factors. It is composed of a detailed model in the greater San Francisco Bay region with horizontal resolution of about 100 m and an extended model with horizontal resolution of about 800 m. The 3D California statewide model of Lin et al. (2010) was obtained by inverting absolute and differential *P* and *S* arrival-time picks from earthquakes, controlled sources and quarry blasts through double-difference tomography. The inversion combined a large amount of active source data and catalog phase picks from the USArray, the Northern California Earthquake Data Center and the Southern California Earthquake Data Center. The model covers the entire state of California with a horizontal grid spacing of 10 km. For grid points lying inside the USGS Bay Area extended model, the density and seismic velocities were directly extracted from the Etree database of the USGS Bay Area model. The query software allows for squashing topography/bathymetry and extracts material properties at user-specified locations. For grid points lying outside the USGS Bay Area extended model, the material properties were interpolated from the values on surrounding grid points of the 3D California statewide model using a kriging algorithm.

5. Results

Our latest 3D model for NC is named "NCF3D09". Map view slices from our latest P-velocity (Vp), S-velocity (Vs) and Poisson's ratio models are show in Figure 6, 7 and 8, respectively. I show map-view slices at 2-km to 40-km depths with 2-km interval. The 3D velocity models can be downloaded from the website: http://pochenfullwave.ddns.net. In Figure 6-8, I also show map view slices in our 3D starting model "NCF3D00" at the same depths for comparison.

In Figure 9, I show the locations of the 30 cross-sections for examining the 3D NCF3D00 and NCF3D09. The locations of these 30 cross-sections are identical to those used in Thurber et al. (2009) for examining their 3D ray-travel-time tomography Vp model. The Vs, Vp and Poisson's ratio in NCF3D00 and NCF3D09 along these 30 cross-sections are displayed on Figure 10, 11 and 12, respectively. Some of the cross-sections have points lying outside of our NC F3DT box. But those points are still within my latest California statewide F3DT model CAF3D04 and I used the velocities inside CAF3D04 for those points lying outside the NC F3DT box.

Compared with the starting model NCF3D00, the updated model NCF3D09 shows several important features. Since the starting model was merely a concatenation of the USGS Bay area model with the statewide ray-travel-time (RTT) tomography model of Lin et al. (2010), there are visible artificial discontinuities at the boundaries of the USGS Bay area model in our starting model NCF3D00. These artificial discontinuities have

largely disappeared in the updated model NCF3D09, which indicates that the F3DT inversion has mostly healed the gaps between the USGS Bay area model and the statewide RTT model.

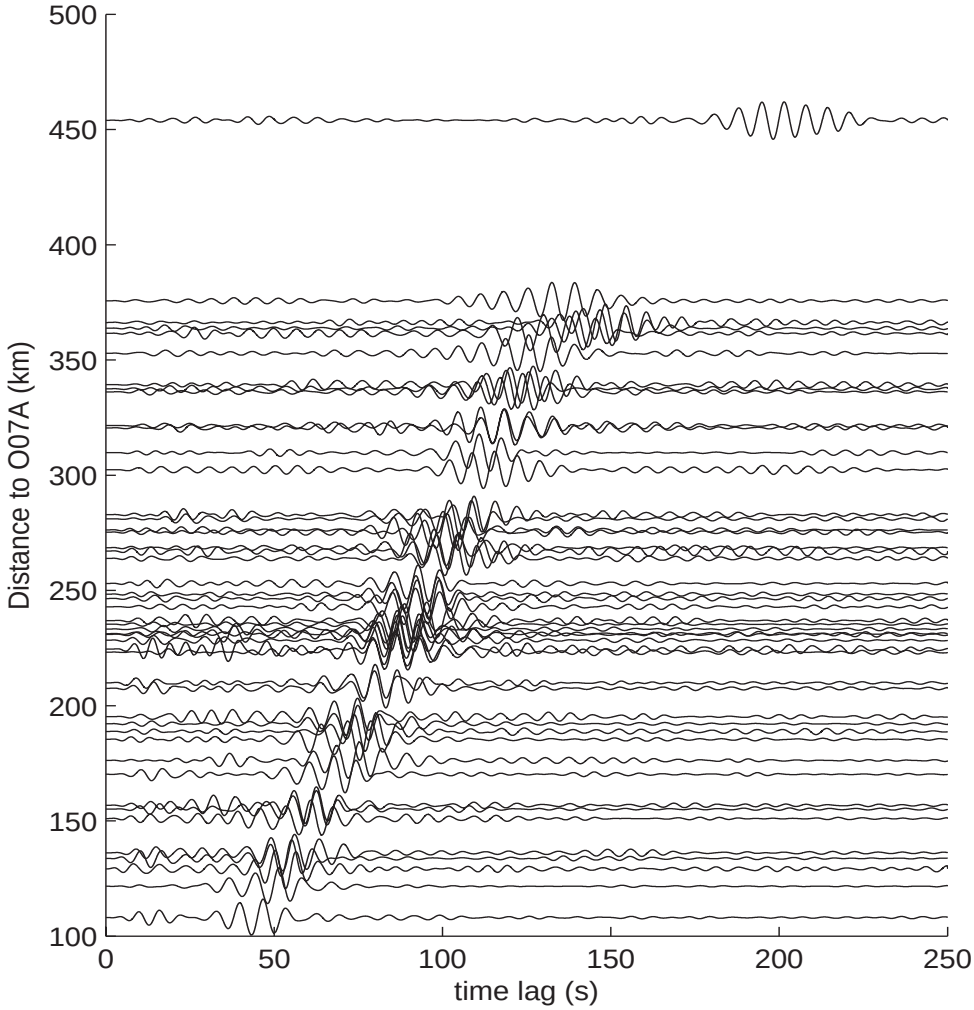

Figure 4. Examples of the ambient-noise Green's functions obtained through the procedure as described in the text. The ambient-noise Green's functions are for 48 station pairs that include the TA station O07A and are sorted according to the distance to O07A.

One distinct feature in our starting model NCF3D00 is that the velocities are mostly laterally uniform at depths greater than 8-km within the regions covered by the USGS Bay area model (Figure 6-8). In the updated model NCF3D09, significant amount of lateral variations have been introduced into these regions. The patterns of the lateral velocity variations seem to be consistent with the geology in those regions and they merge with the variations outside of those regions naturally without noticeable artificial discontinuities.

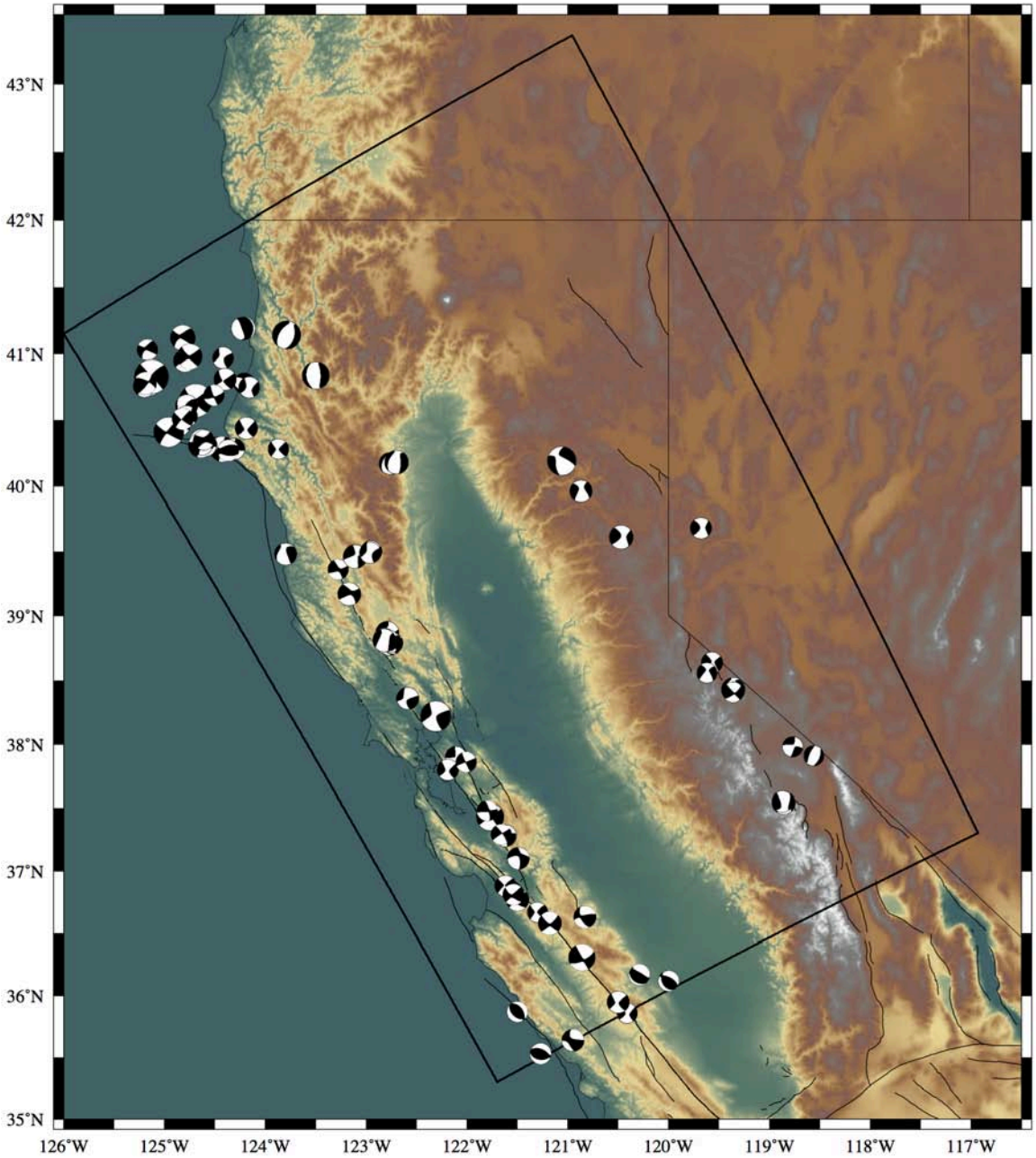

Figure 5. Centroid moment tensor (CMT) solutions for 88 earthquakes used in our F3DT inversion. The beach balls are plotted at the epicenters of the earthquakes. Major faults are shown in black solid lines. Background color shows regional topography.

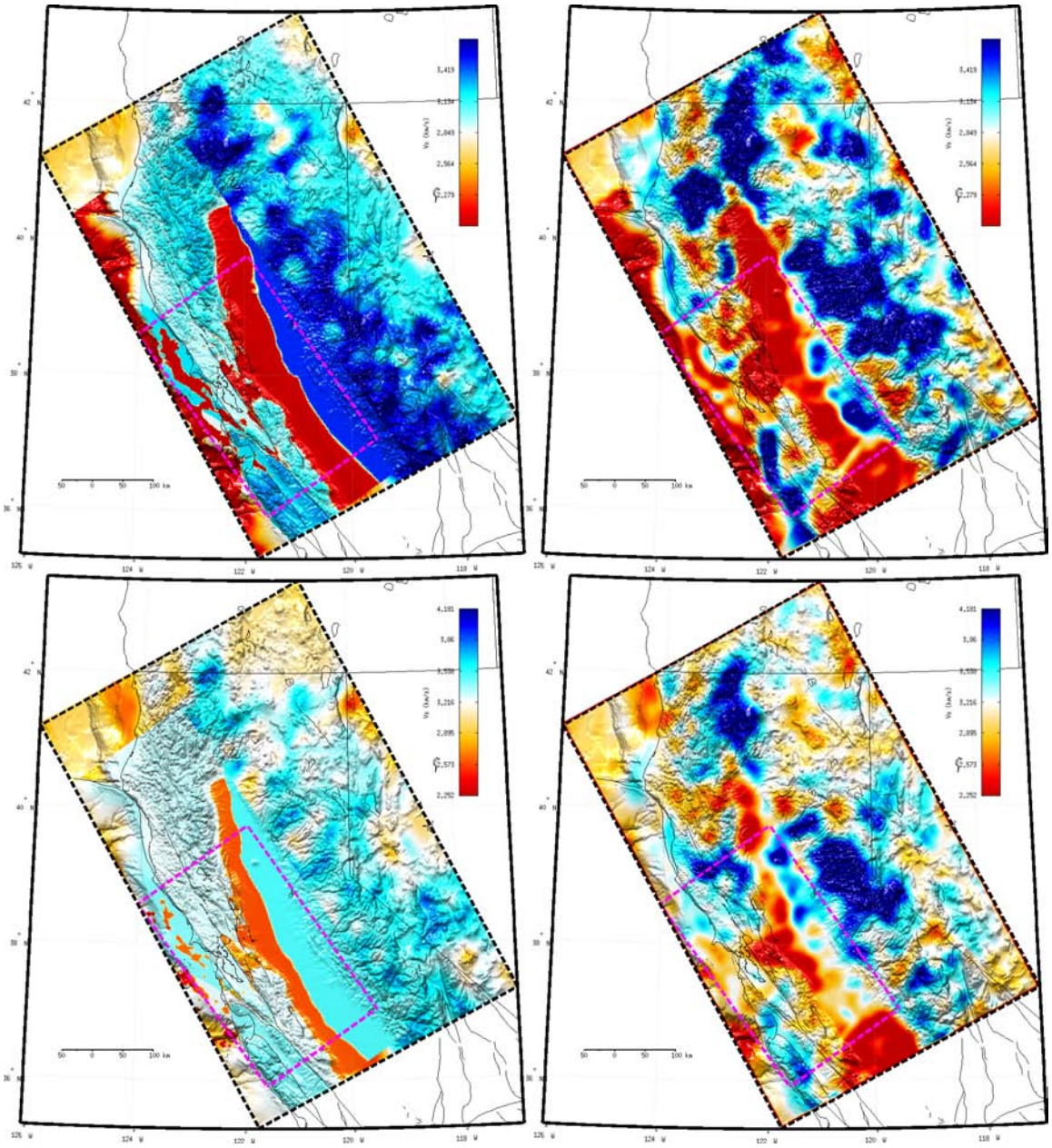

Figure 6. Map views of the 3D Vs model in our starting model NCF3D00 (left column) and the latest updated model NCF3D09 at 2-km (upper row) and 4-km (lower row) depths. Warm color: lower Vs; cold color: higher Vs; magenta dash-line box: location of the USGS Bay Area high-resolution model: black solid lines: faults, coastlines and state boundaries; background gray-scale shading: regional topography.

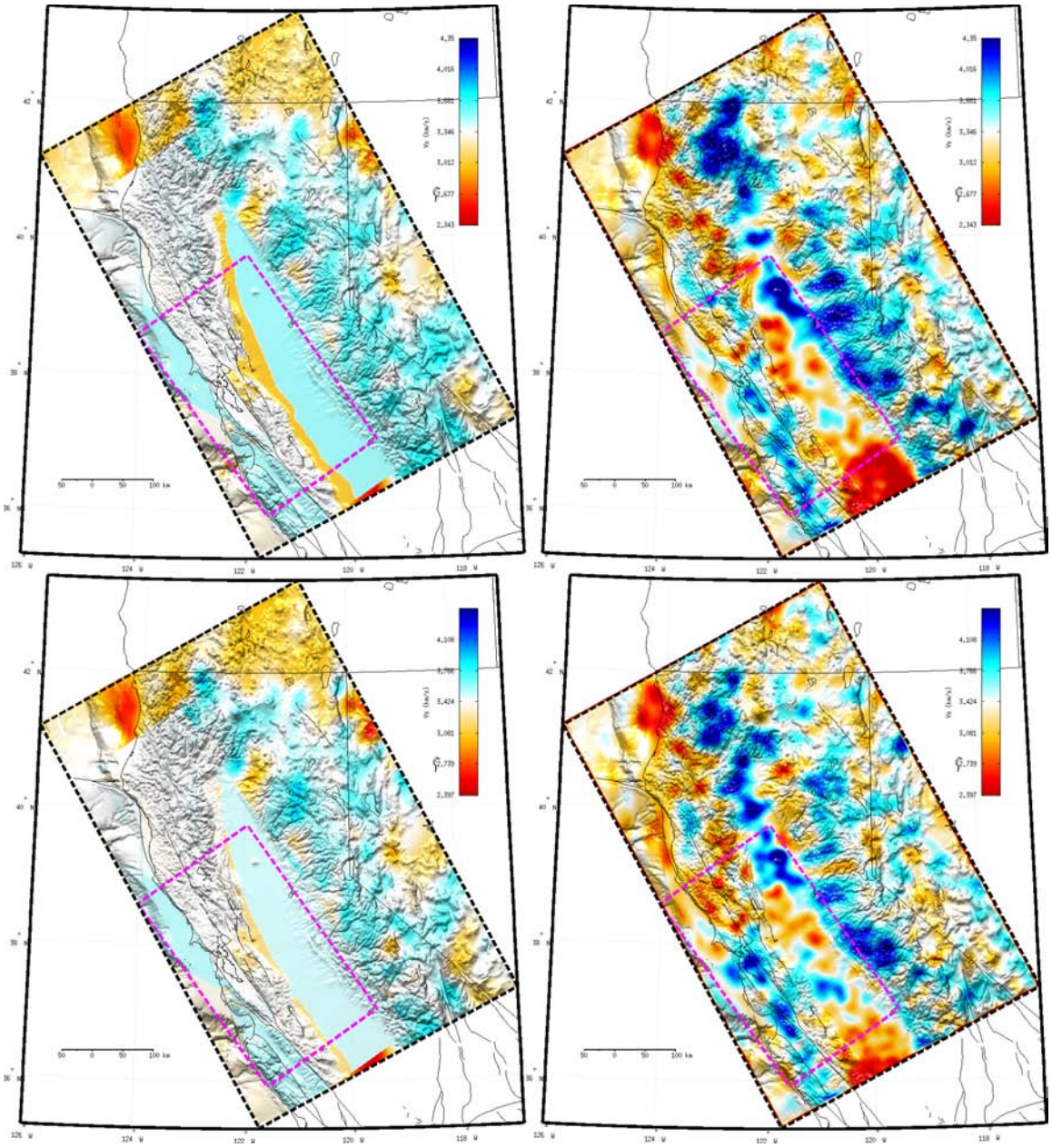

Figure 6. (continued) 6-km (upper) and 8-km (lower) depths.

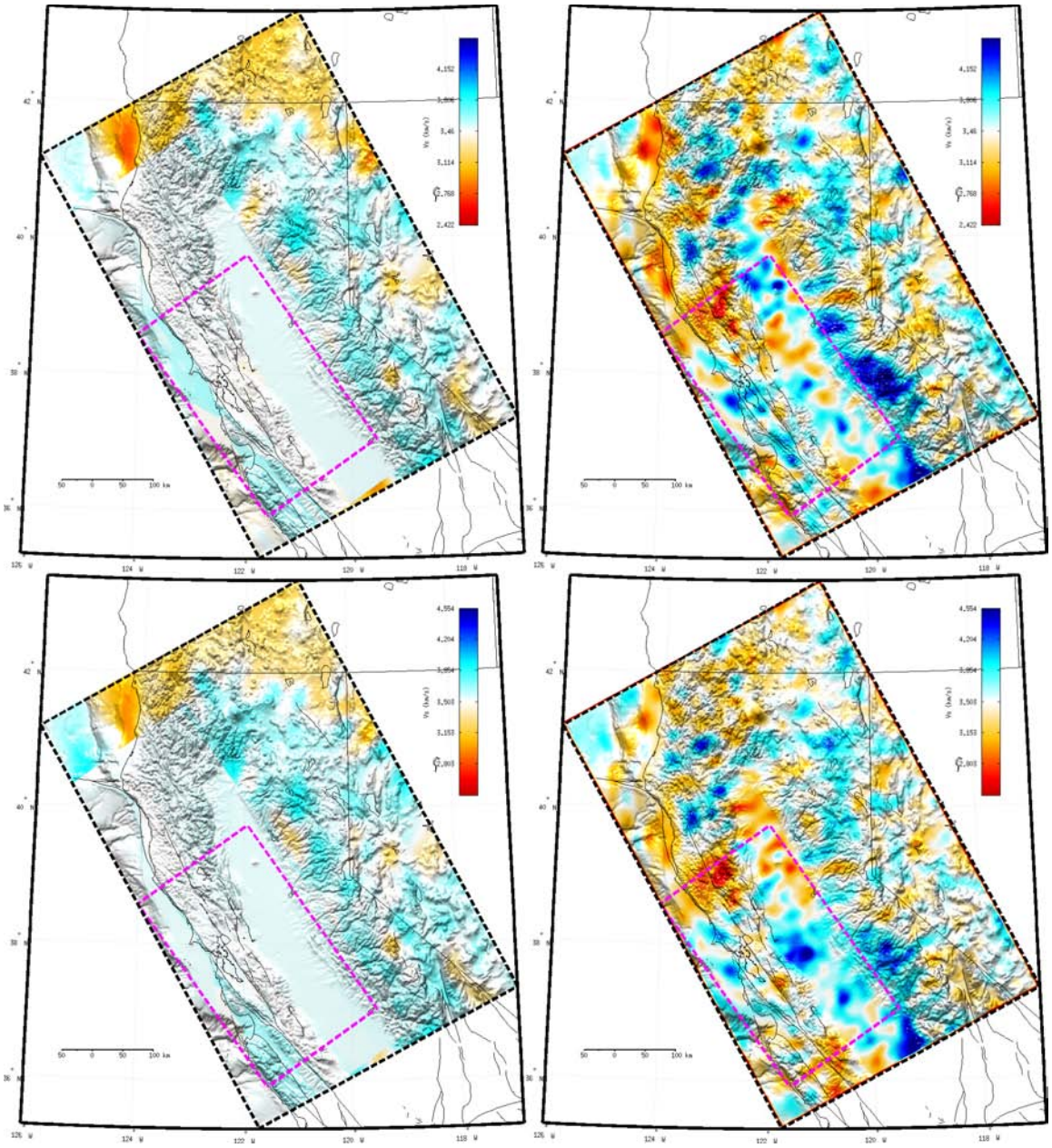

Figure 6. (continued) 10-km (upper) and 12-km (lower) depths.

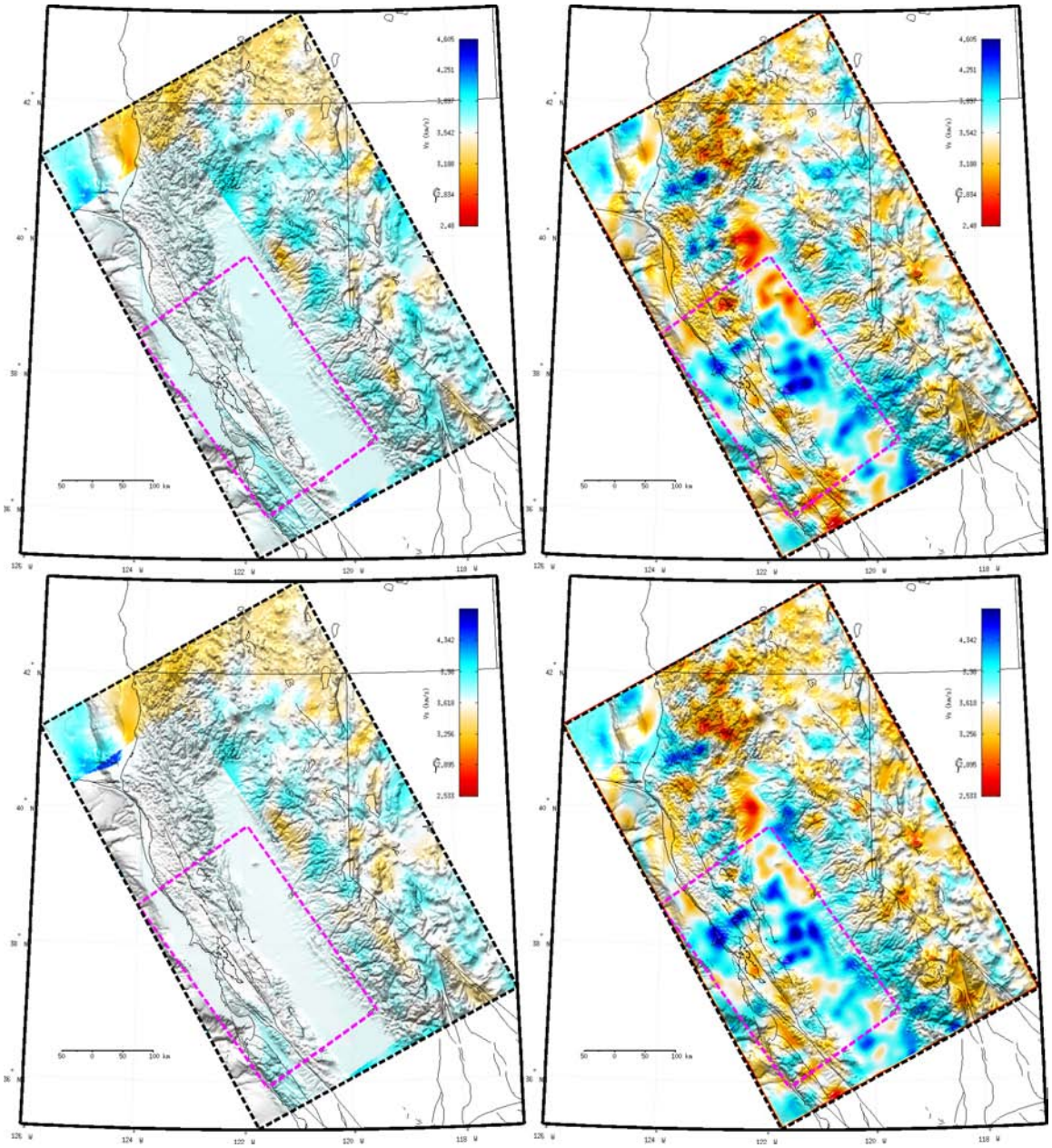

Figure 6. (continued) 14-km (upper) and 16-km (lower) depths.

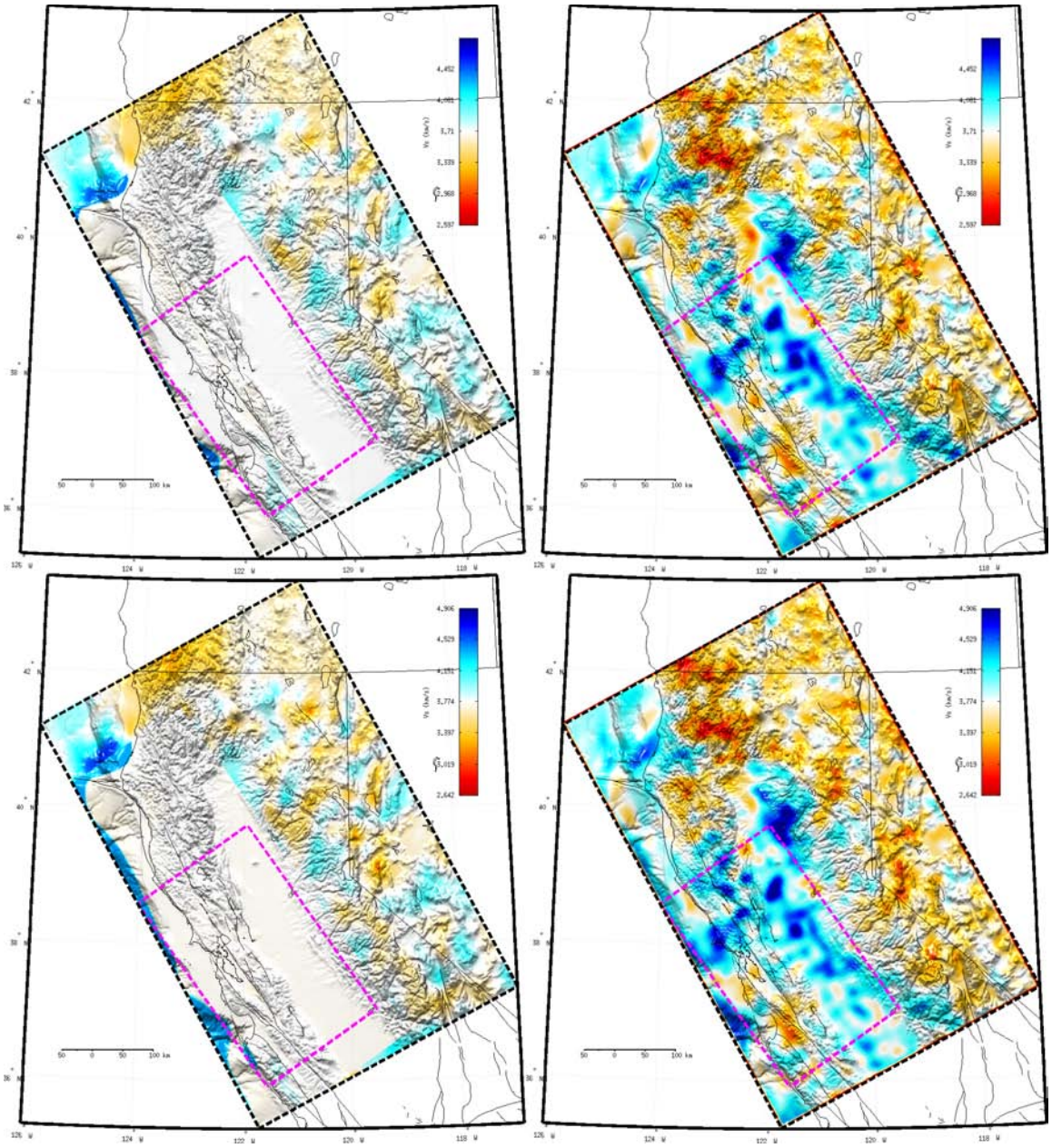

Figure 6. (continued) 18-km (upper) and 20-km (lower) depths.

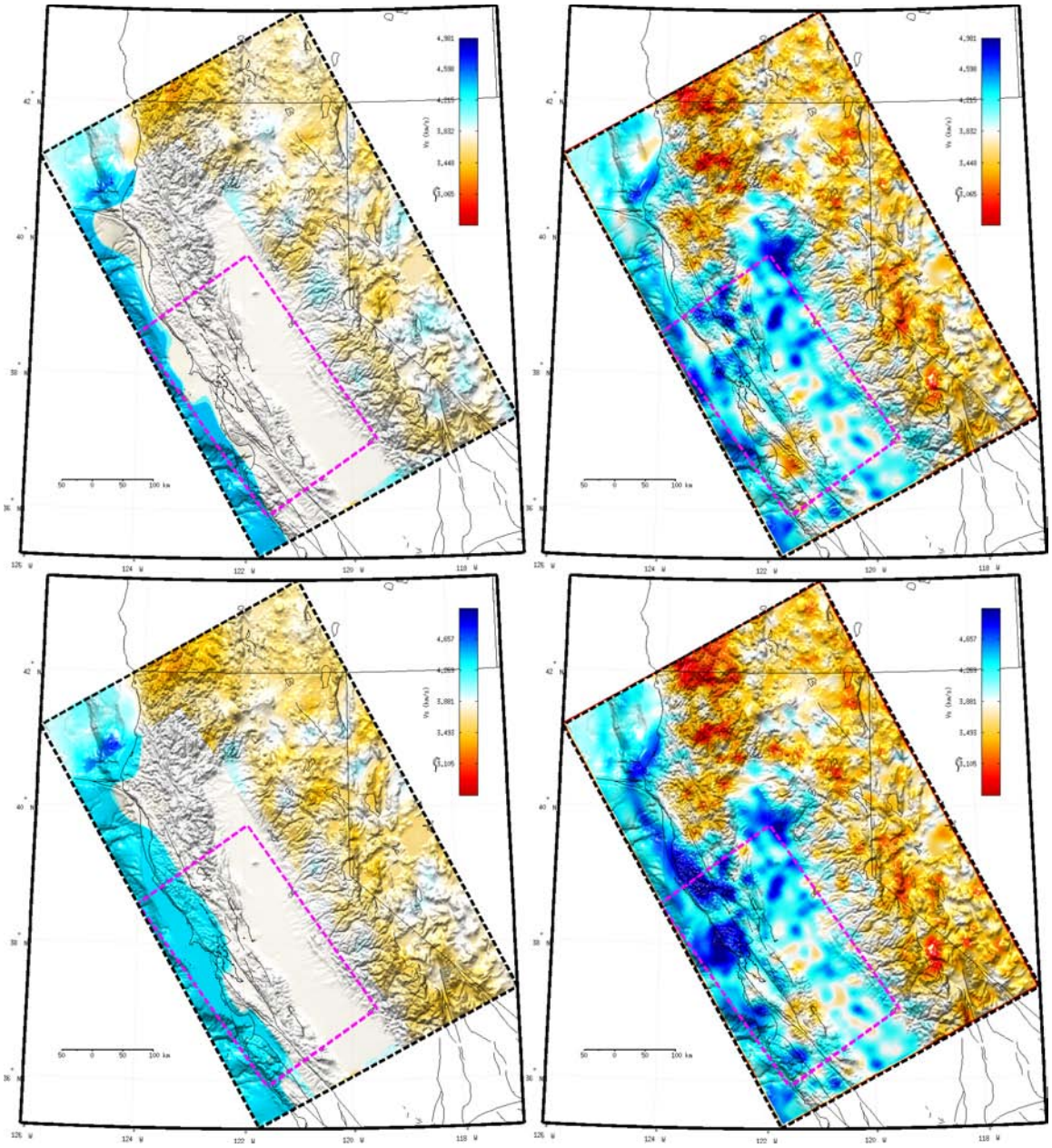

Figure 6. (continued) 22-km (upper) and 24-km (lower) depths.

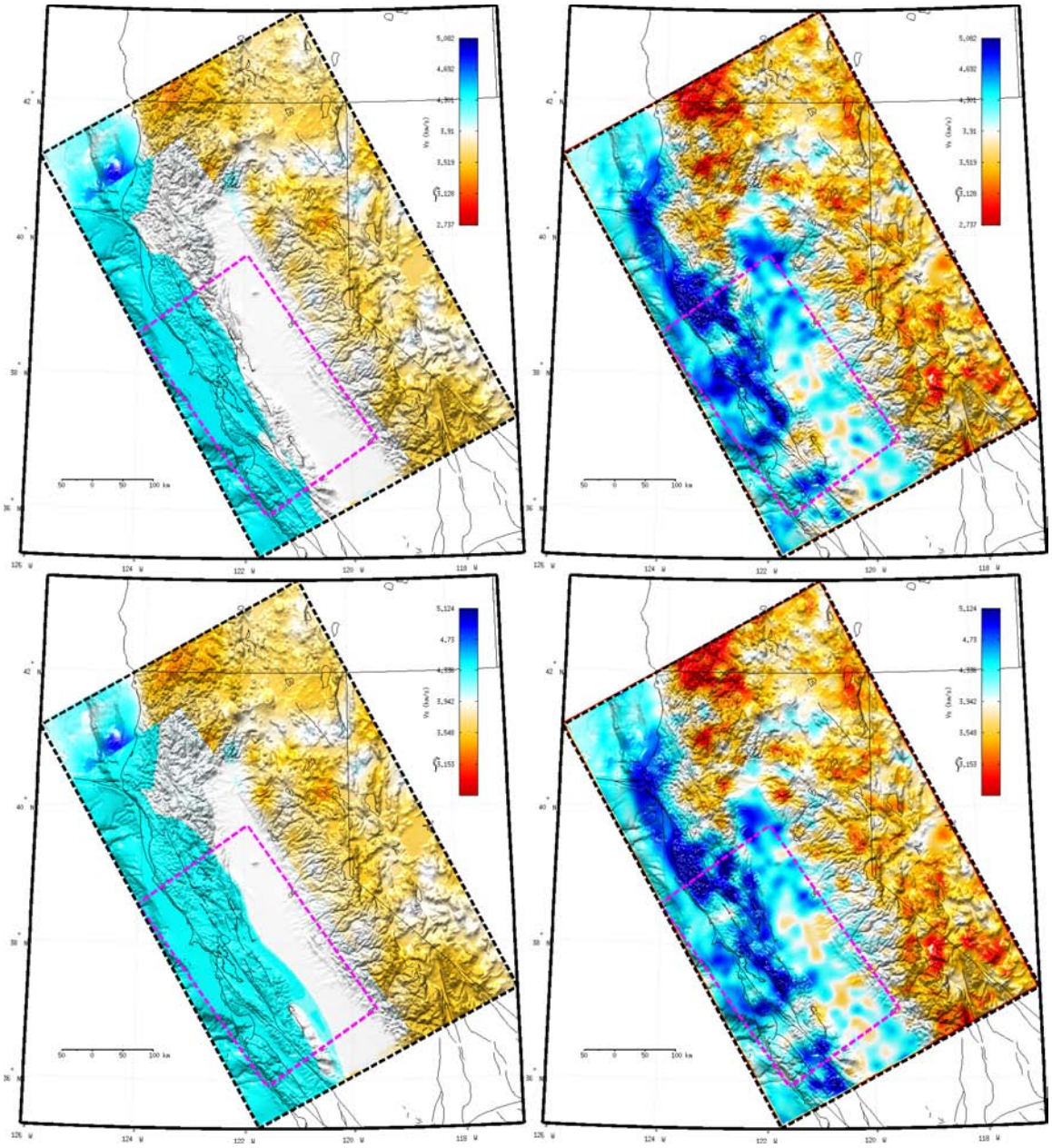

Figure 6. (continued) 26-km (upper) and 28-km (lower) depths.

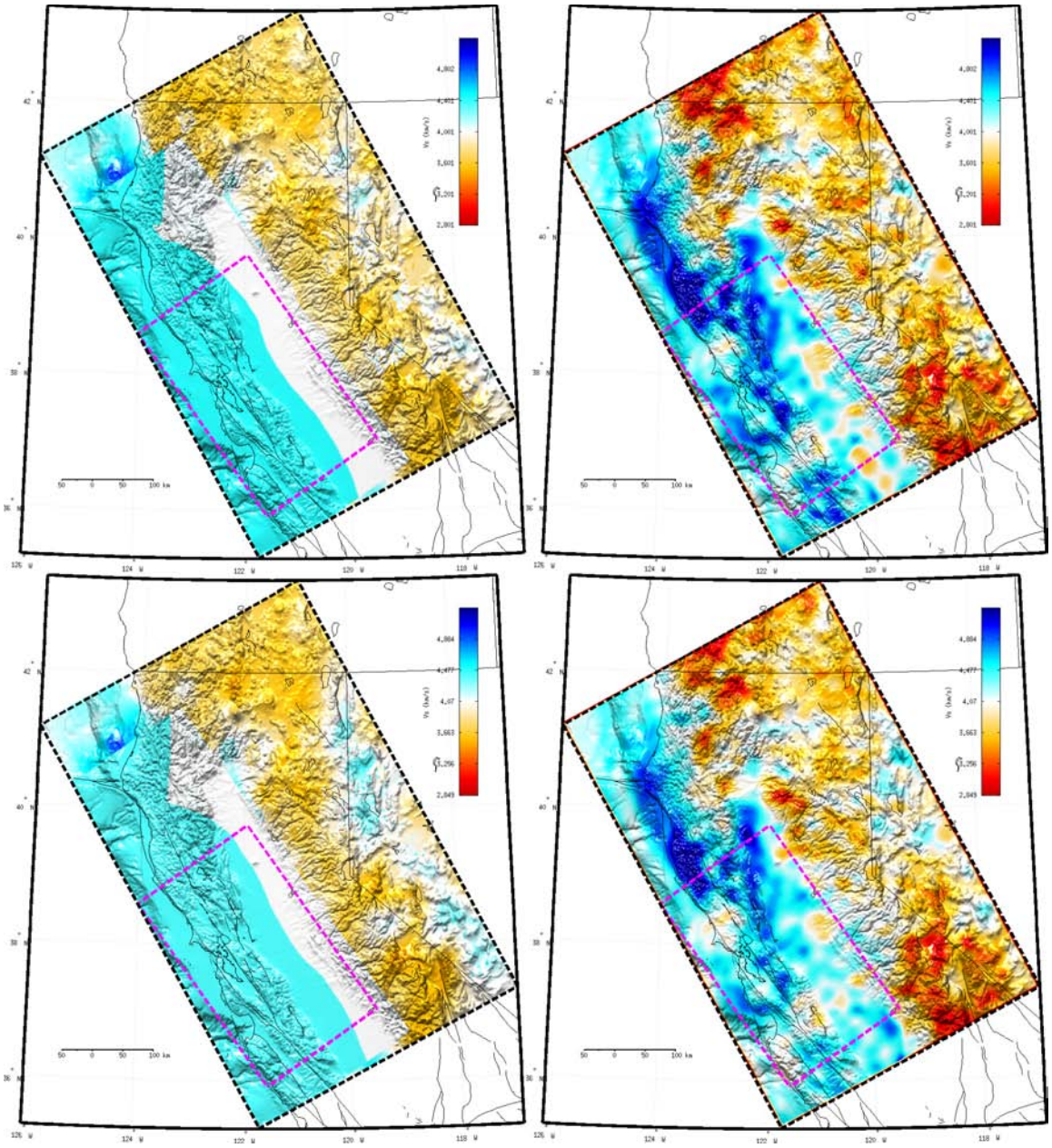

Figure 6. (continued) 30-km (upper) and 32-km (lower) depths.

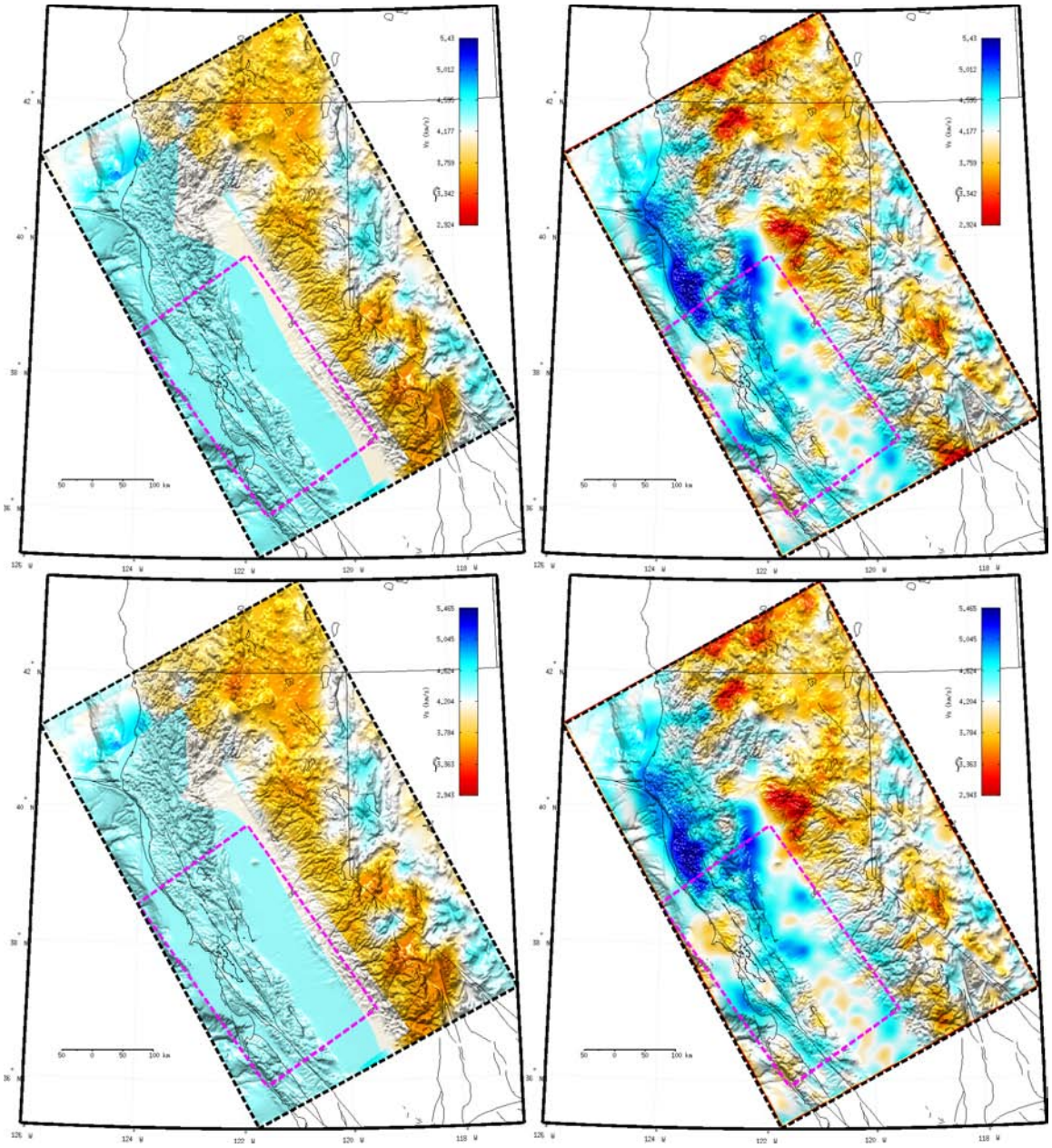

Figure 6. (continued) 34-km (upper) and 36-km (lower) depths.

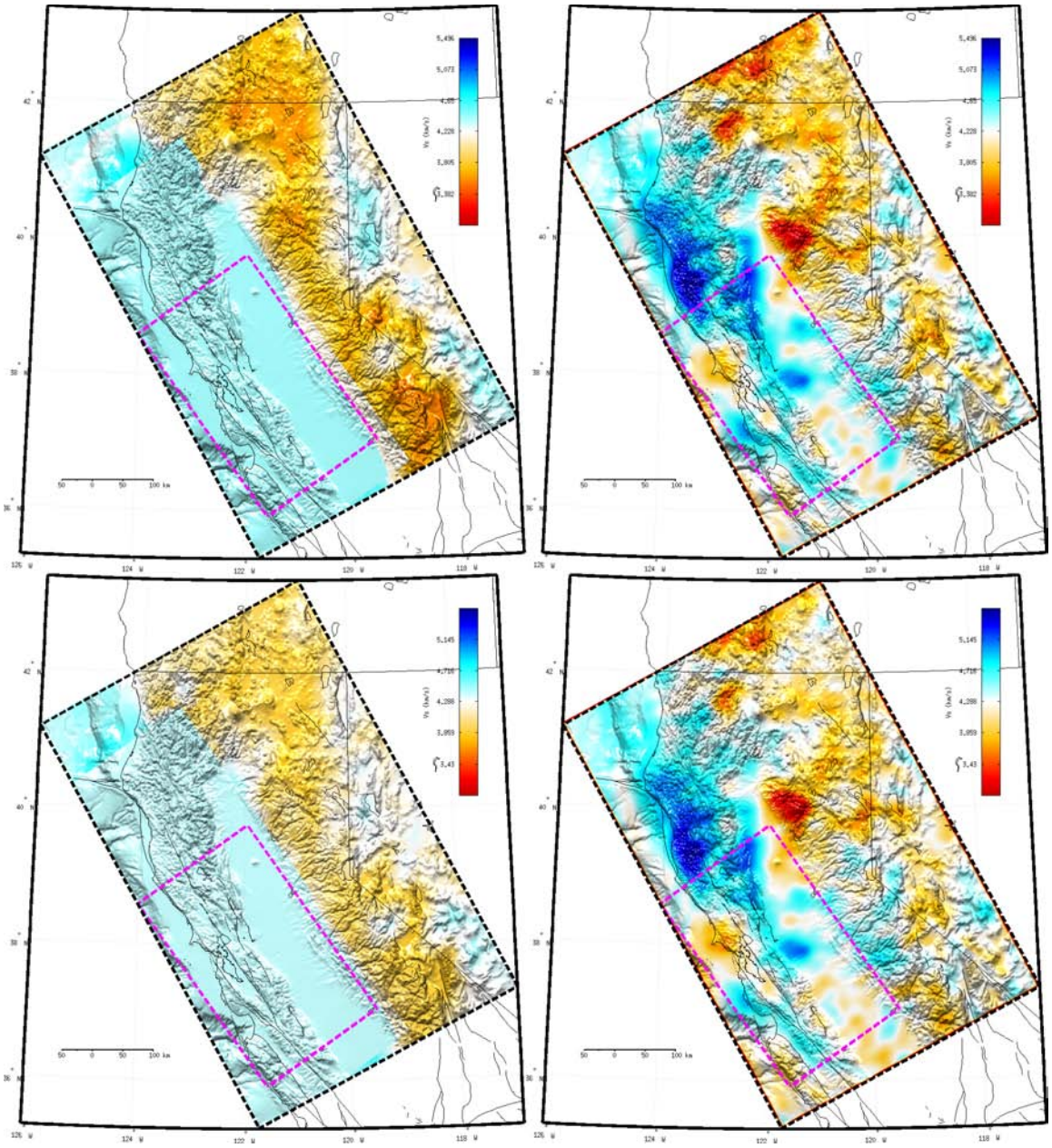

Figure 6. (continued) 38-km (upper) and 40-km (lower) depths.

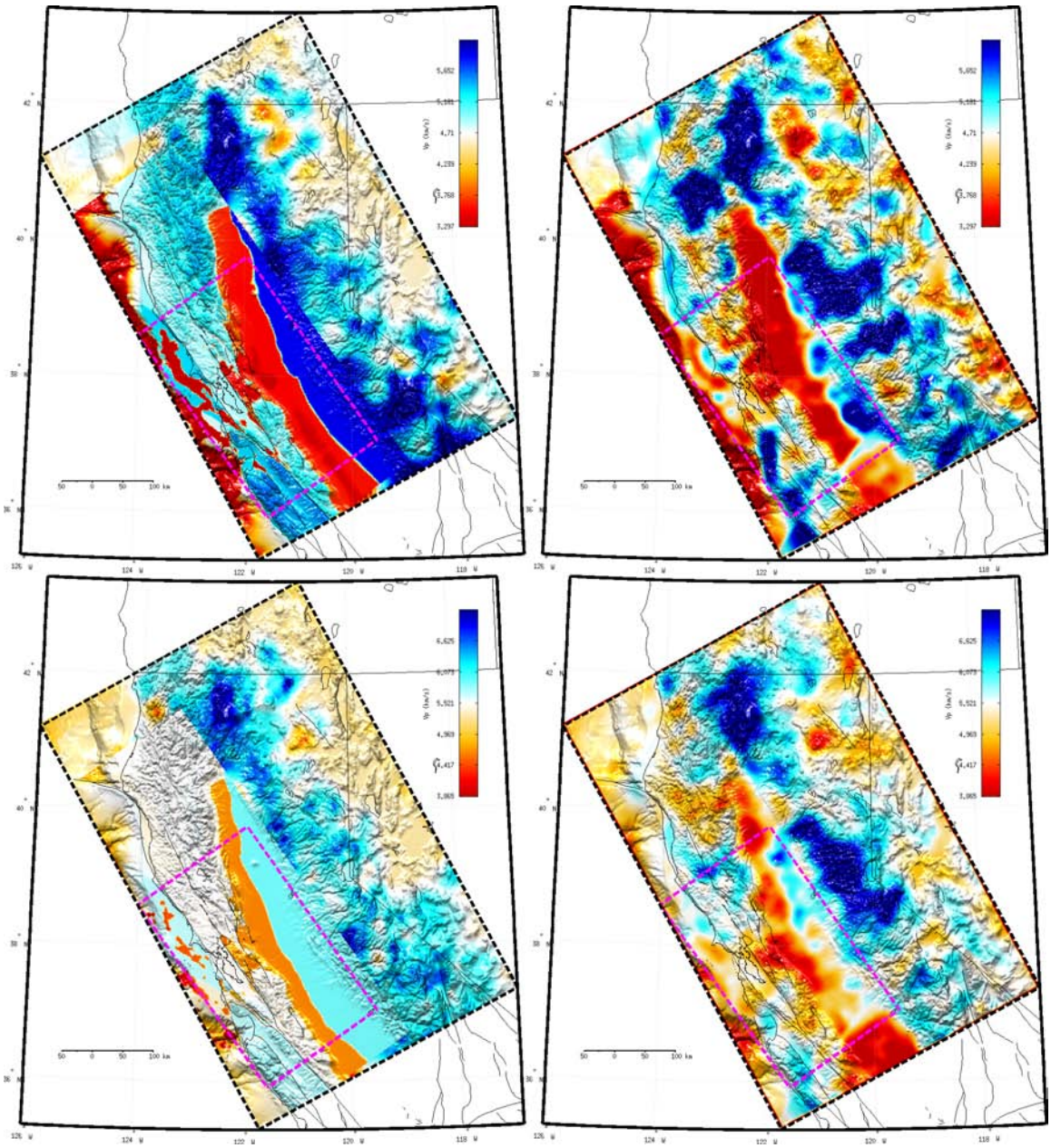

Figure 7. Map views of the 3D Vp model in our starting model NCF3D00 (left column) and the latest updated model NCF3D09 at 2-km (upper row) and 4-km (lower row) depths. Warm color: lower Vp; cold color: higher Vp; magenta dash-line box: location of the USGS Bay Area high-resolution model: black solid lines: faults, coastlines and state boundaries; background gray-scale shading: regional topography.

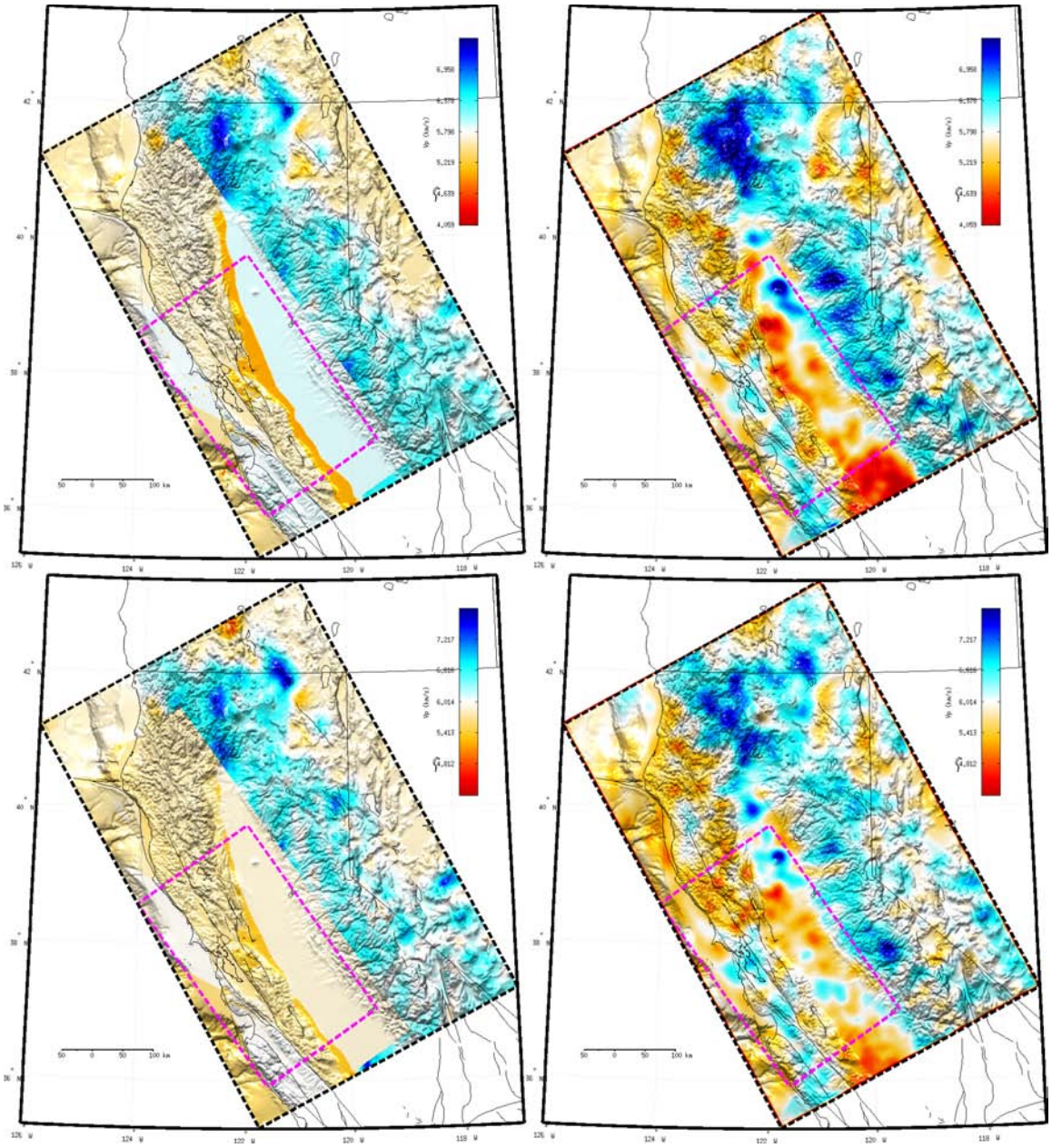

Figure 7. (continued) 6-km and 8-km depths.

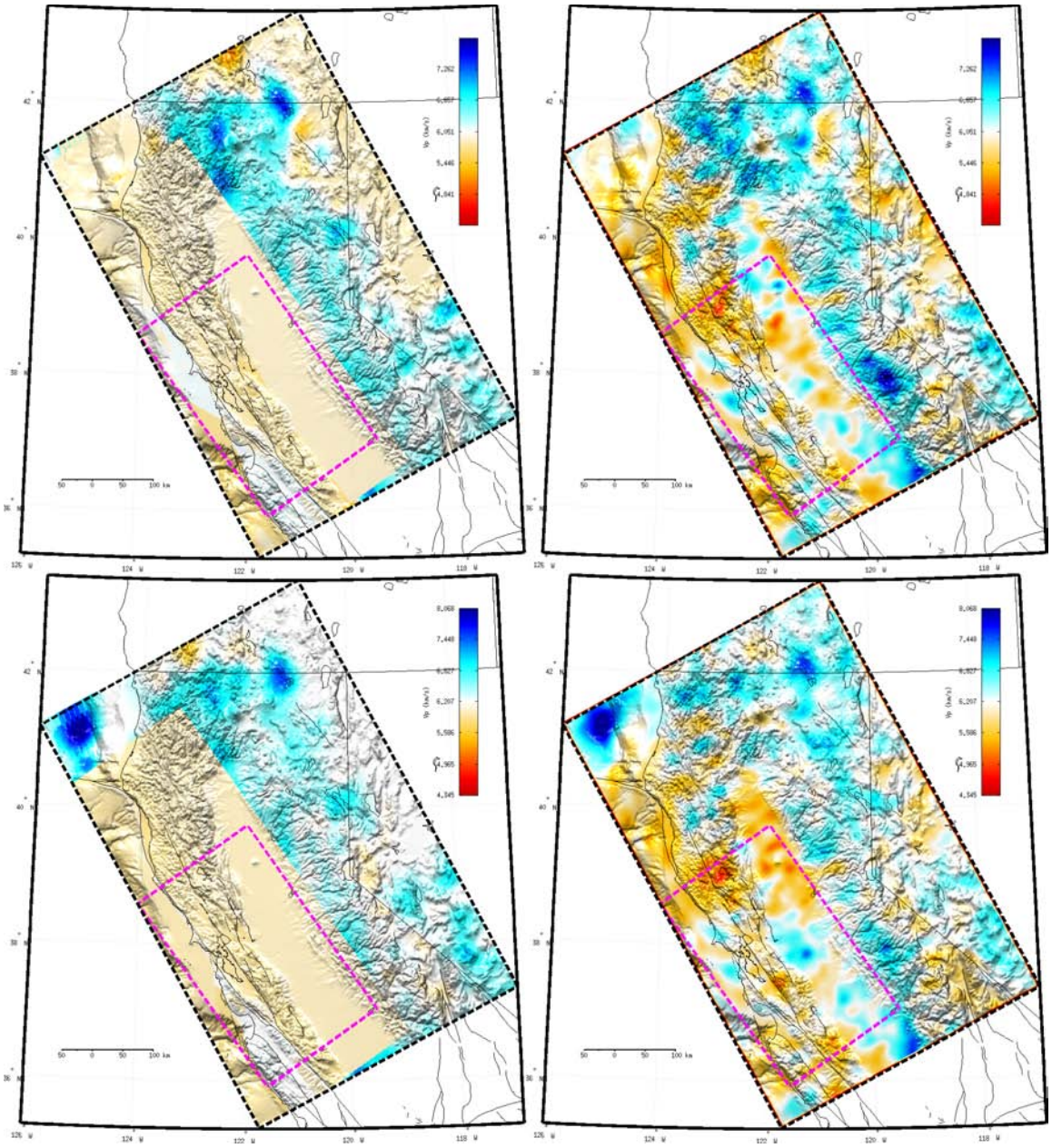

Figure 7. (continued) 10-km and 12-km depths.

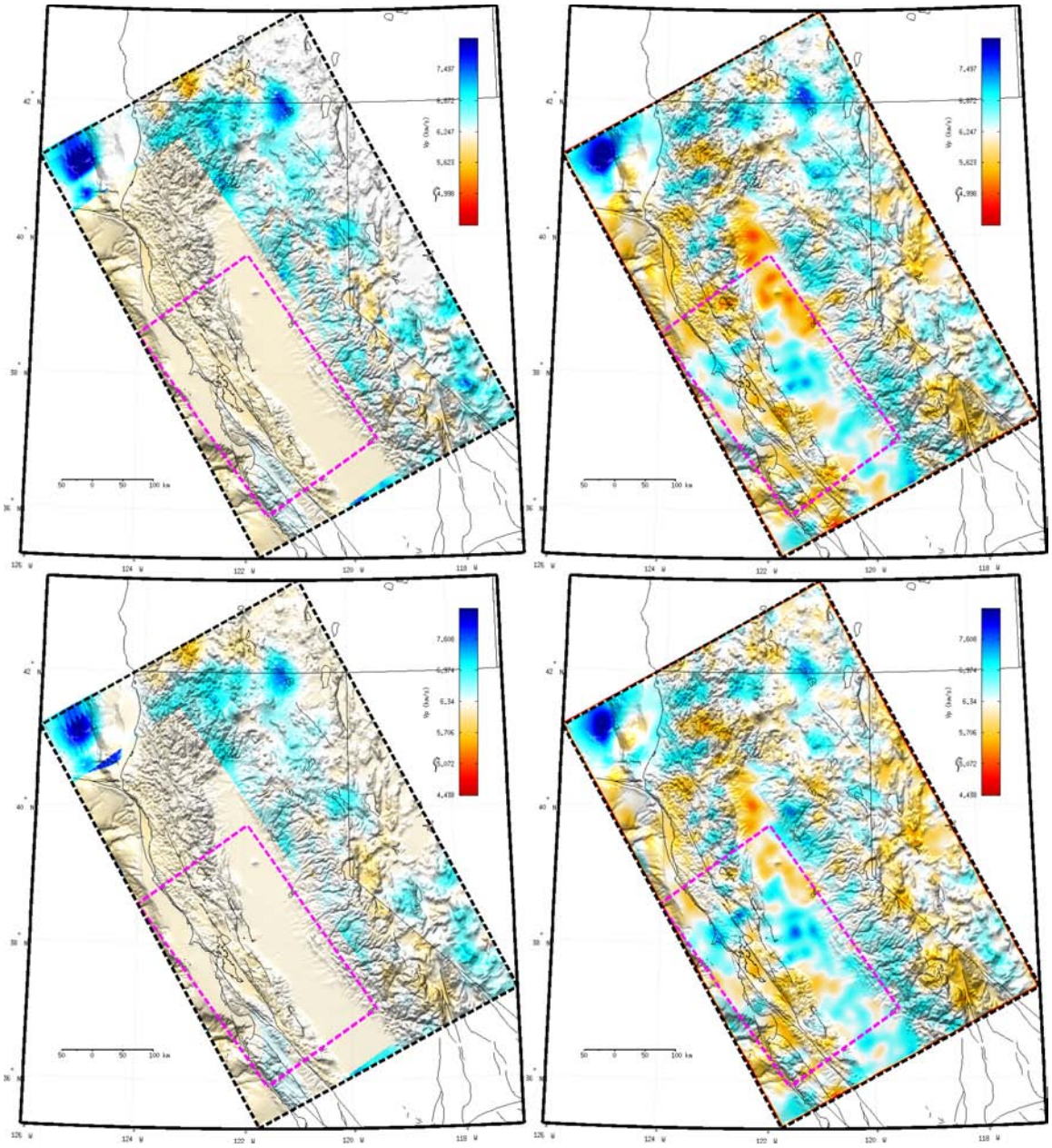

Figure 7. (continued) 14-km and 16-km depths.

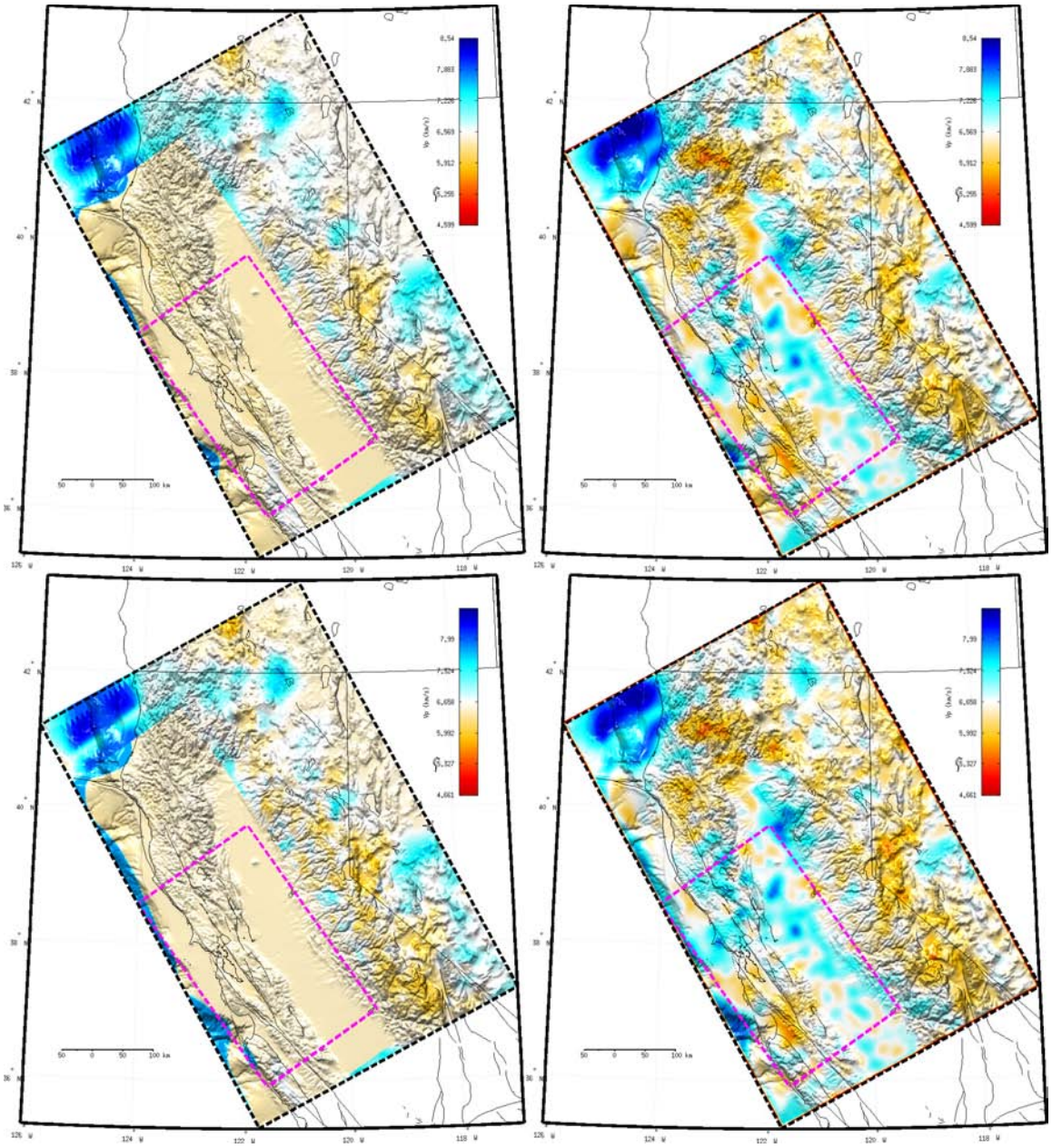

Figure 7. (continued) 18-km and 20-km depths.

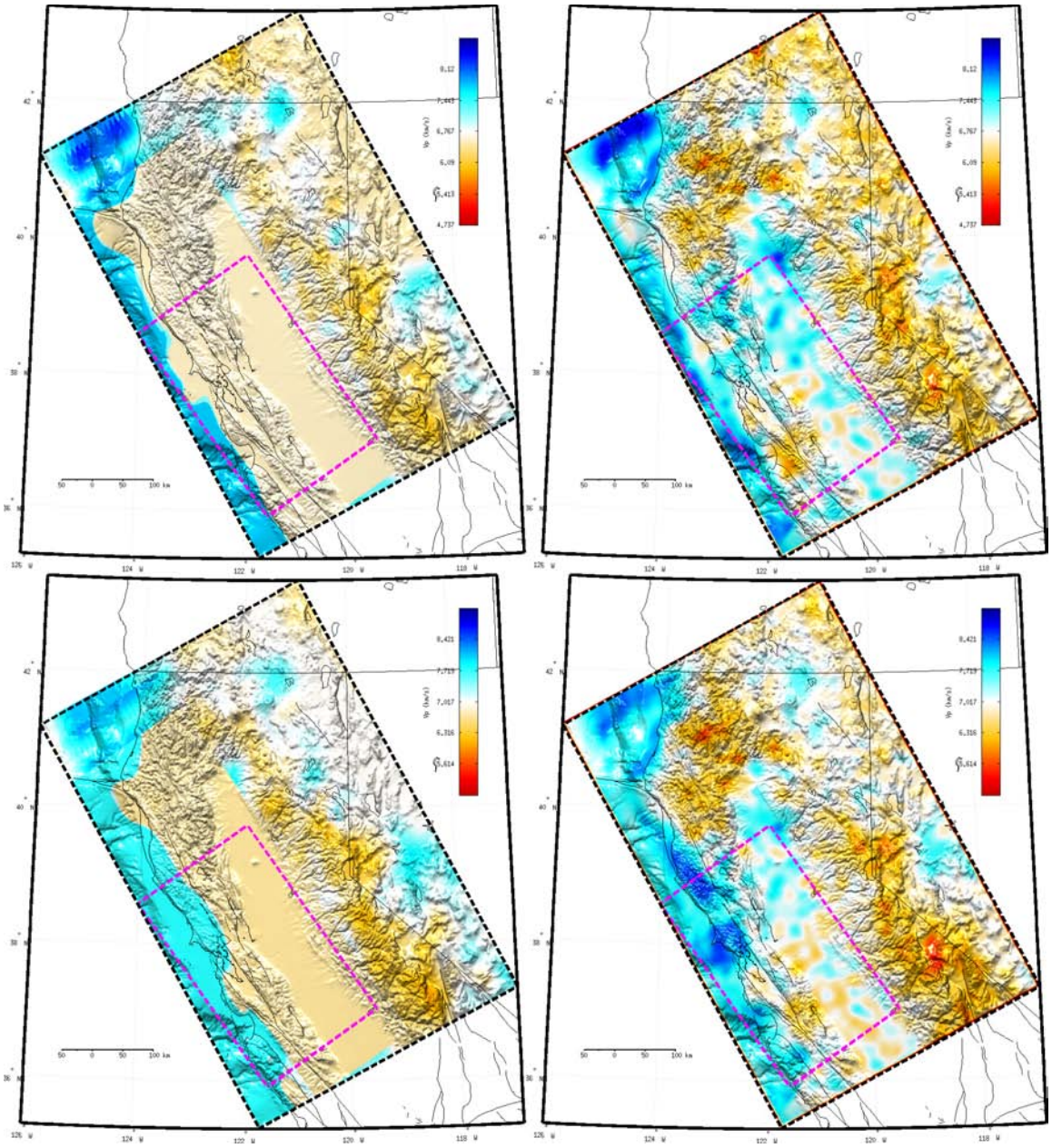

Figure 7. (continued) 22-km and 24-km depths.

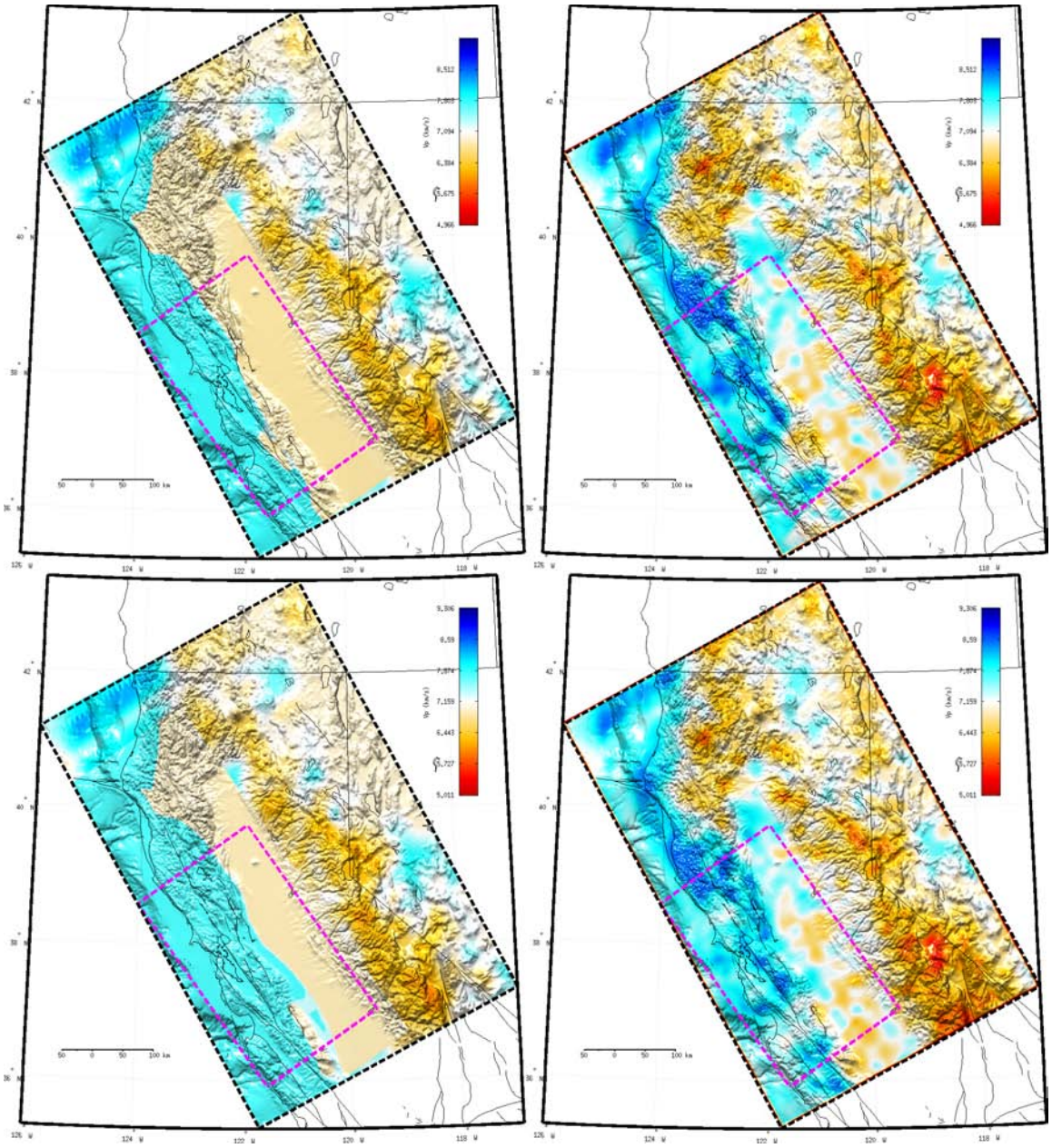

Figure 7. (continued) 26-km and 28-km depths.

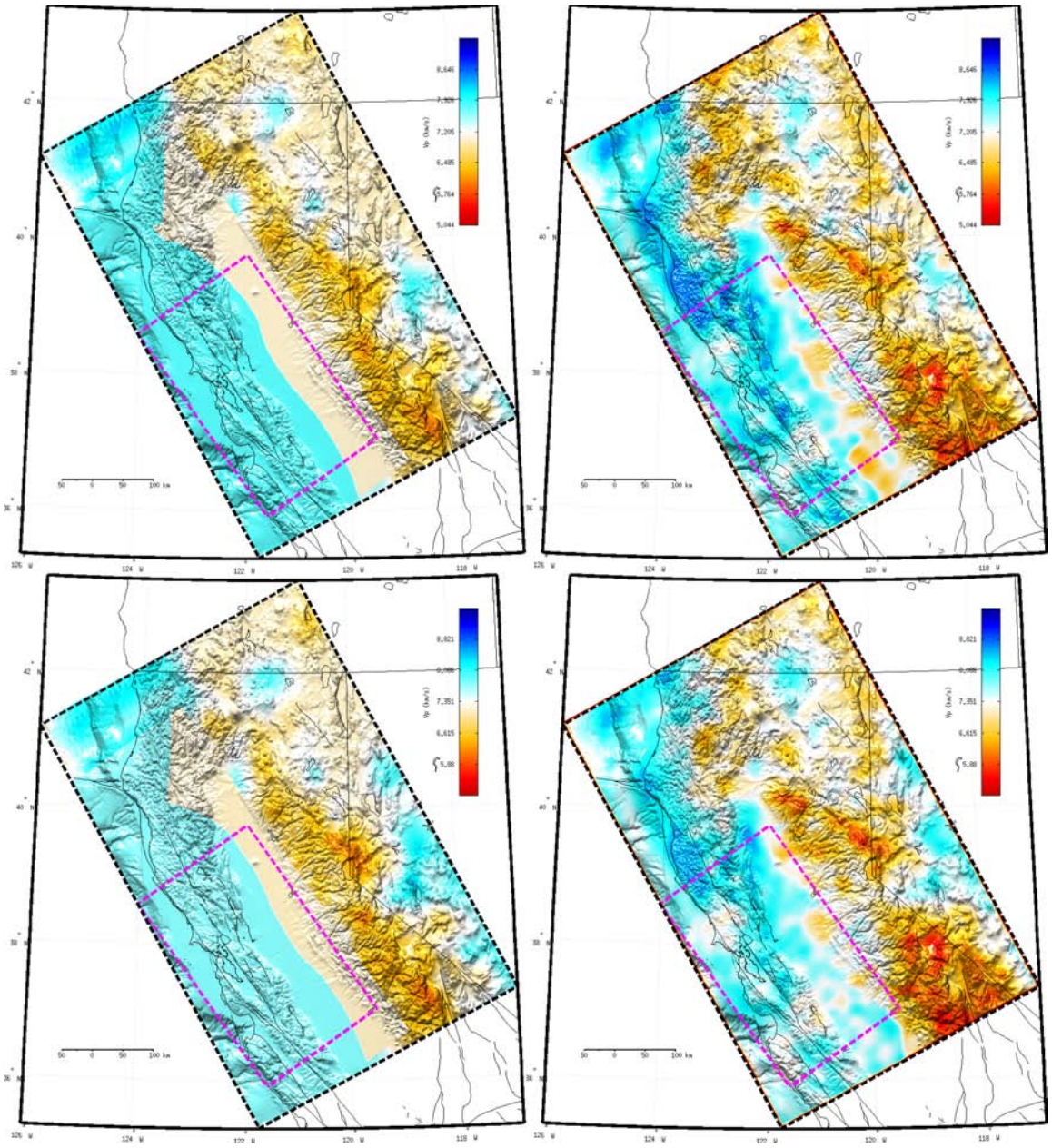

Figure 7. (continued) 30-km and 32-km depths.

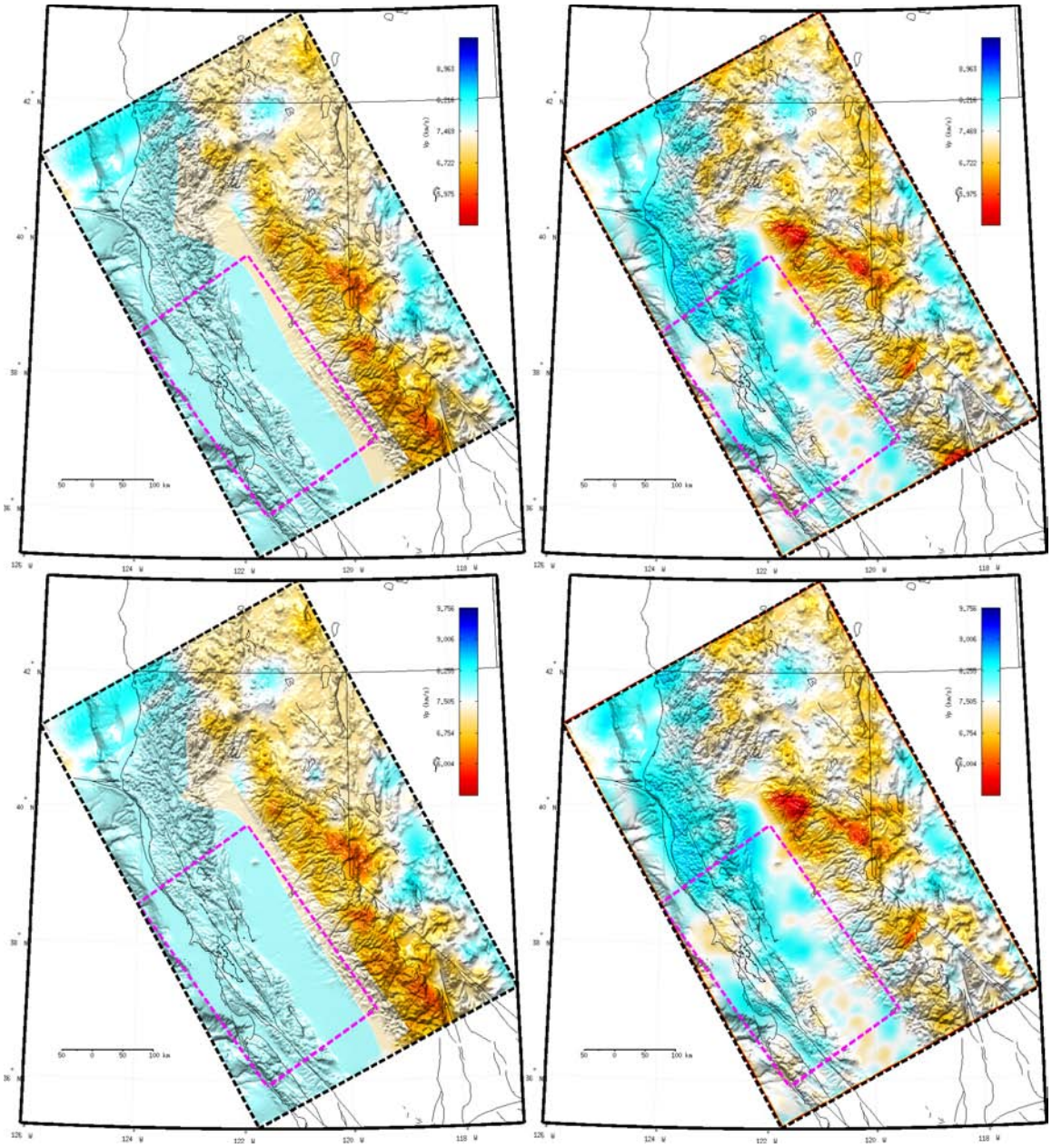

Figure 7. (continued) 34-km and 36-km depths.

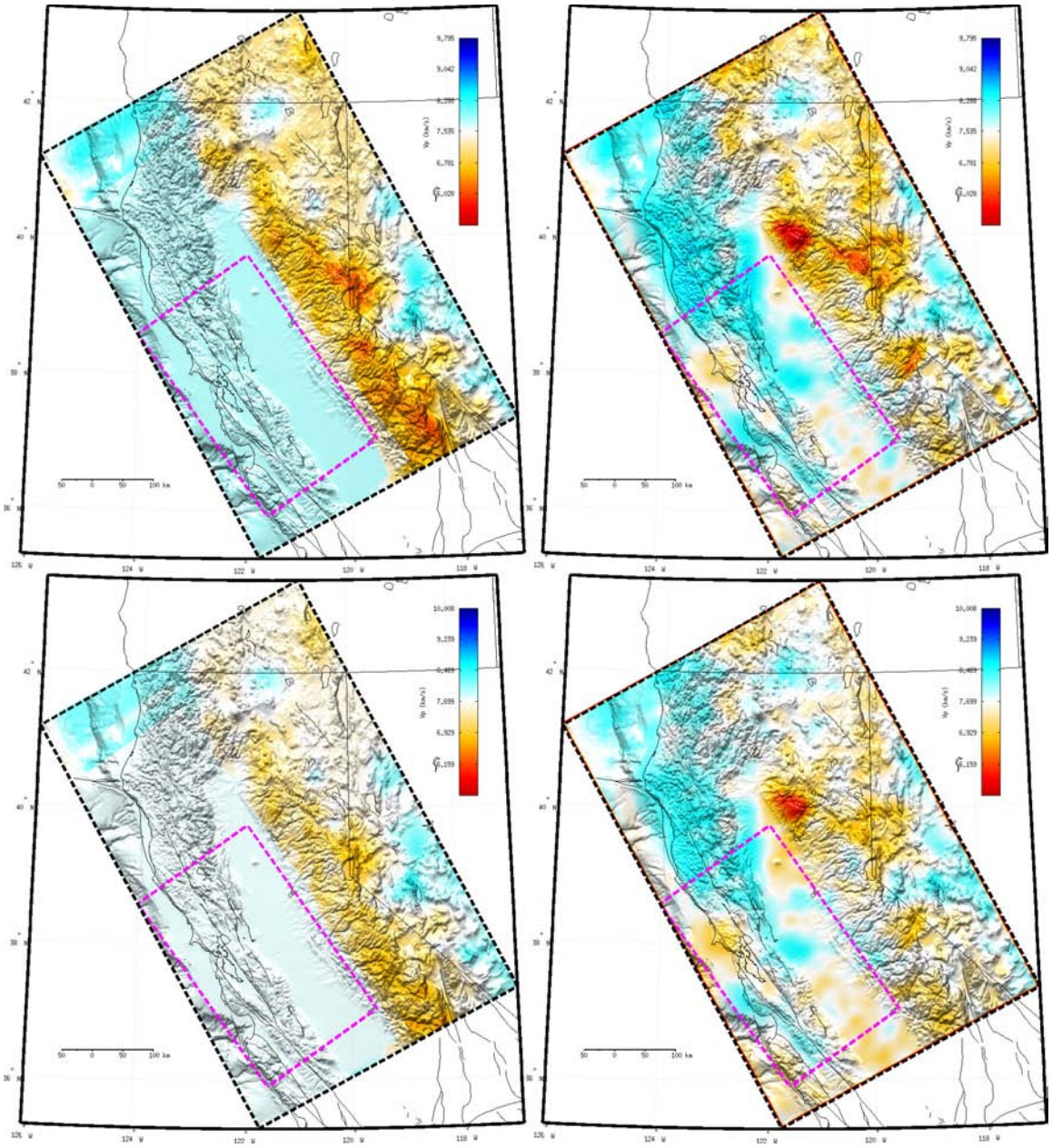

Figure 7. (continued) 38-km and 40-km depths.

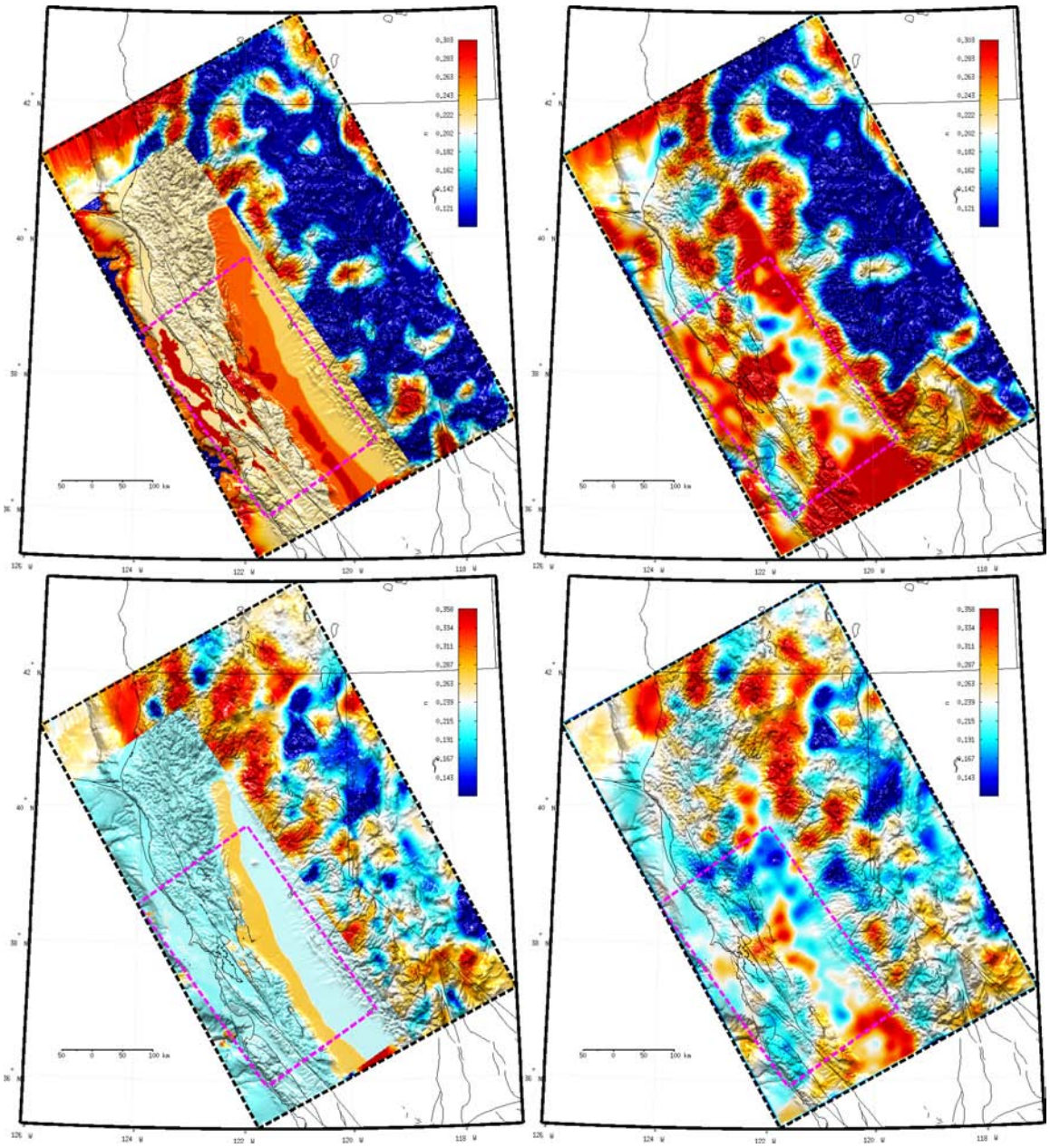

Figure 8. Map views of the 3D Poisson's ratio model in our starting model NCF3D00 (left column) and the latest updated model NCF3D09 at 2-km (upper row) and 4-km (lower row) depths. Warm color: higher Poisson's ratio; cold color: lower Poisson's ratio; magenta dash-line box: location of the USGS Bay Area high-resolution model: black solid lines: faults, coastlines and state boundaries; background gray-scale shading: regional topography.

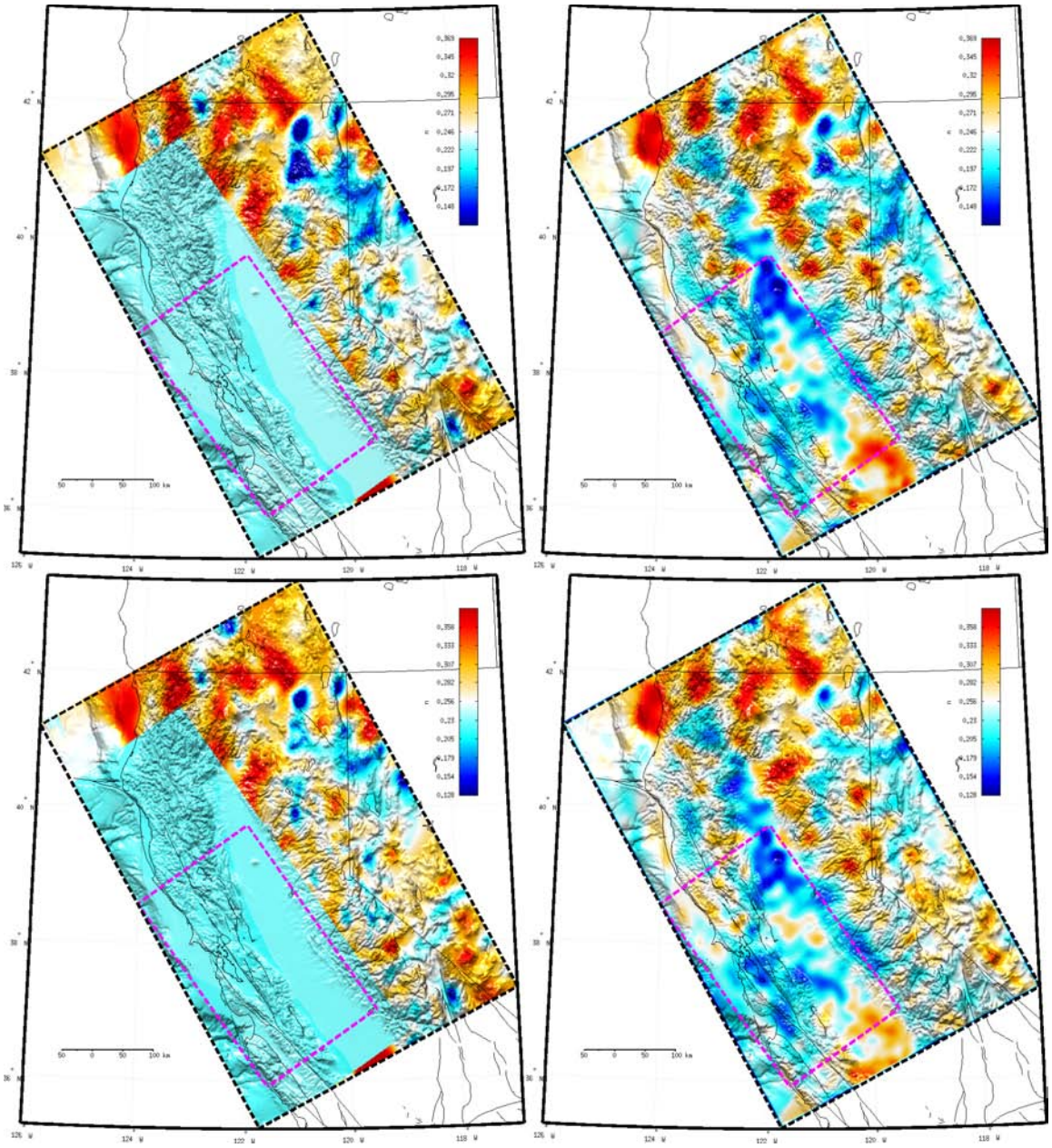

Figure 8. (continued) 6-km and 8-km depths.

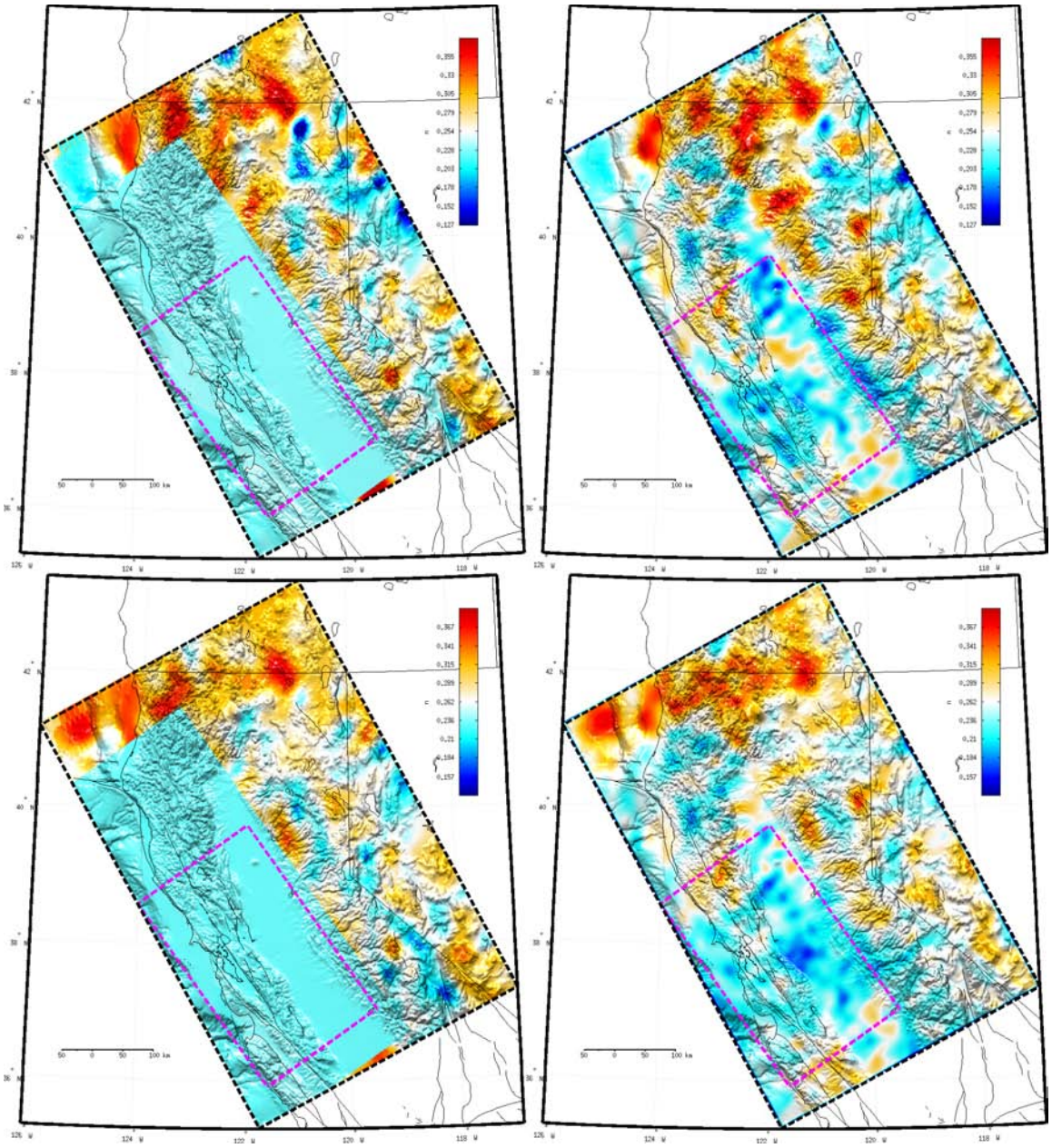

Figure 8. (continued) 10-km and 12-km depths.

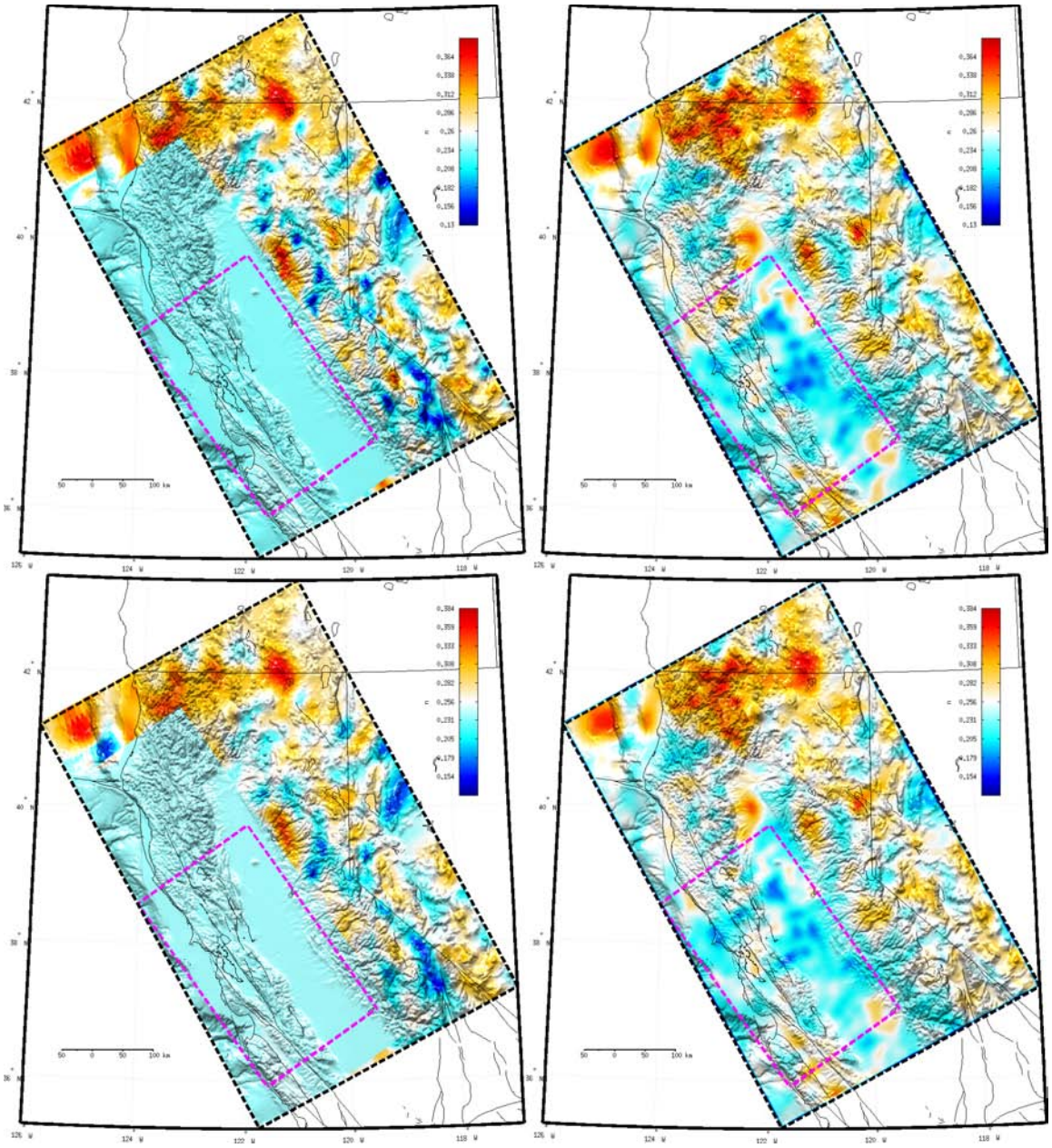

Figure 8. (continued) 14-km and 16-km depths.

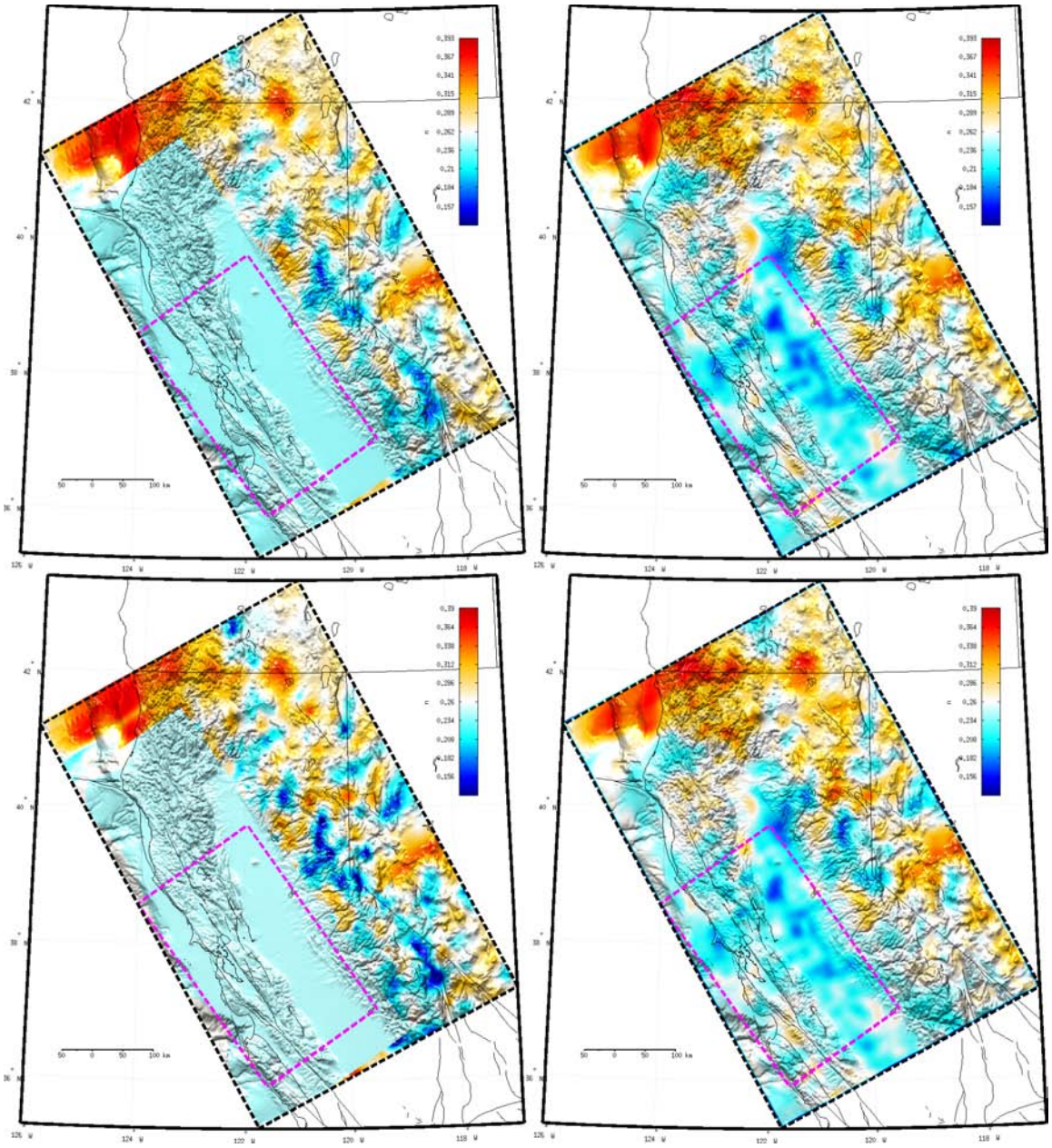

Figure 8. (continued) 18-km and 20-km depths.

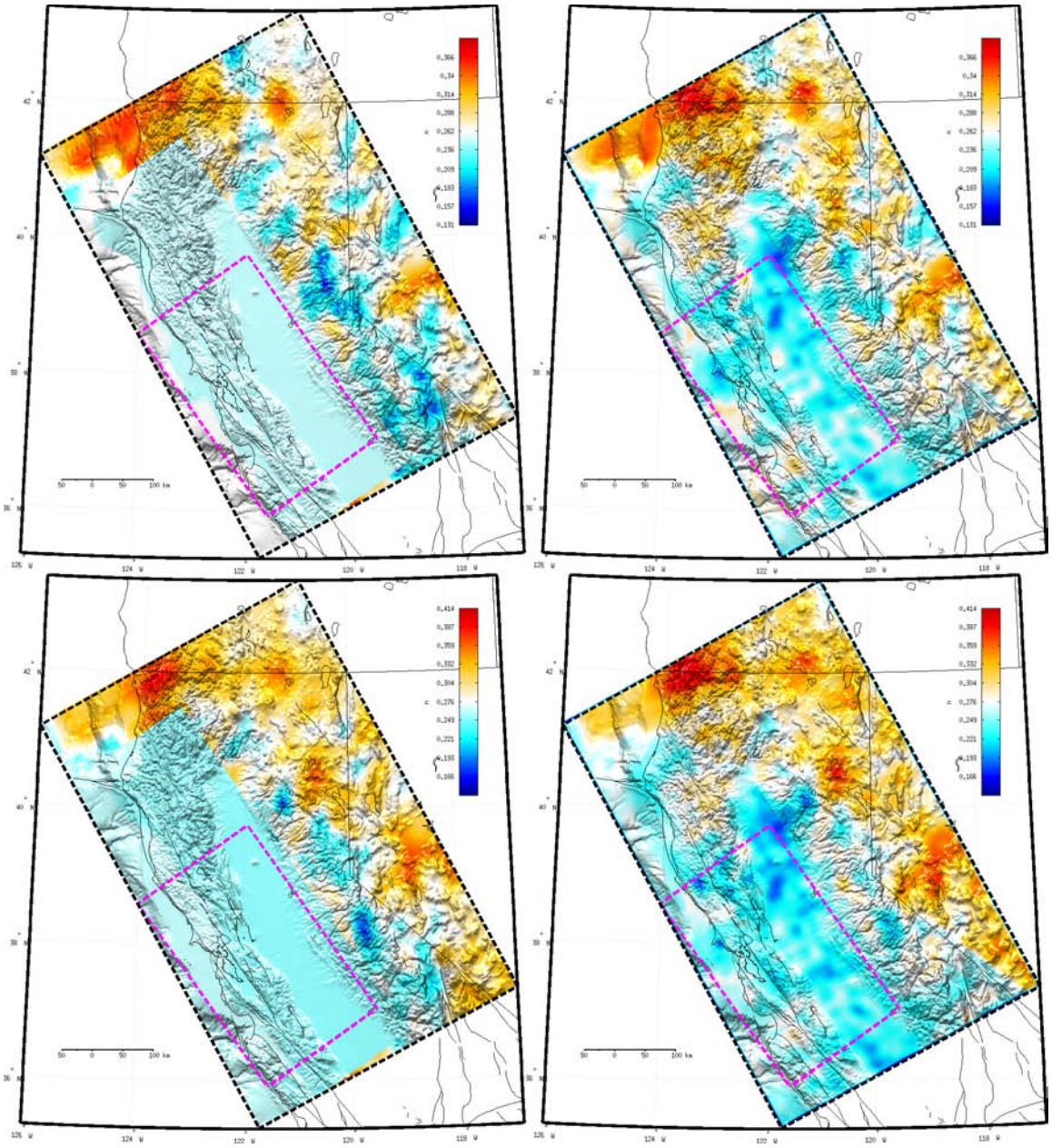

Figure 8. (continued) 22-km and 24-km depths.

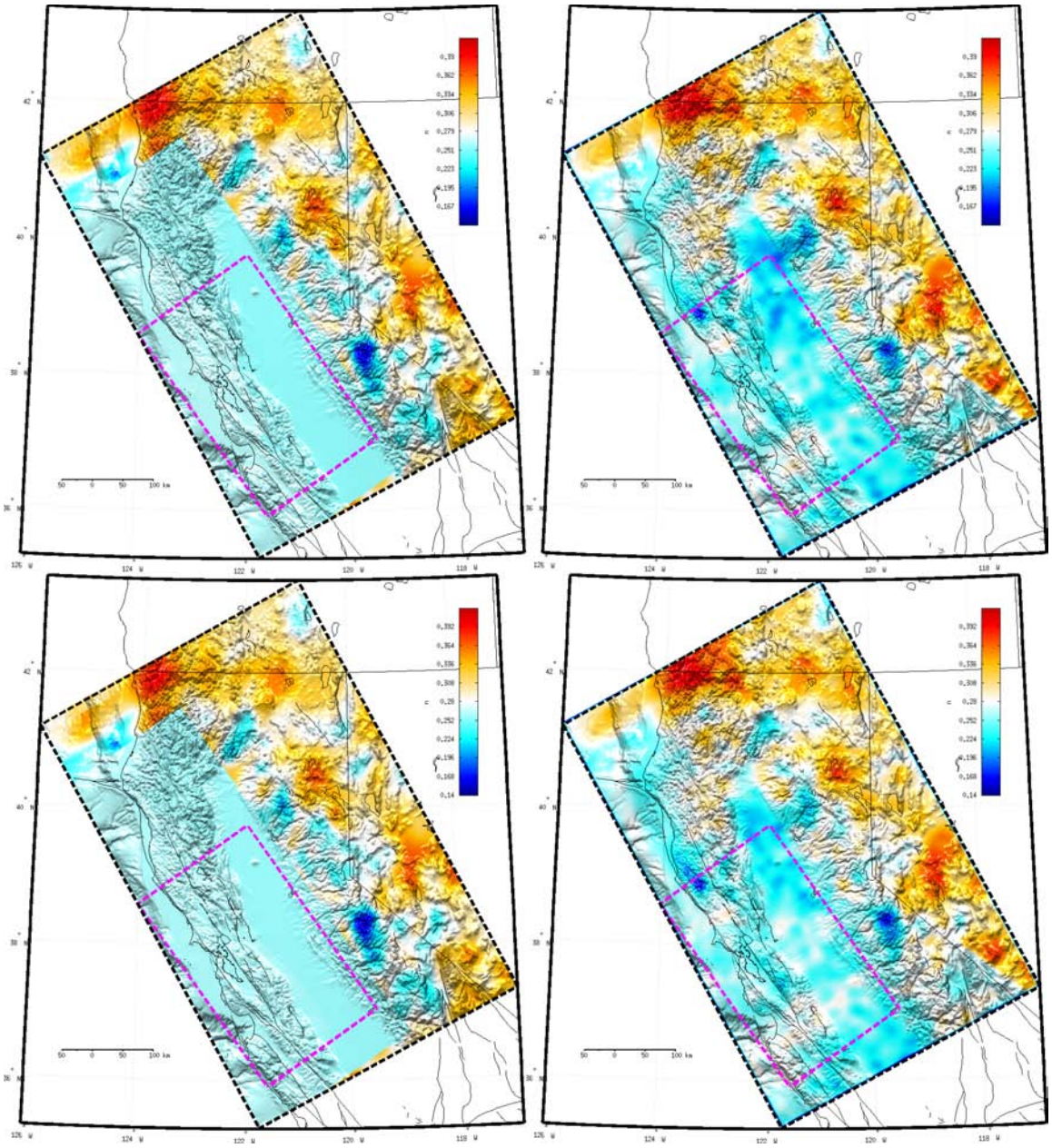

Figure 8. (continued) 26-km and 28-km depths.

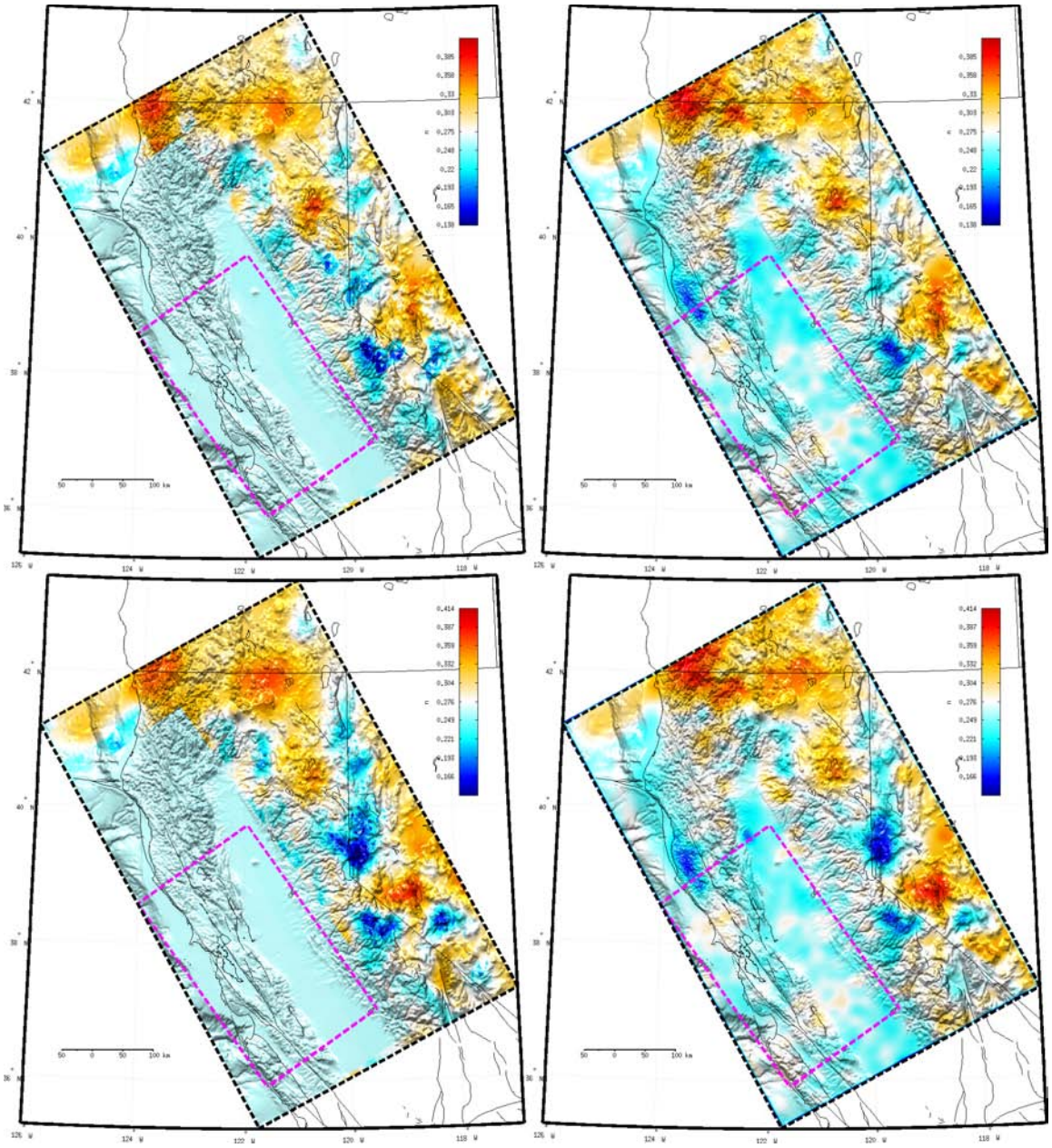

Figure 8. (continued) 30-km and 32-km depths.

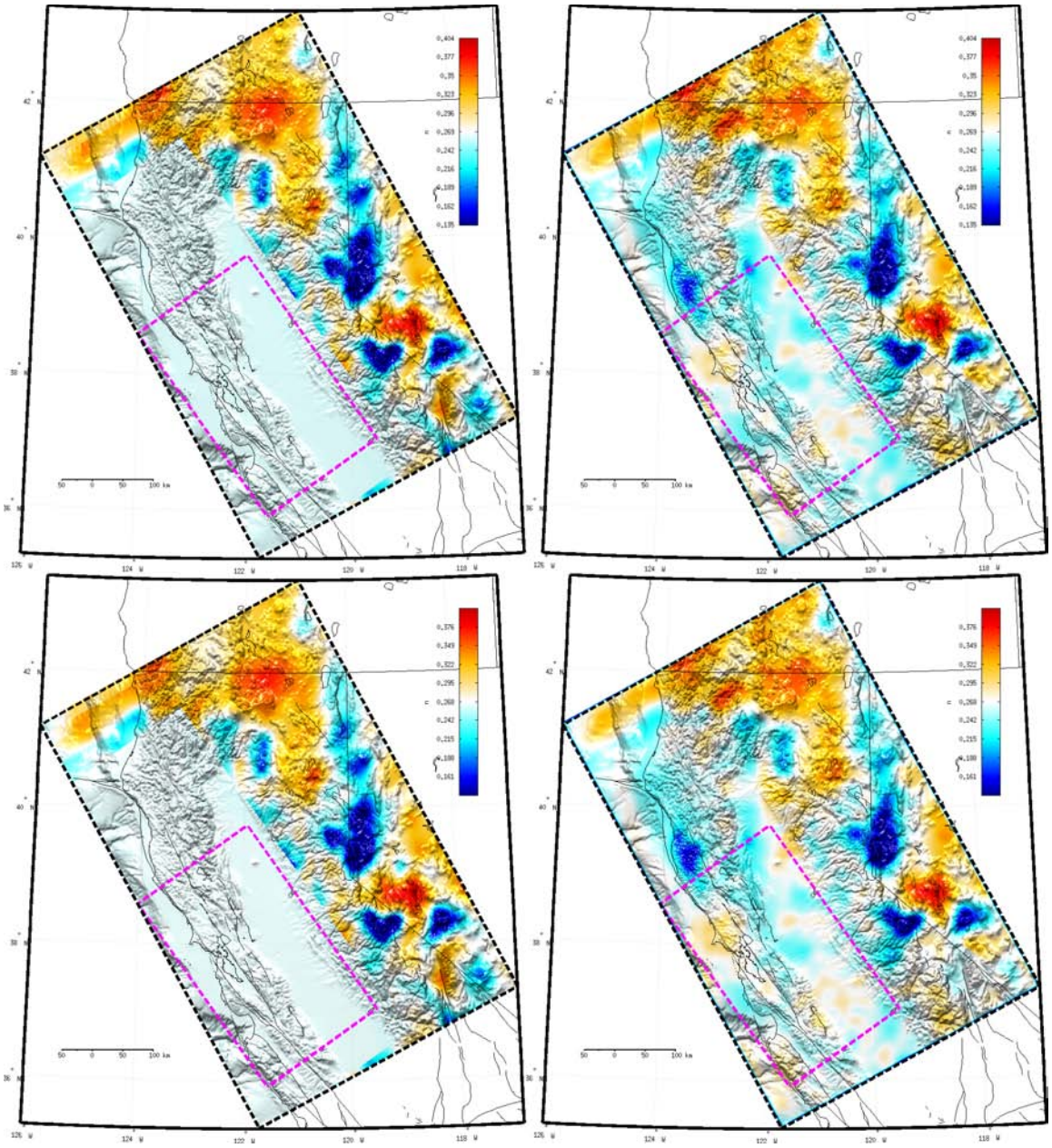

Figure 8. (continued) 34-km and 36-km depths.

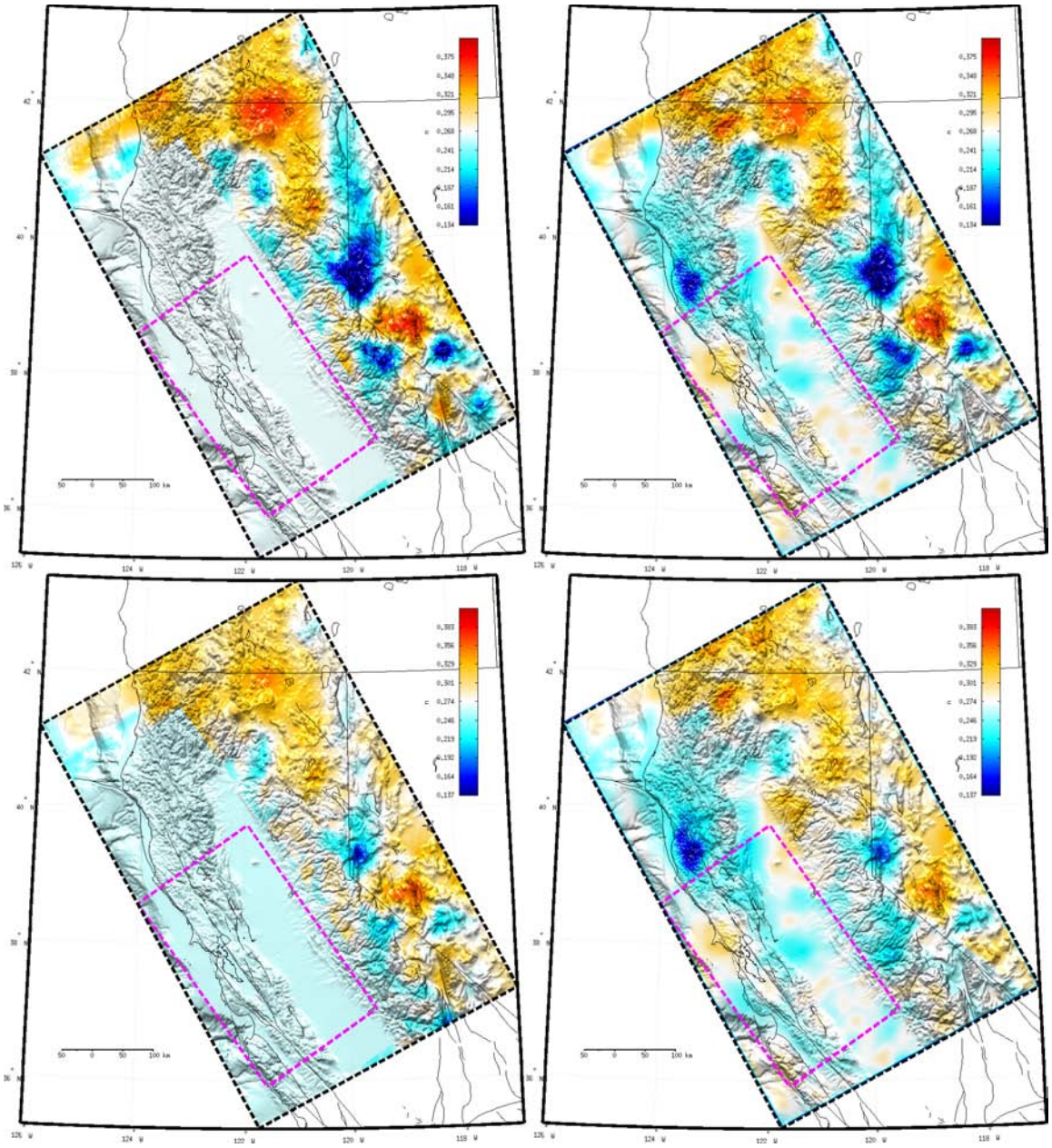

Figure 8. (continued) 38-km and 40-km depths.

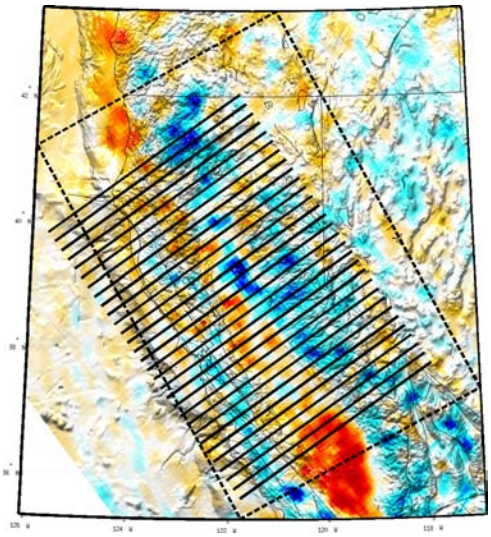

Figure 9. Locations of the southwest-northeast cross-sections. From north to south, the cross-sections are labeled as (a), (b), (c),…, (z), (aa), (bb), (cc), (dd). The locations of the cross-sections are identical to the corresponding cross-sections shown in Thurber et al (2009). The starting locations of some of the cross-sections lie outside of our NC F3DT box (black dash line) and velocity values from our California statewide F3DT model are used for those segments. Background color shows Vs in the statewide model at 6-km depth.

Both the map-views and the cross-section views show that NCF3D09 has much more details (small-scale features) than our starting model NCF3D00. For example, at shallow depths, low-velocity anomalies are mainly associated with sedimentary basins, such as the Great Valley, in both NCF3D00 and NCF3D09. However, NCF3D09 also shows significant velocity variations inside the Great Valley. Sediments around the Sacramento River Delta area appear to be thicker in NCF3D09. Velocities west of the Hayward Fault appear to be significantly faster in NCF3D09 than in NCF3D00. In regions not covered by the USGS Bay area model but by the statewide RTT model, NCF3D09 appears to be enhancing the velocity gradients already existing in the statewide RTT model, which is a phenomenon we also observed in previous F3DT inversions using RTT models as starting models (e.g., Chen et al., 2007a; Lee et al., 2014a).

A thorough interpretation of NCF3D09 is still underway. Many structural features that were imaged in Thurber et al. (2009) are also visible in NCF3D09 and some of those features are imaged with more clarity. For example, the geometry of the subducting Gorda plate is well constructed in NCF3D09 (Figure 10-12). The shallow high-velocity anomaly around the Klamath Mountains region appears to be extending to a much larger depth towards southwest and connected to the subducting Gorda plate. The mid-crustal low-velocity zones beneath Mount Shasta and Lake Tahoe imaged in Thurber et al. (2009) are also visible in NCF3D09 with additional fine-scale details. The Great Value ophiolite body underneath the basin sediments is well constructed in NCF3D09 and the geometry and the spatial extent of the ophiolite body is well imaged. The mid- to lower-crustal low-velocity zone under the Long Valley caldera is well constructed with additional details in NCF3D09. At shallower depth, low-velocity anomalies in NCF3D09 have good correlation with the distribution of sediments and high-velocity anomalies are associated with Sierra Nevada, Klamath Mountains and Lake Oroville. Sharp velocity contrasts in upper crust in NCF3D09 appear to correlate with the locations of major faults in this region.

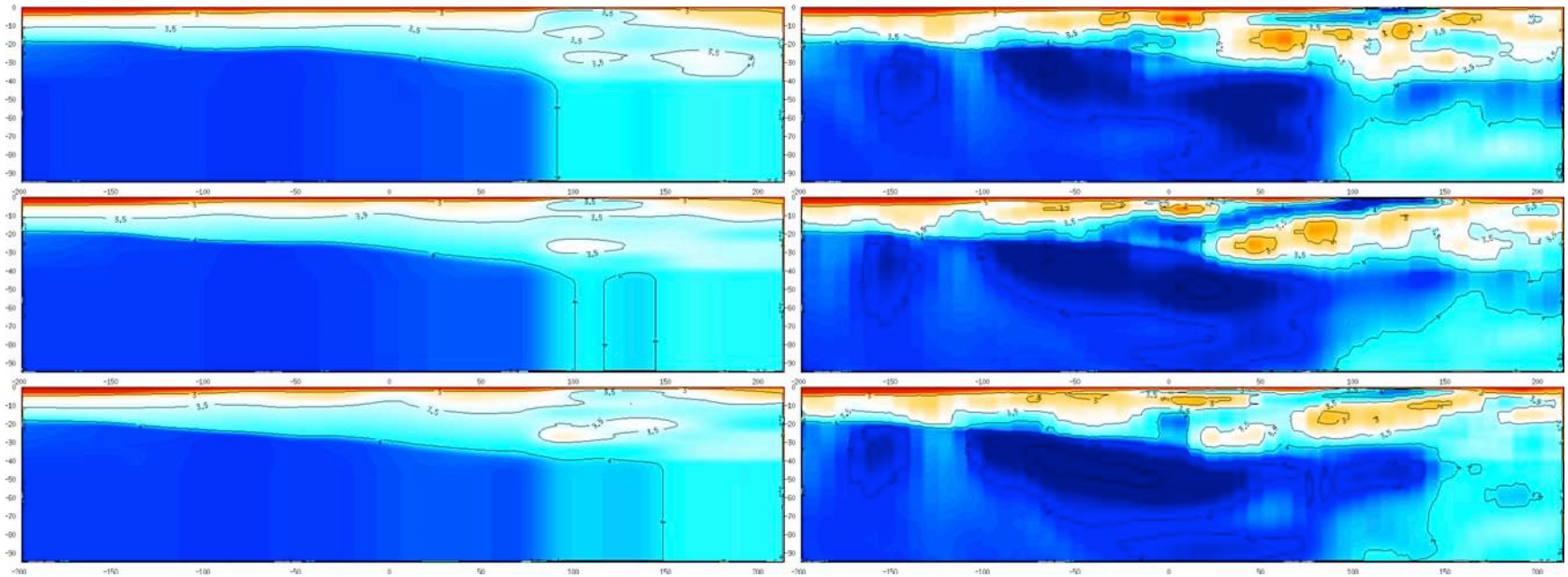

Figure 10. Cross-section views of the Vs model in NCF3D00 (left) and NCF3D09 (right) for cross-sections (a)-(c). Horizontal and vertical dimensions are in km. No vertical exaggeration in all cross-sections.

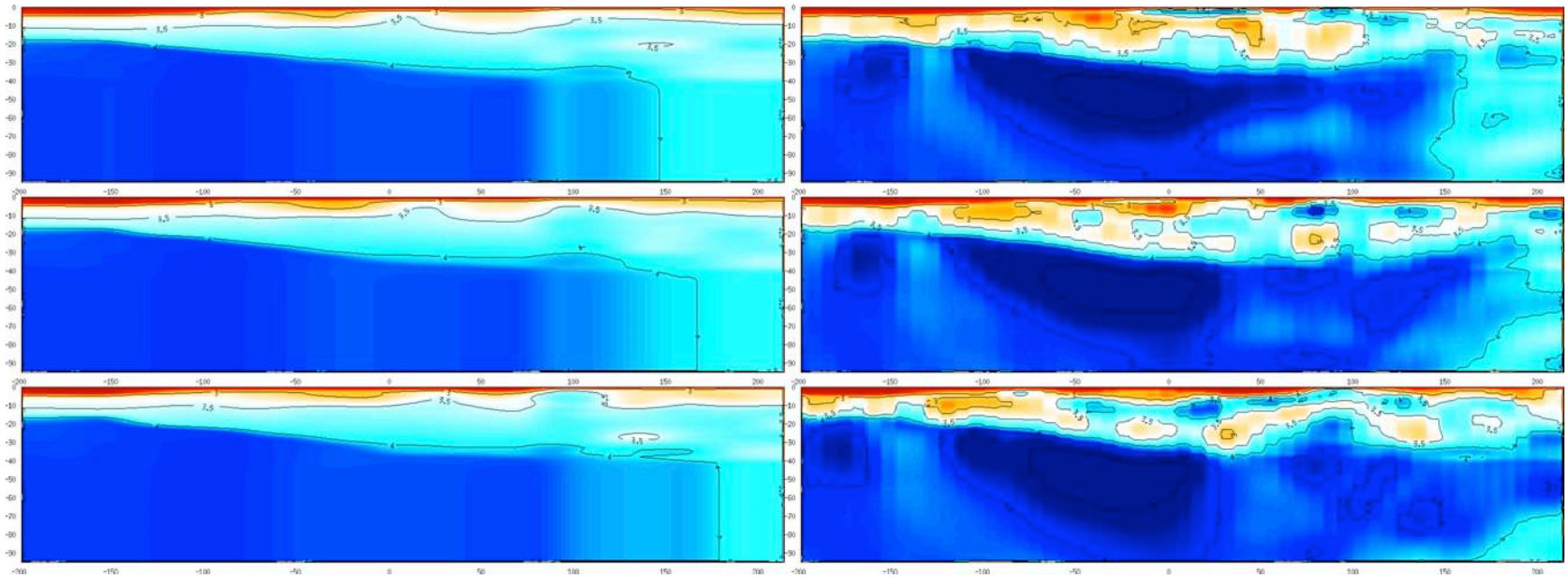

Figure 10. (continued) cross-sections (d)-(f).

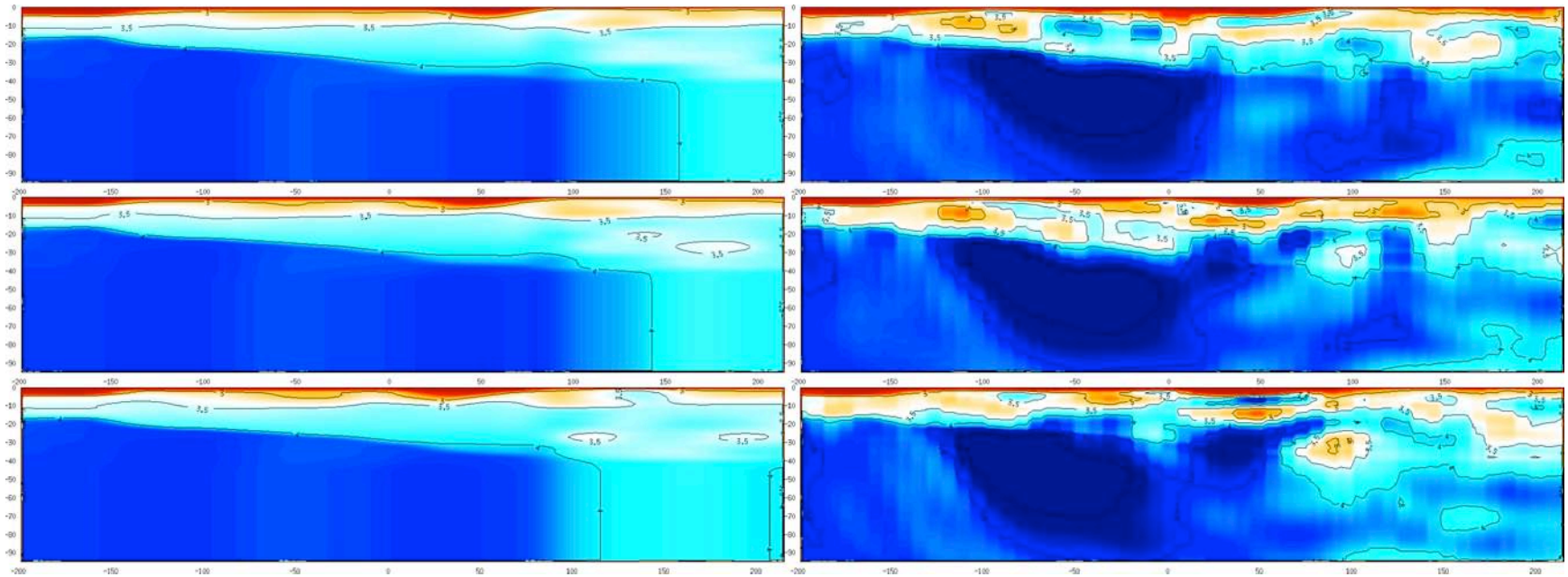

Figure 10. (continued) cross-sections (g)-(i).

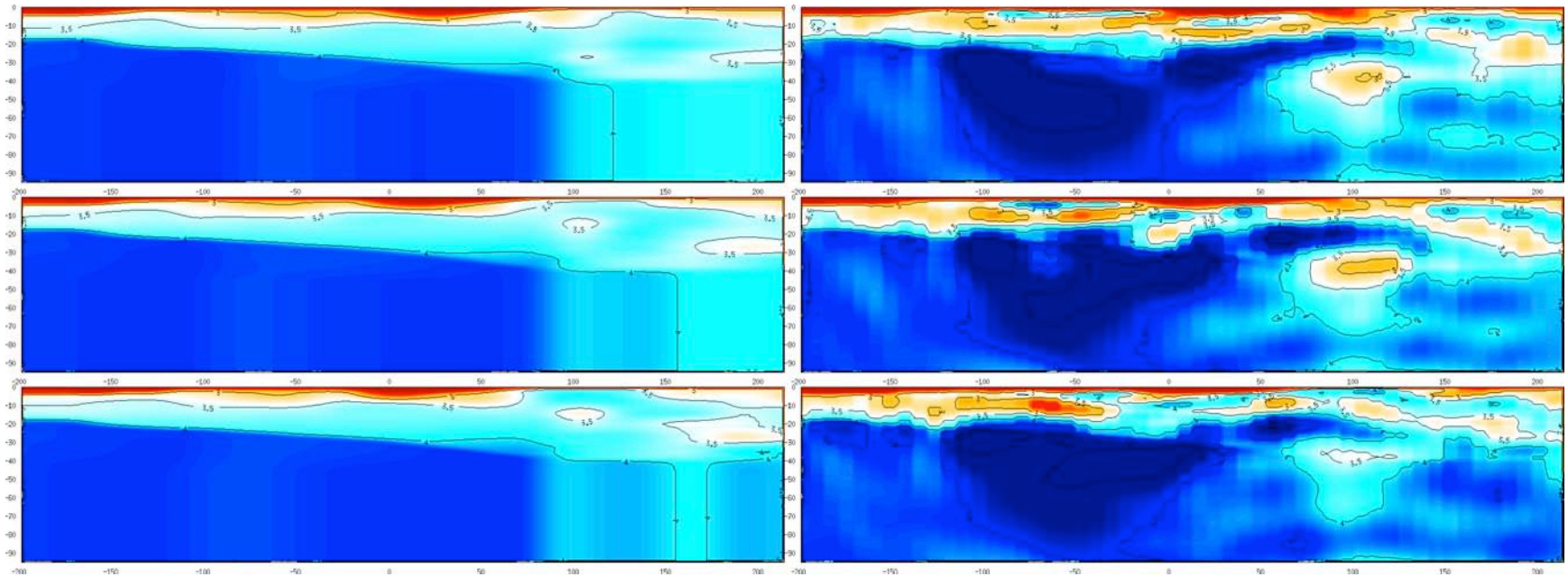

Figure 10. (continued) cross-sections (j)-(l).

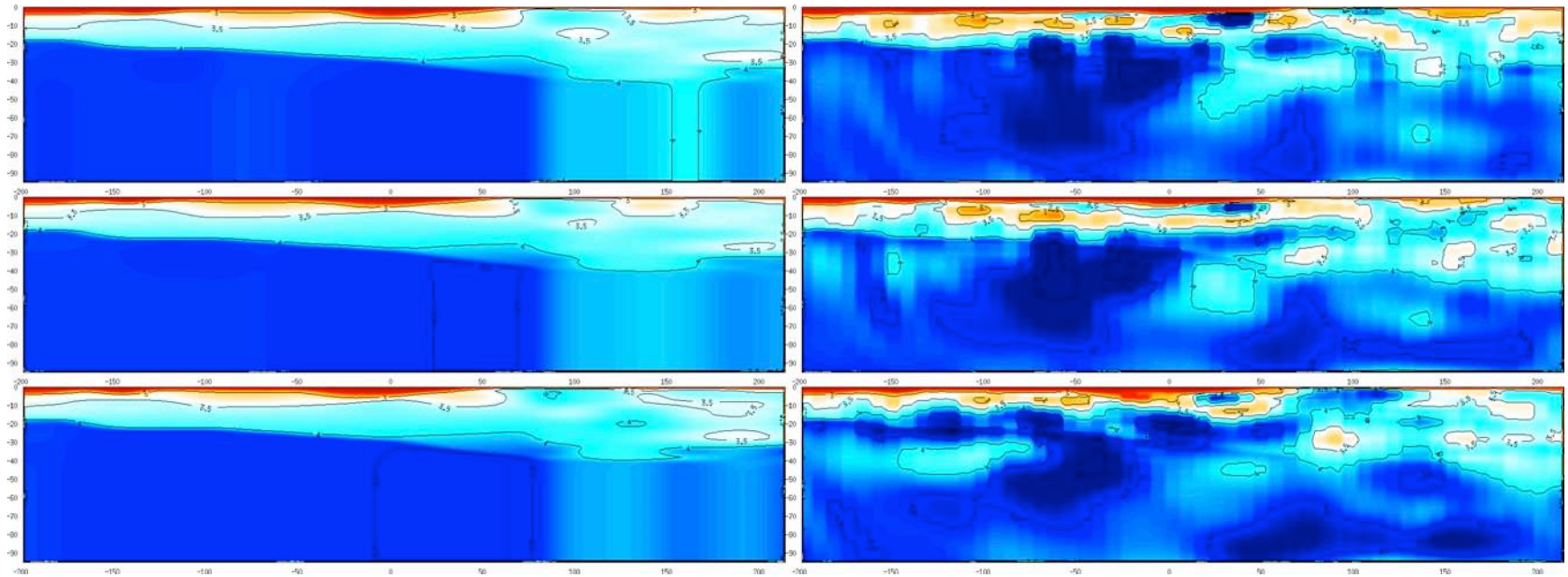

Figure 10. (continued) cross-sections (m)-(o).

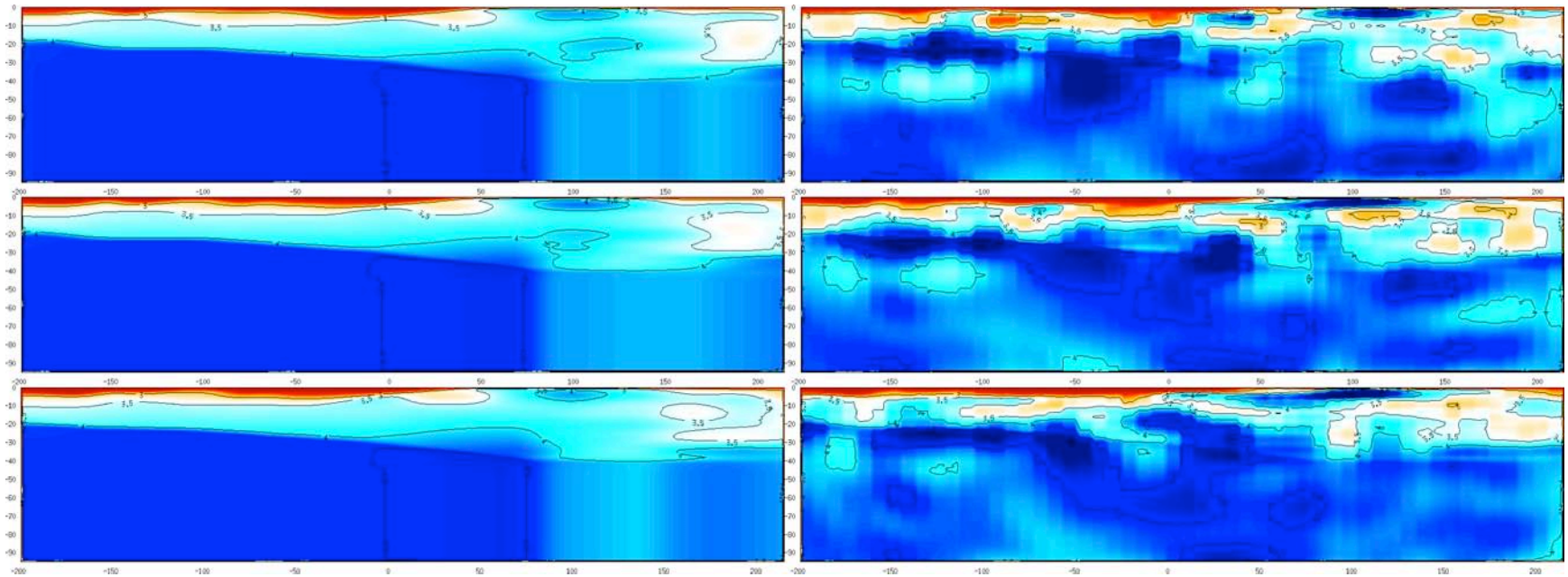

Figure 10. (continued) cross-sections (p)-(r).

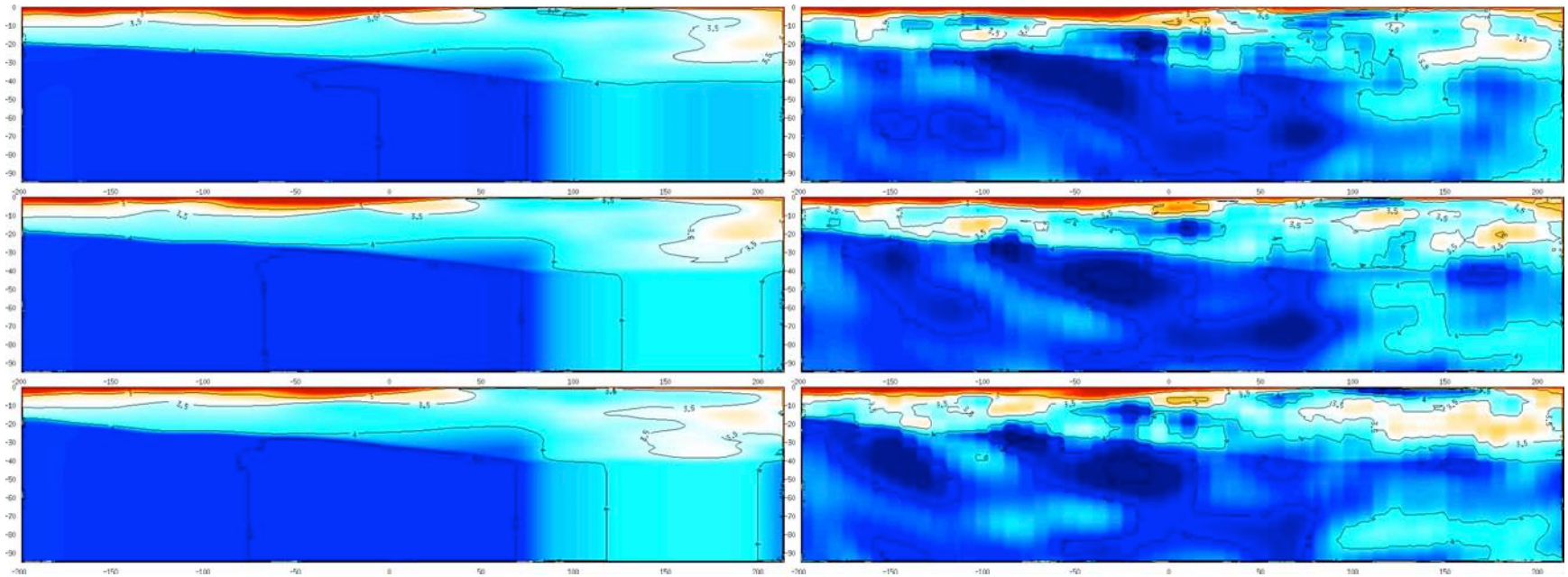

Figure 10. (continued) cross-sections (s)-(u).

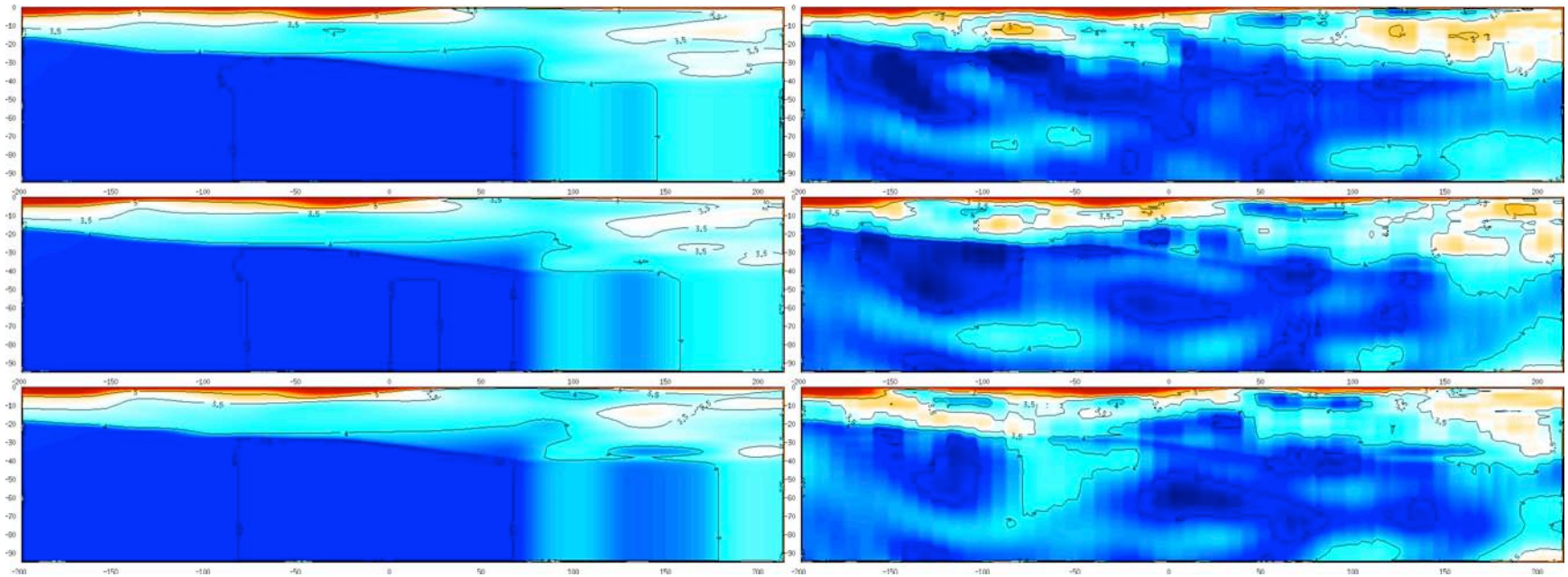

Figure 10. (continued) cross-sections (v)-(x).

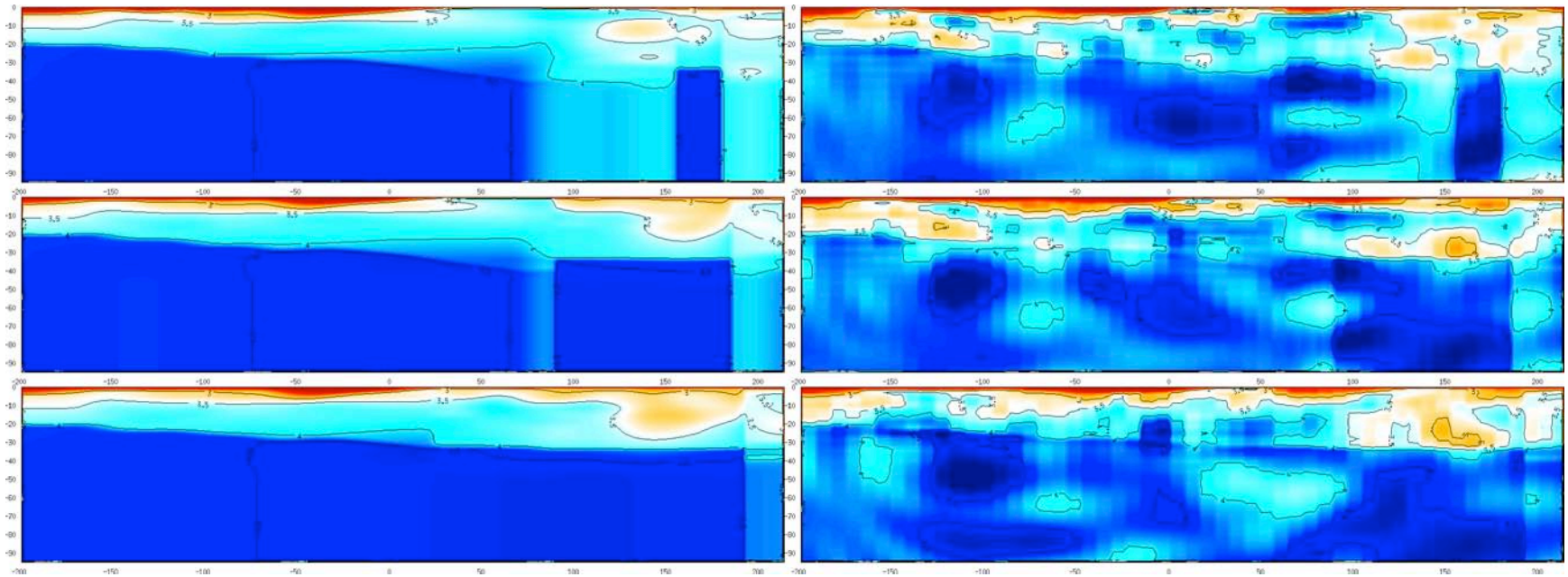

Figure 10. (continued) cross-sections (y)-(aa).

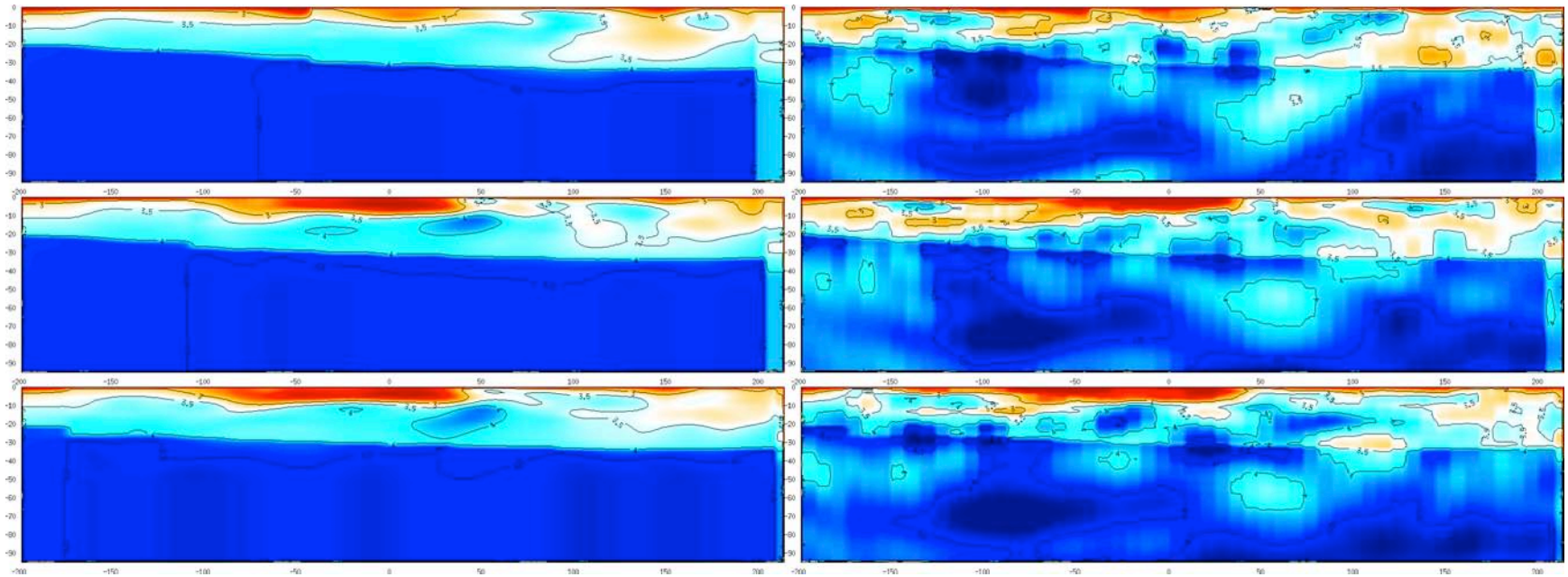

Figure 10. (continued) cross-sections (bb)-(dd).

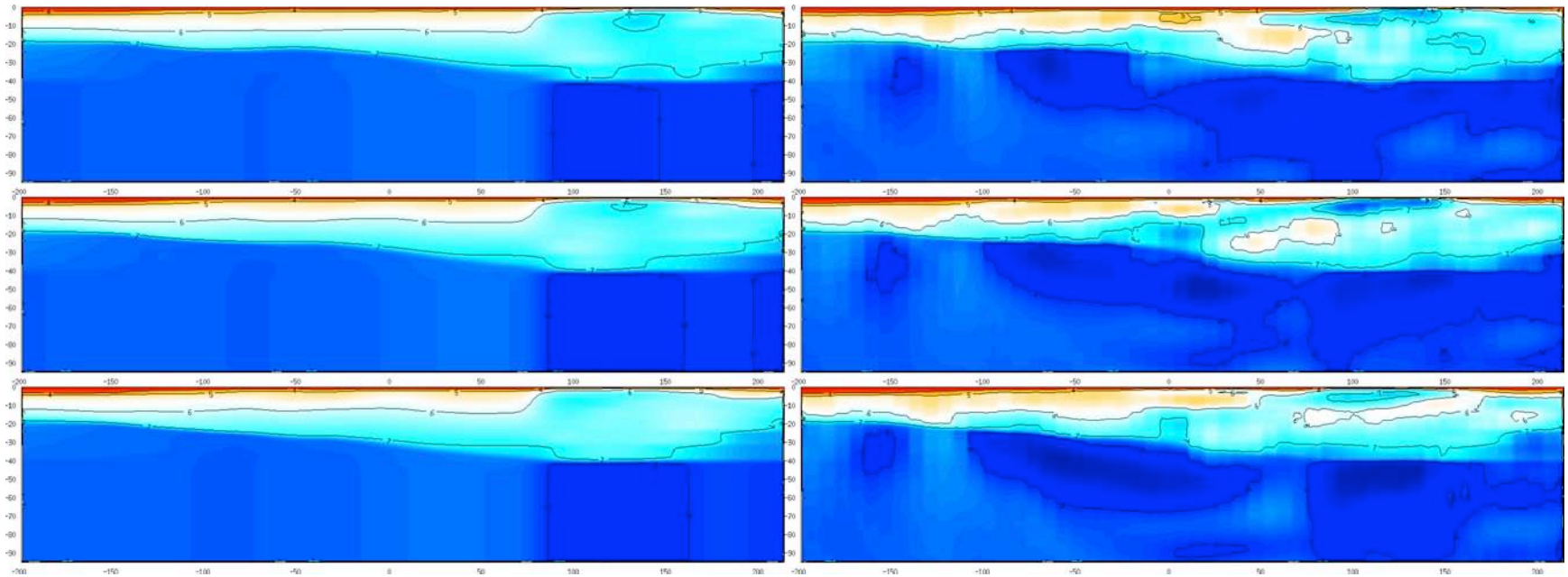

Figure 11. Cross-section views of the Vp model in NCF3D00 (left) and NCF3D09 (right) for cross-sections (a)-(c). Horizontal and vertical dimensions are in km. No vertical exaggeration in all cross-sections.

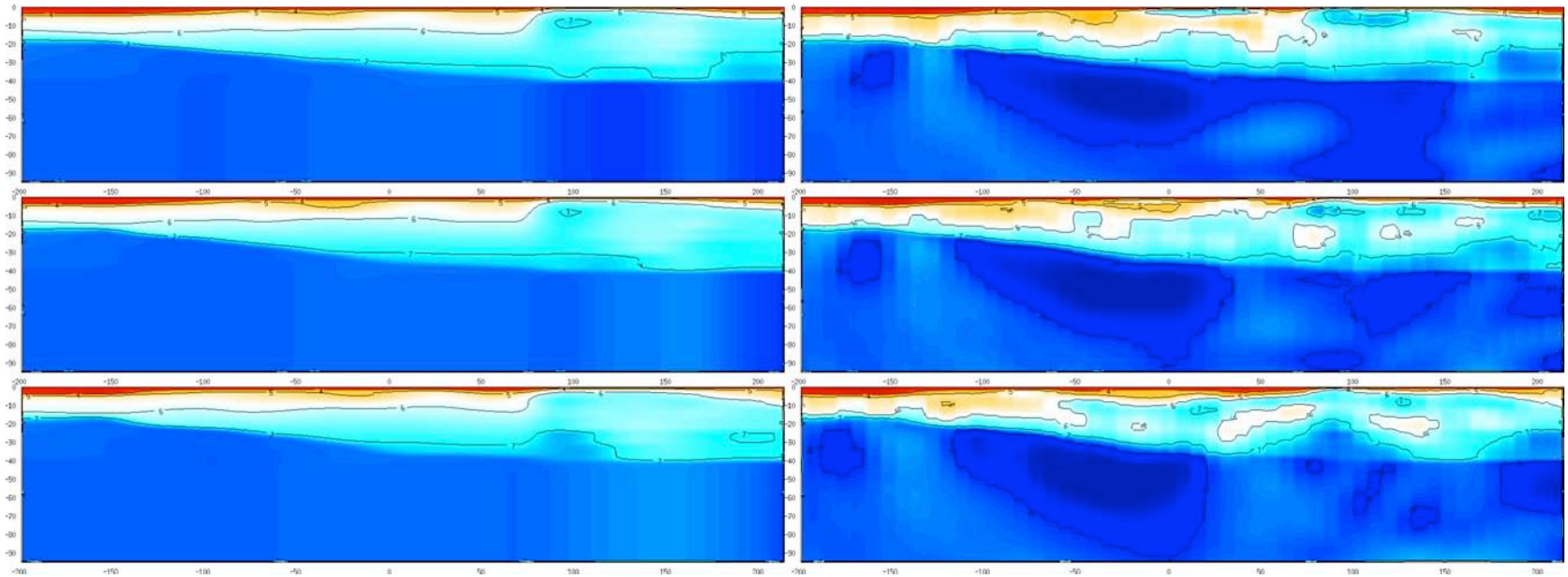

Figure 11. (continued) cross-sections (d)-(f).

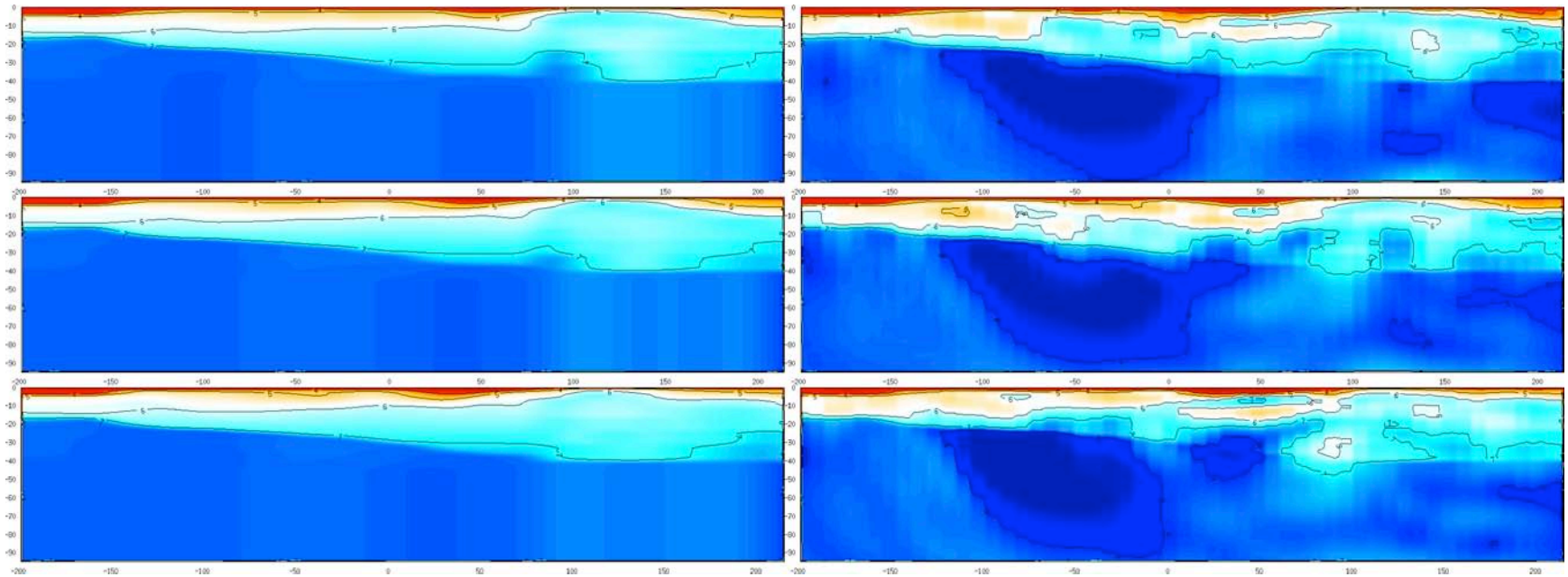

Figure 11. (continued) cross-sections (g)-(i).

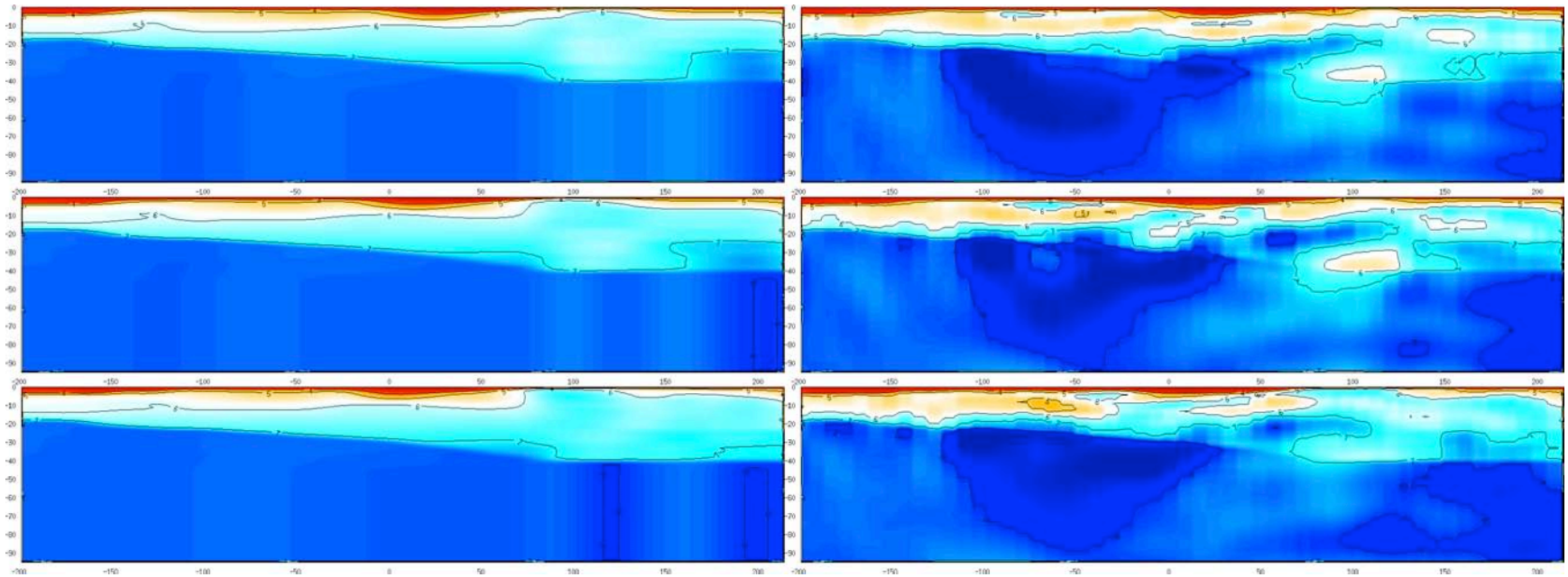

Figure 11. (continued) cross-sections (j)-(l).

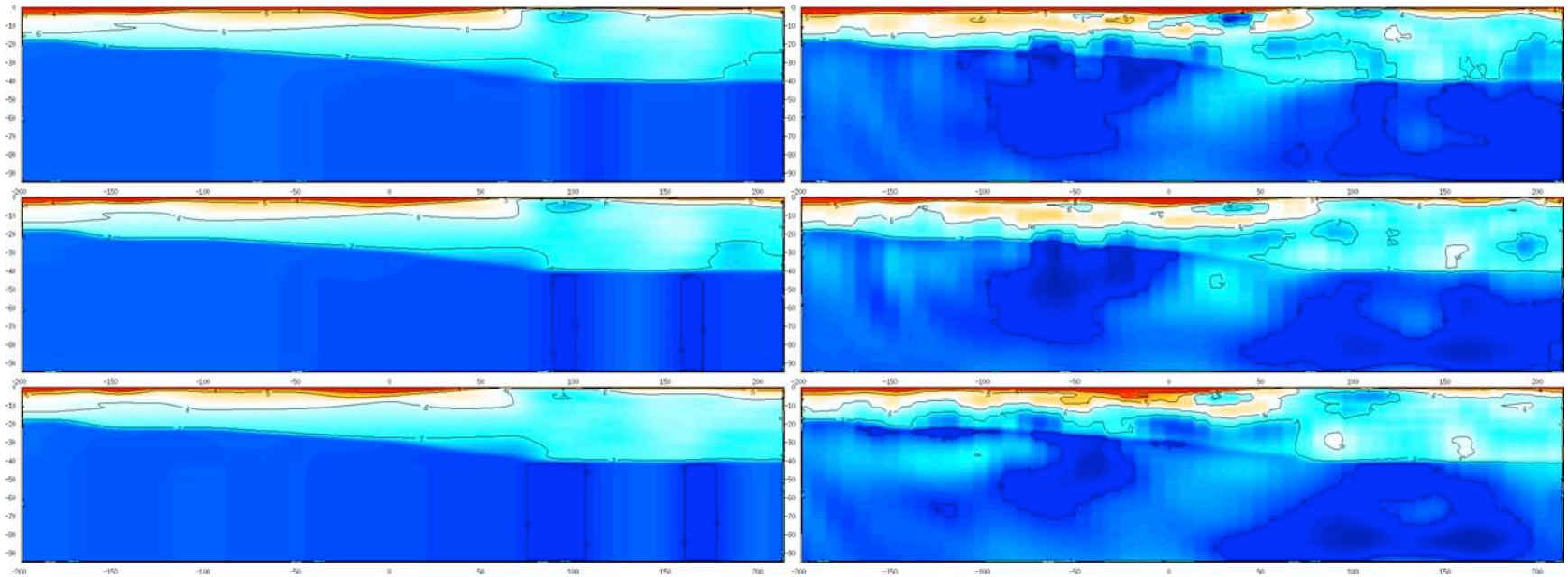

Figure 11. (continued) cross-sections (m)-(o).

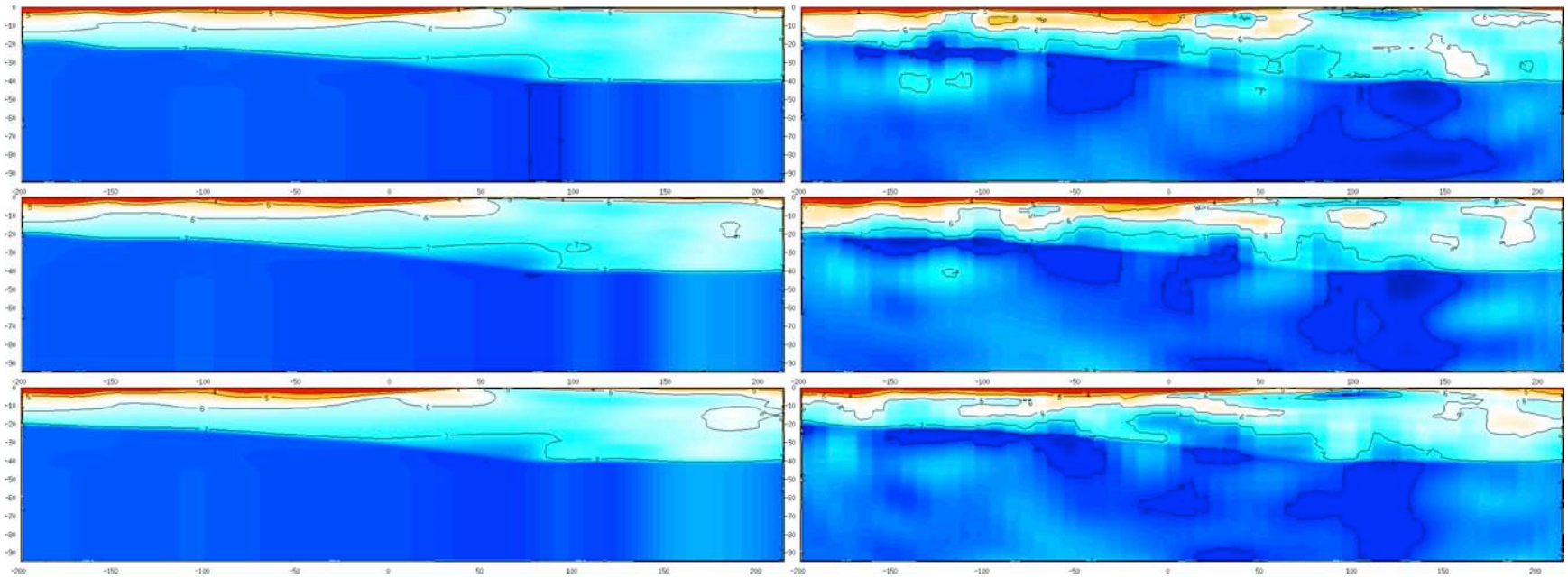

Figure 11. (continued) cross-sections (p)-(r).

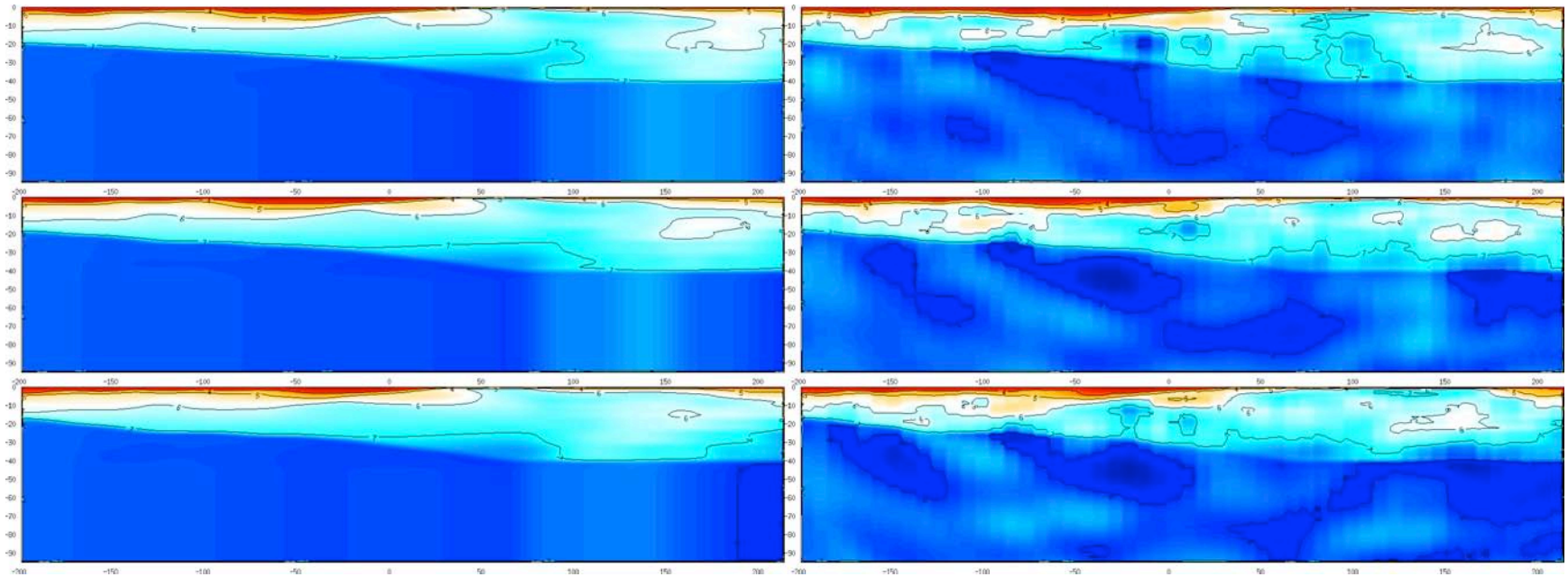

Figure 11. (continued) cross-sections (s)-(u).

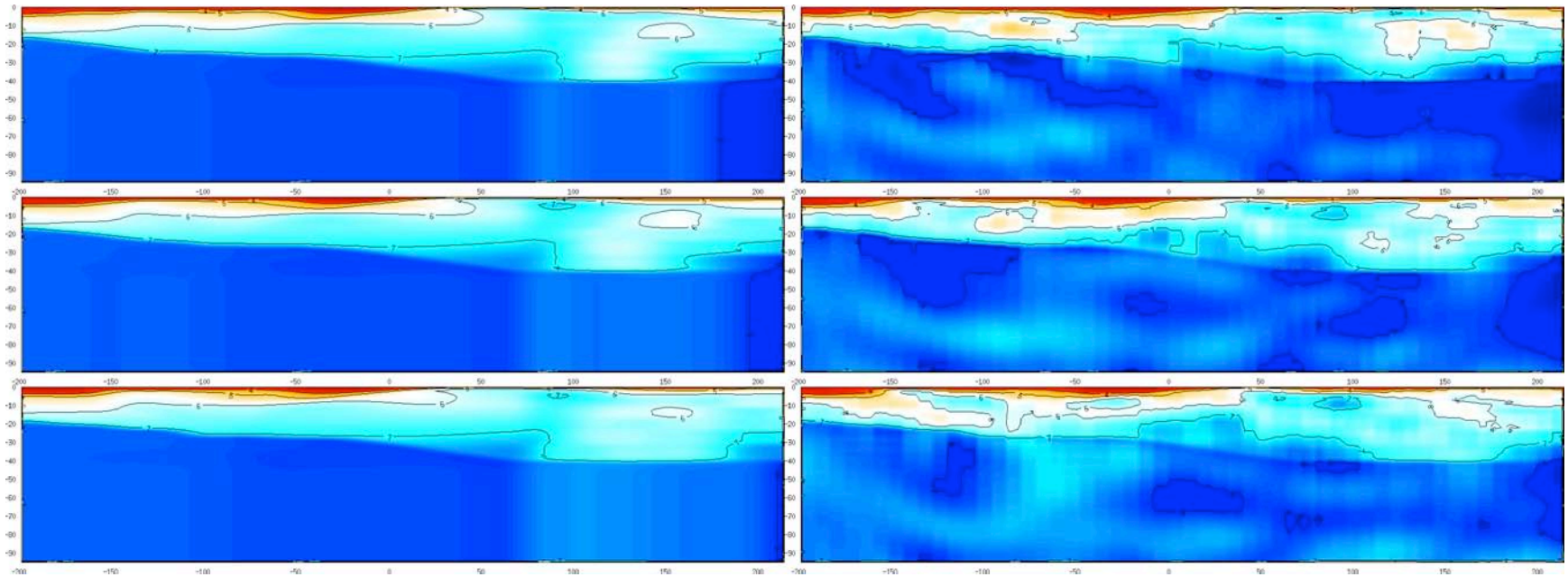

Figure 11. (continued) cross-sections (v)-(x).

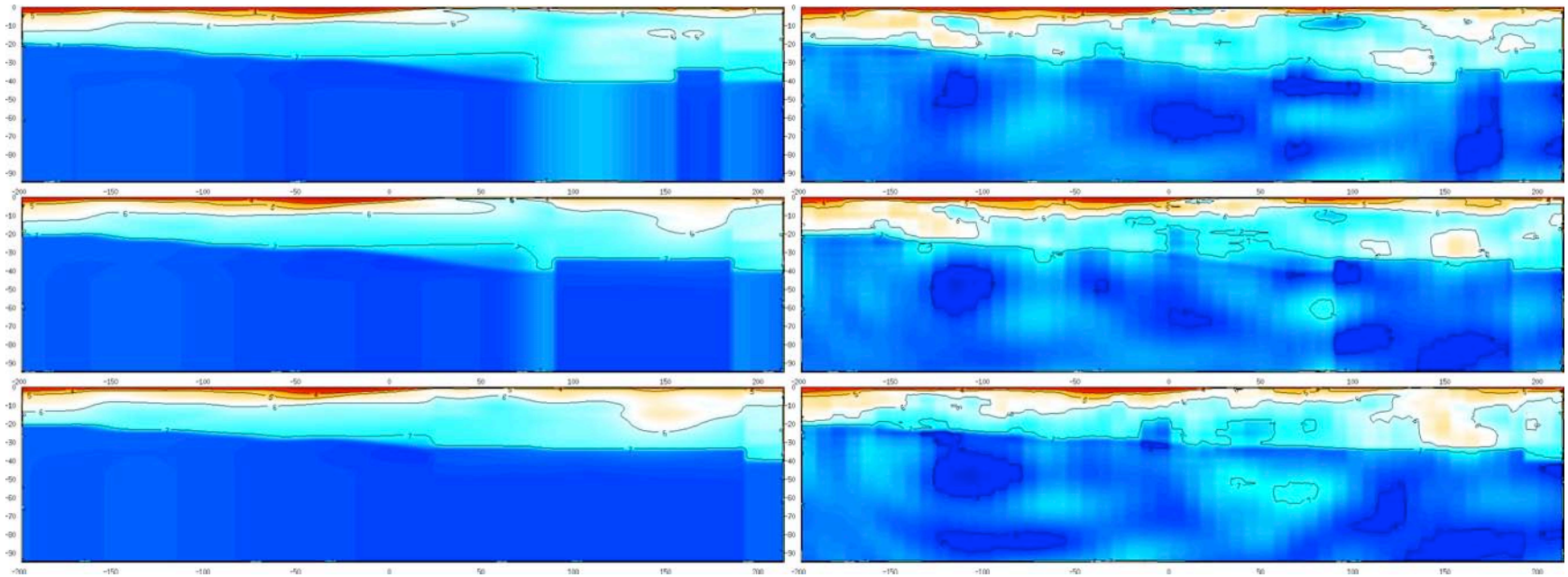

Figure 11. (continued) cross-sections (y)-(aa).

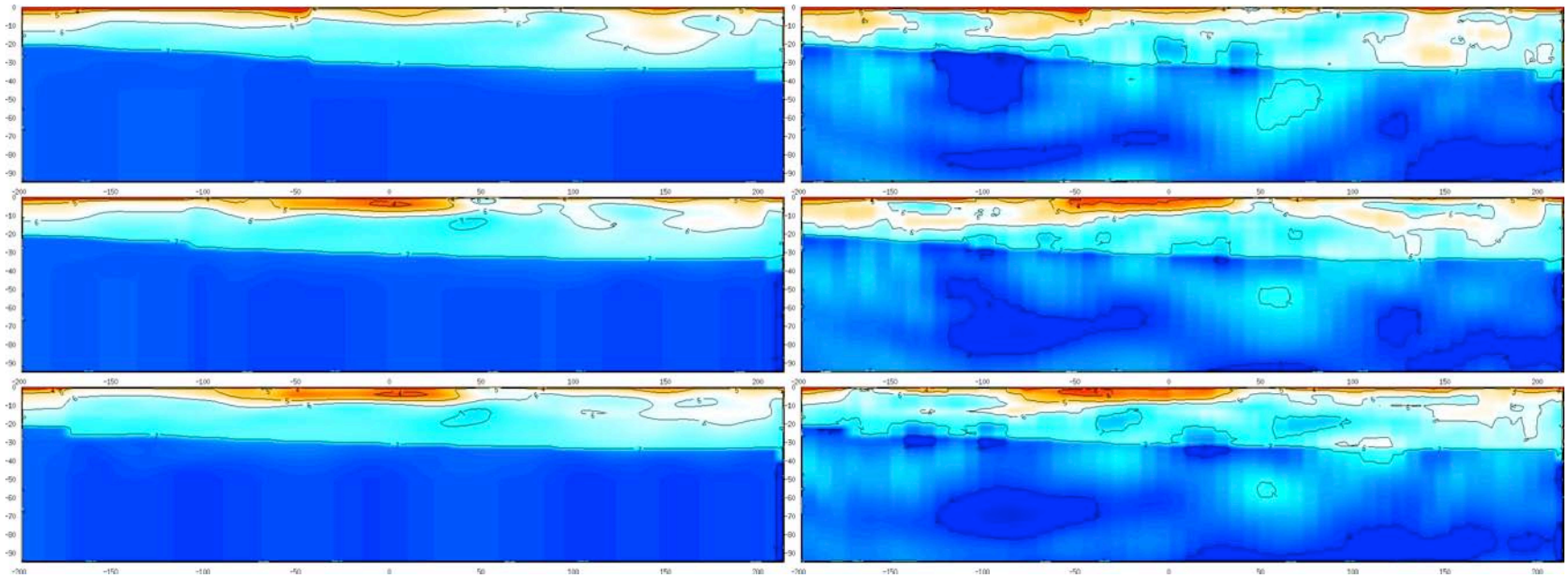

Figure 11. (continued) cross-sections (bb)-(dd).

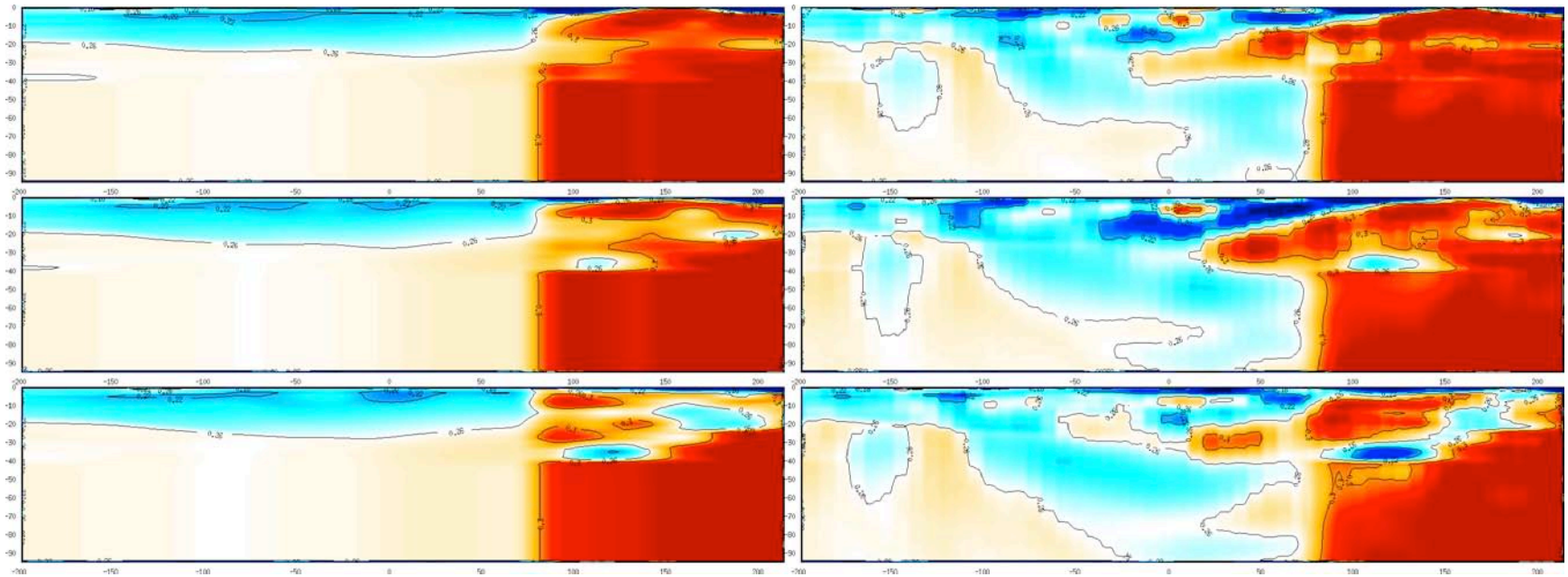

Figure 12. Cross-section views of the Poisson's ratio model in NCF3D00 (left) and NCF3D09 (right) for cross-sections (a)-(c). Horizontal and vertical dimensions are in km. No vertical exaggeration in all cross-sections.

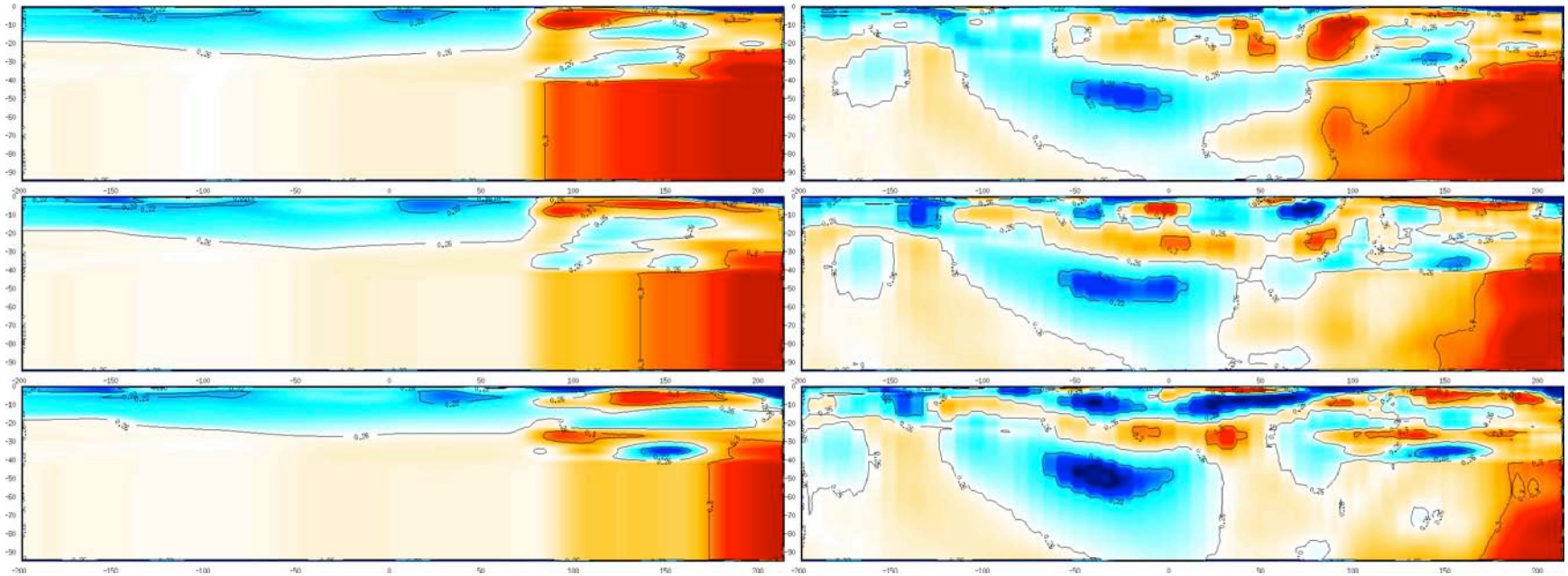

Figure 12. (continued) cross-sections (d)-(f).

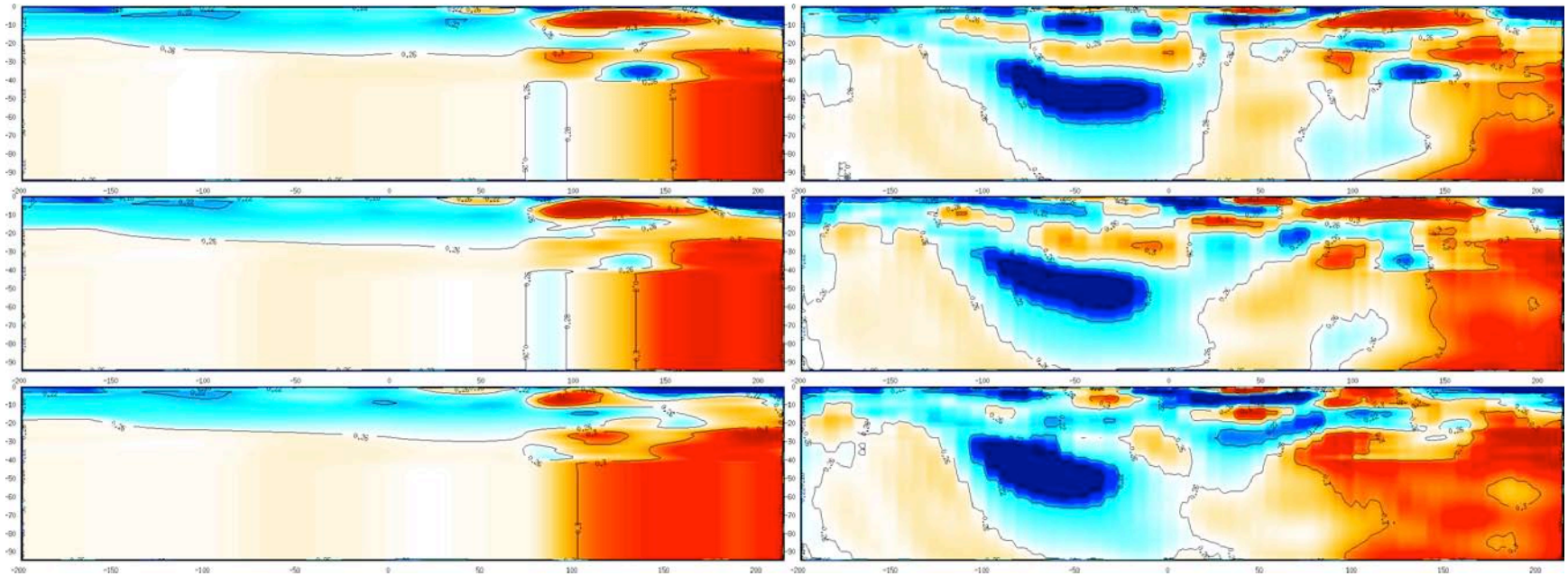

Figure 12. (continued) cross-sections (g)-(i).

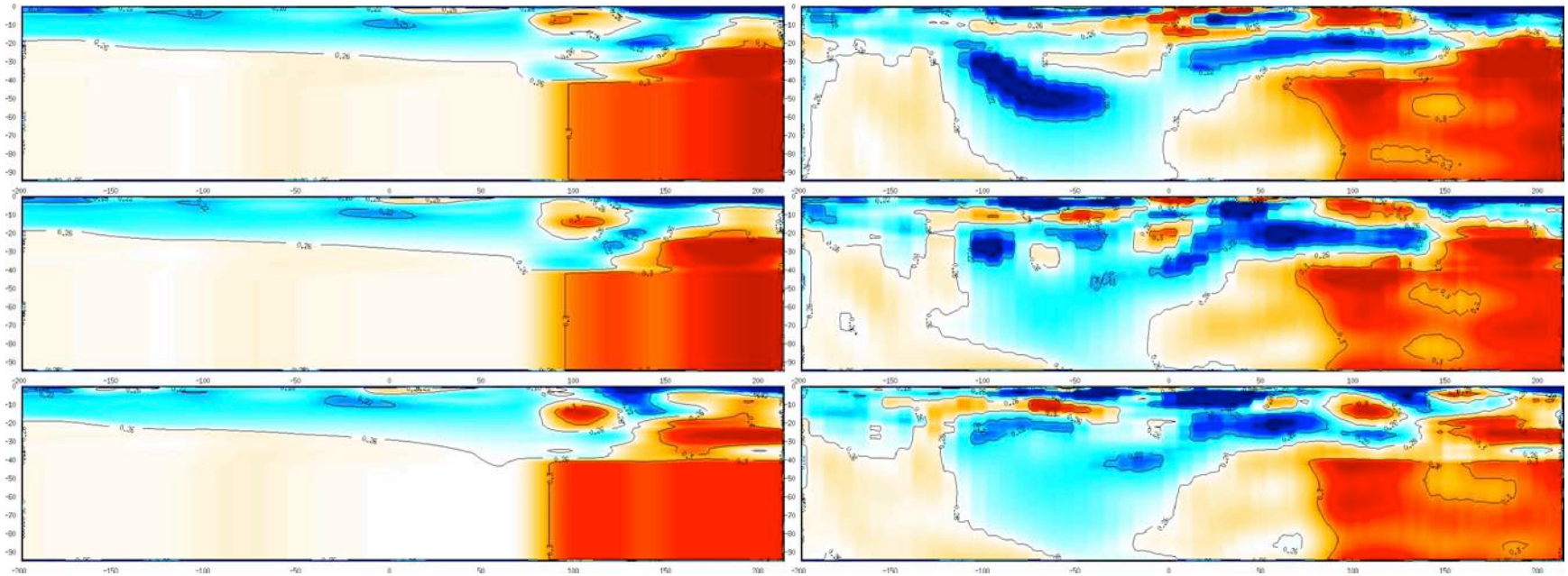

Figure 12. (continued) cross-sections (j)-(l).

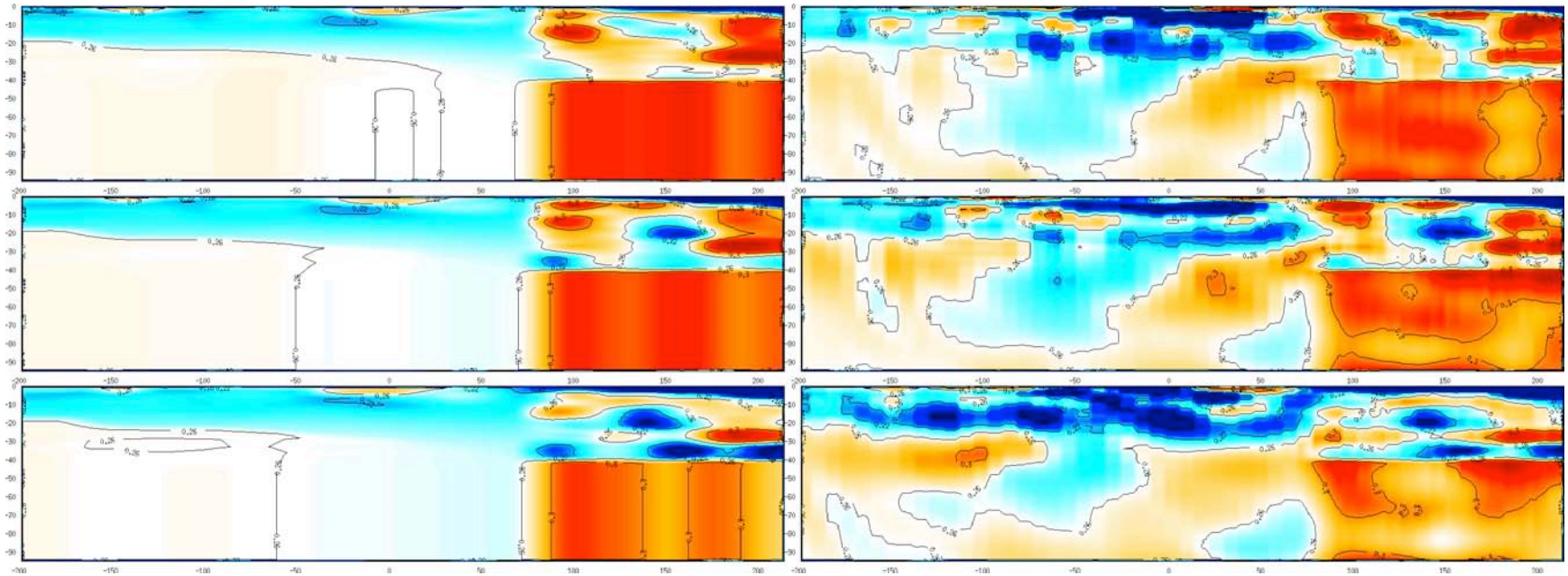

Figure 12. (continued) cross-sections (m)-(o).

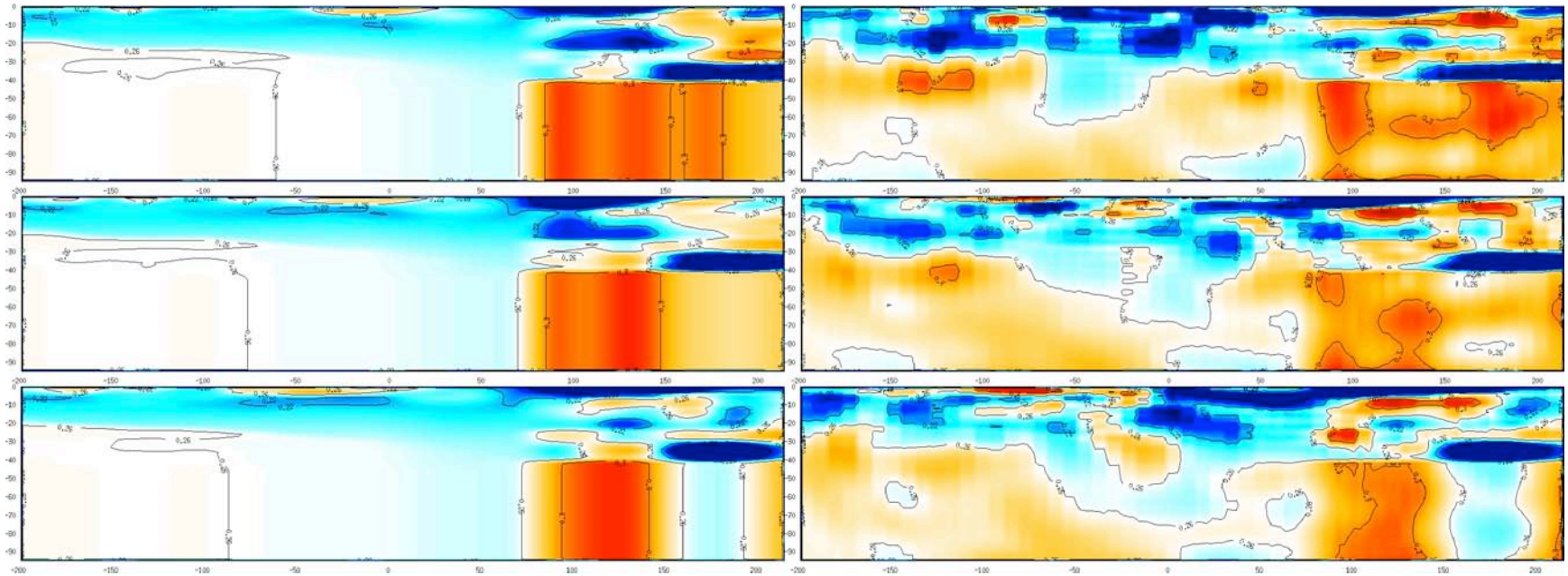

Figure 12. (continued) cross-sections (p)-(r).

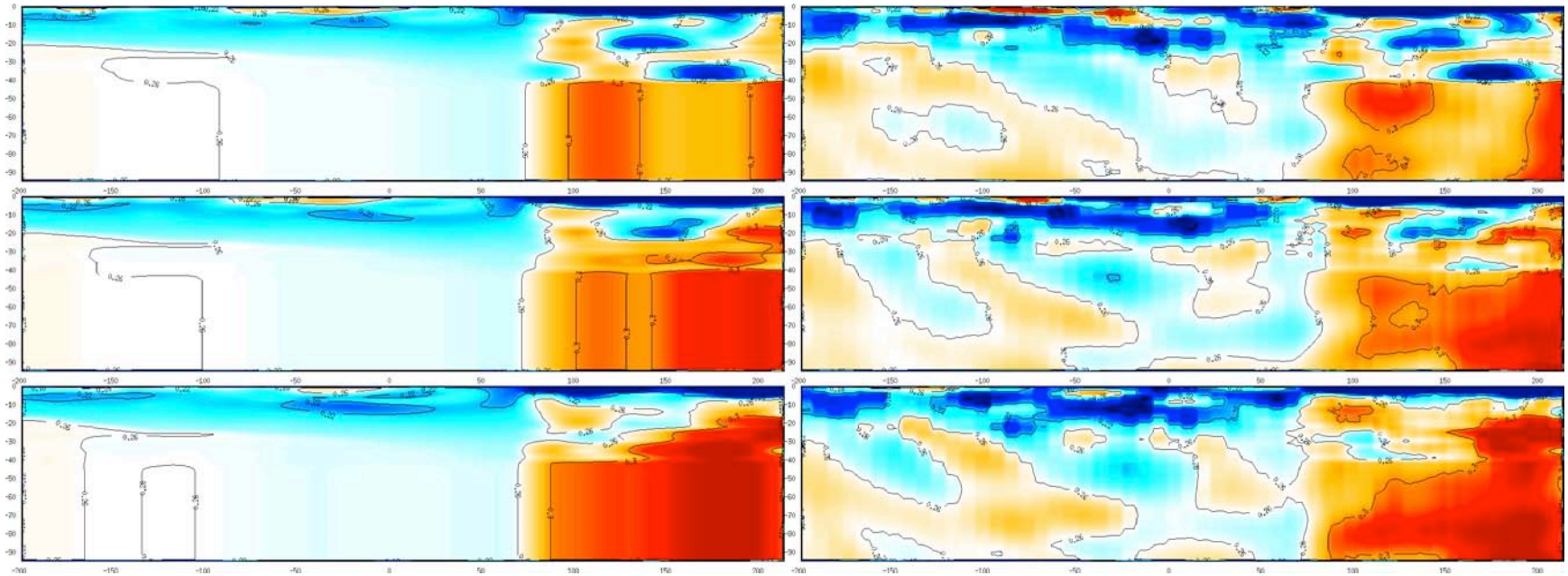

Figure 12. (continued) cross-sections (s)-(u).

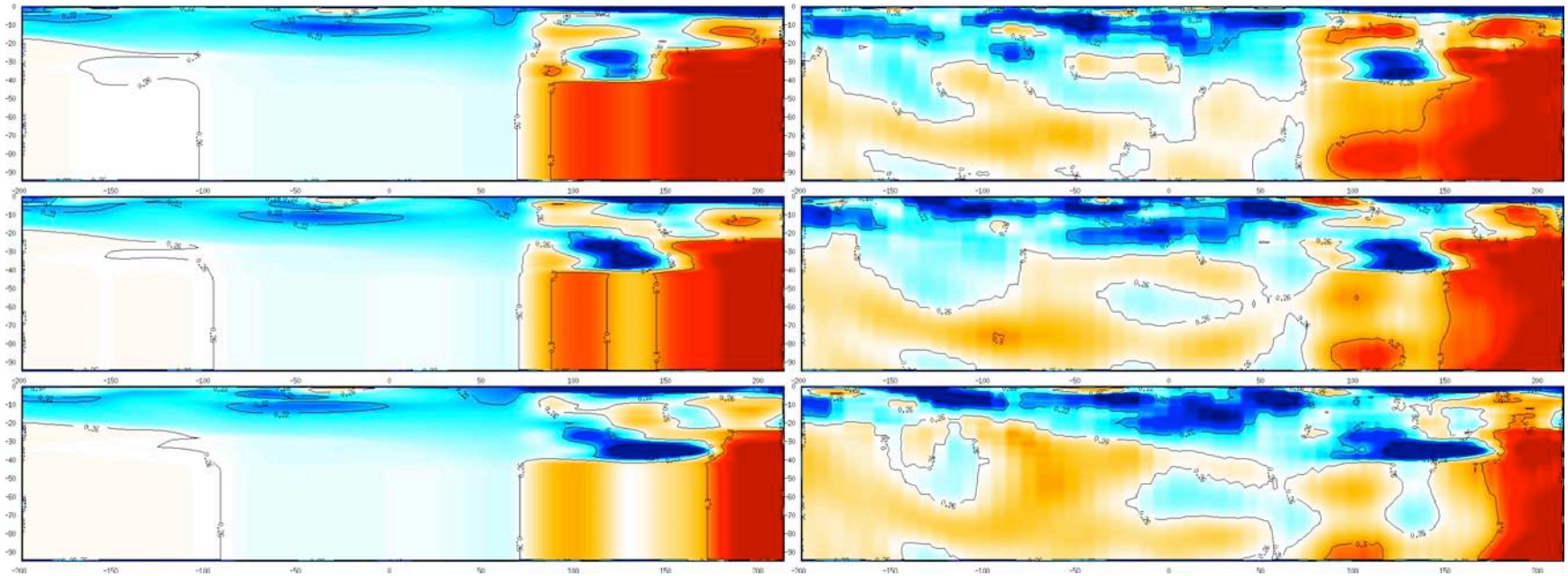

Figure 12. (continued) cross-sections (v)-(x).

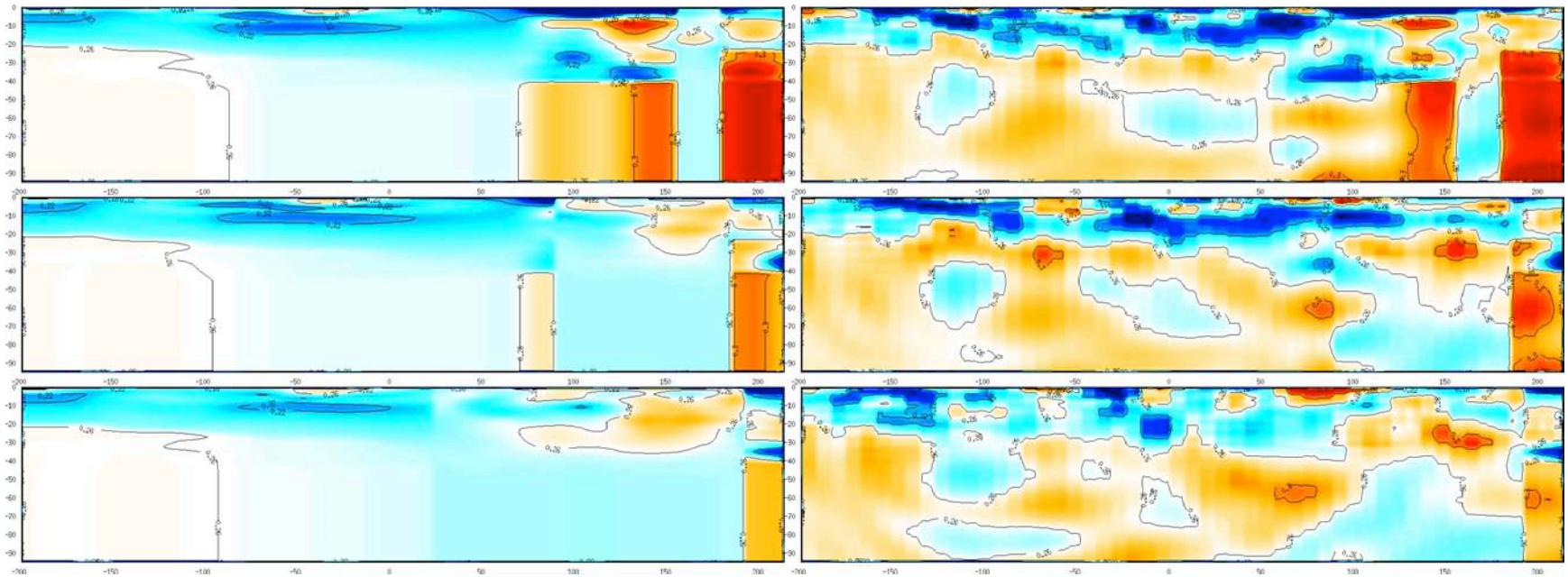

Figure 12. (continued) cross-sections (y)-(aa).

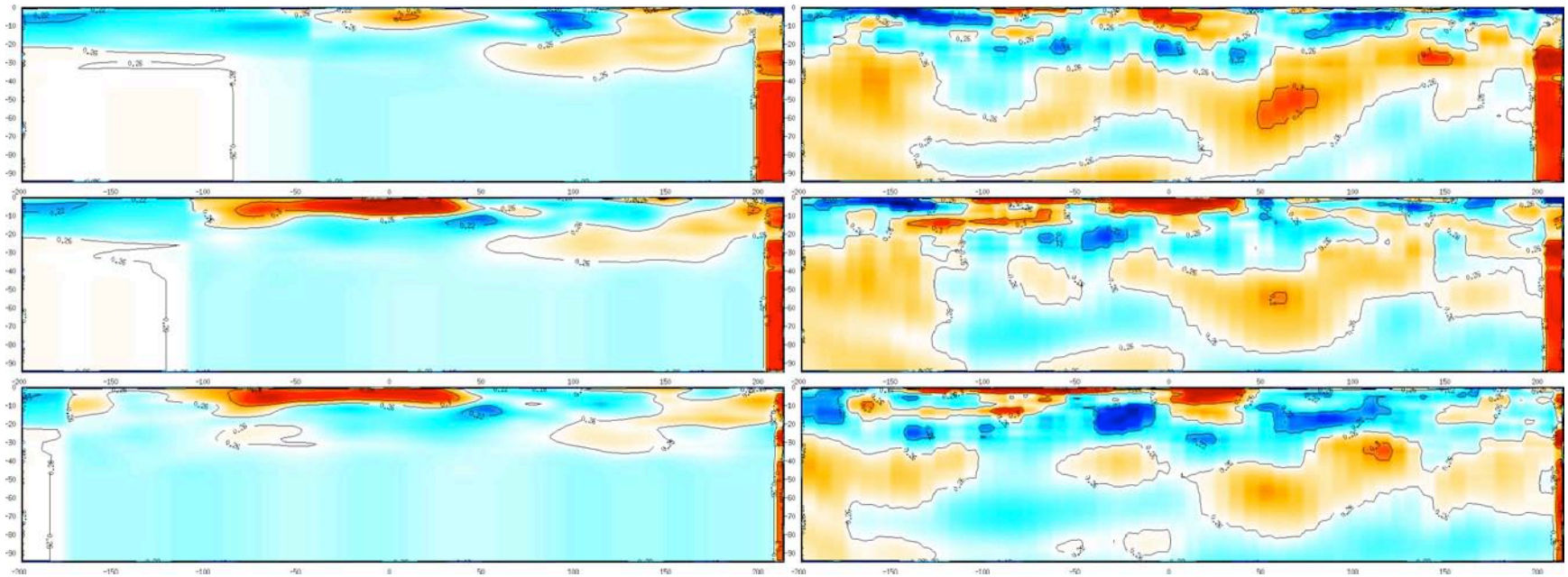

Figure 12. (continued) cross-sections (bb)-(dd).

Reference:

Aagaard, B. (2006). Finite-element simulations of ground motions in the San Francisco Bay Area from large earthquakes on the San Andreas Fault (abstract for the 2006 Seismological Society of American meeting), *Seism. Res. Lett*. 77, 275.

Aagaard, B. T., T. M. Brocher, D. Dolenc, D. Dreger, R. W. Graves, S. Harmsen, S. Hartzell, S. Larsen, and M. L. Zoback (2008a). Ground-motion modeling of the 1906 San Francisco earthquake, part I: Valida-tion using the 1989 Loma Prieta earthquake, *Bull. Seismol. Soc. Am*. 98, no. 2, 989–1011.

Aagaard, B. T., T. M. Brocher, D. Dolenc, D. Dreger, R. W. Graves, S. Harmsen, S. Hartzell, S. Larsen, K. McCandless, S. Nilsson, N. A. Petersson, A. Rodgers, B. Sjögreen, and M. L. Zoback (2008b). Ground-motion modeling of the 1906 San Francisco earthquake, part II: Ground-motion estimates for the 1906 earthquake and sce-nario events, *Bull. Seismol. Soc. Am*. 98, no. 2, 1012–1046.

Bao, H., Bielak, J., Ghattas, O., Kallivokas, L. F., Hallaronb, D. R. O., Shewchukb, J. R., & Xu, J. (1998). Large-scale simulation of elastic wave propagation in heterogeneous media on parallel computers, 7825(97).

Bensen, G. D., Ritzwoller, M. H., Barmin, M. P., Levshin, A. L., Lin, F., Moschetti, M. P. Barmin, A. L. Levshin, F. Lin, M. P. Moschetti, N. M. Shapiro, and Y. Yang (2007). Processing seismic ambient noise data to obtain reliable broad-band surface wave dispersion measurements. *Geophysical Journal International*, *169*(3), 1239-1260.

Berenger, J. (1994). A perfectly matched layer for the absorption of electromagnetic wave. Journal of Computational Physics.

Brocher, T. M., 2005a. Empirical relations between elastic wavespeeds and density in the Earth's crust, *Bulletin Of The Seismological Society Of America*, 95(6), 2081–2092.

Brocher, T. M., 2005b. A Regional View of Urban Sedimentary Basins in Northern California Based on Oil Industry Compressional-Wave Velocity and Density Logs, *Bulletin of the Seismological Society of America*, 95(6), 2093–2114.

Cerveny, V. (2005). *Seismic ray theory*. Cambridge university press.

Chen, P., Jordan, T., & Zhao, L. (2007a). Full three-dimensional tomography: a comparison between the scattering-integral and adjoint-wavefield methods. *Geophysical Journal International* , *170* (1), 175-181.

Chen, P., Zhao, L., & Jordan, T. (2007b). Full 3D tomography for the crustal structure of the Los Angeles region. *Bulletin of the Seismological Society of America* , *97* (4), 1094-1120.

Chen, P., 2011. Full-wave seismic data assimilation: Theoretical background and recent advances, *Pure and Applied Geophysics*, 168(10), 1527–1552.

Chen, P. & Lee, E-J., 2015. Full-3D Seismic Waveform Inversion: Theory, Software and Practice, *Springer*, 511pp.

Dahlen, F., Hung, S., & Nolet, G., 2000. Fréchet kernels for finite-frequency traveltimes-I. Theory, *Geophysical Journal International*, 141, 157–174.

Fichtner, A., B. L. N. Kennett, H. Igel, and H.-P. Bunge (2009), Full seismic waveform tomography for upper-mantle structure in the Australasian region using adjoint methods, *Geophys. J. Int.*, *179*(3), 1703–1725, doi:10.1111/j.1365-246X.2009.04368.x.

Fichtner, A. (2011). Full seismic waveform modelling and inversion . Berlin/Heidelberg: Springer.

Field, E. H., 2007. A Summary of Previous Working Groups on California Earthquake Probabilities. *Bulletin of the Seismological Society of America*, Vol. 97, No. 4, pp. 1033–1053, doi: 10.1785/0120060048

Frankel, A., D. Carver, E. Cranswick, T. Bice, R. Sell, and S. Hanson (2001). Observations of basin ground motions from a dense seismic array in San Jose, California, *Bull. Seism. Soc. Am.* **91**, 1-12.

Graves, R. W., 1996. Simulating seismic wave propagation in 3d elastic media using staggered-grid finite-differences, *Bulletin of the Seismological Society of America*, 86(4), 1091–1106.

Hartzell, S., E. Cranswick, A. Frankel, D. Carver, and M. Meremonte (1997). Variability of site response in the Los Angeles urban area, *Bull. Seism. Soc. Am.* **87**, 1377-1400.

Iwata, T., K. Hatayama, H. Kawase, and K. Irikura (1996). Site amplification of ground motions during aftershocks of the 1995 Hyogo-ken Nanbu earthquake in severely damaged zone-Array observation of ground motions in Higashinada Ward, Kobe City, Japan, *J. Phys. Earth* **44**, 553-561.

Käser, M., Dumbser, M., de la Puente, J., & Igel, H., 2007. An arbitrary high-order Discontinuous Galerkin method for elastic waves on unstructured meshes - III. Viscoelastic attenuation, *Geophysical Journal International*, 168, 224–242.

Kawase, H. (1996). The cause of the damage belt in Kobe: “The basin-edge effect”, constructive interference of the direct S-wave with the basin-induced diffracted/Raleigh waves, *Seism. Res. Lett.* **67**, (5), 25-34.

Komatitsch, D. & Tromp, J., 2002. Spectral-element simulations of global seismic wave propagation – I Validation, *Geophysical Journal International*, 149(2), 390–412.

Lee, E. J., Chen, P., Jordan, T. H., Maechling, P. B., Denolle, M. A., & Beroza, G. C. (2014). Full-3-D tomography for crustal structure in Southern California based on the scattering-integral and the adjoint-wavefield methods. *Journal of Geophysical Research: Solid Earth*, *119*(8), 6421-6451.

Lee, E. J., Chen, P., & Jordan, T. H. (2014). Testing waveform predictions of 3D velocity models against two recent Los Angeles earthquakes. *Seismological Research Letters*, *85*(6), 1275-1284.

Lee, E. J., Chen, P., Jordan, T. H., & Wang, L. (2011). Rapid full-wave centroid moment tensor (CMT) inversion in a three-dimensional earth structure model for earthquakes in Southern California. *Geophysical Journal International*, *186*(1), 311-330.

Lee, E. J., Huang, H., Dennis, J. M., Chen, P., & Wang, L. (2013). An optimized parallel LSQR algorithm for seismic tomography. *Computers & Geosciences*, *61*, 184-197.

Lin, G., Thurber, C. H., Zhang, H., Hauksson, E., Shearer, P. M., Waldhauser, F., Brocher, T. M., 2008. Compressional and shear-wave velocity versus depth relations for common rock types in northern California, *Bulletin Of The Seismological Society Of America*, 98(2), 950–968.

Lindstrom, P., Chen, P. and Lee, E-J., Reducing disk storage of full-3D seismic tomography (F3DT) through lossy compression, in preparation.

Liu, Q., and J. Tromp (2006), Finite-Frequency Kernels Based on Adjoint Methods, *Bull. Seismol. Soc. Am.*, *96*(6), 2383–2397, doi:10.1785/0120060041.

Olsen, K. B., 1994. *Simulation of three-dimensional wave propagation in the Salt Lake Basin*, Ph.D. thesis, University of Utah, Salt Lake City, UT.

Olsen, K. B. and R. J. Archuleta (1996). Three-dimensional simulation of earthquakes on the Los Angeles fault system, Bull. Seism. Soc. Am., 86, 575-596.

Pitarka, A., K. Irikura, T. Iwata, and T. Kagawa (1996). Basin structure effects in the Kobe area inferred from the modeling of ground motions from two aftershocks of the January 17, 1995 Hyogo-ken Nanbu earthquake, *J. Phys. Earth* **44**, 563-576.

Tape, C., Q. Liu, A. Maggi, and J. Tromp (2009), Adjoint Tomography of the Southern California Crust, *Science*, *325*(5943), 988–992, doi:10.1126/science.1175298.

Tarantola, A., 1988. Theoretical background for the inversion of seismic waveforms including elasticity and attenuation, *Pure and Applied Geophysics*, 128(1-2), 365–399.

Thurber, C., Zhang, H., Brocher, T., & Langenheim, V. (2009). Regional three-dimensional seismic velocity model of the crust and uppermost mantle of northern California. *Journal of Geophysical Research: Solid Earth (1978–2012)*, *114*(B1).

Triebel, H. (1978). *Interpolation theory, function spaces, differential operators*. North Holland.

Tromp, J., Tape, C., & Liu, Q., 2005. Seismic tomography, adjoint methods, time reversal and banana-doughnut kernels, *Geophysical Journal International*, 160(1), 195–216.

Wald, D. J., and R. W. Graves (1998). The seismic response of the Los Angeles Basin, California, *Bull. Seism. Soc. Am.* **88**, 337-356.

Working Group on California Earthquake Probabilities (WGCEP) (2003). Earthquake probabilities in the San Francisco Bay Region: 2002– 2031, U.S. *Geol. Surv. Open-File Rept. 03-214*.

Xu, Z., P. Chen, and Y. Chen (2013), Sensitivity Kernel for the Weighted Norm of the Frequency-Dependent Phase Correlation, *Pure Appl. Geophys.*, *170*(3), 353–371, doi:10.1007/s00024-012-0507-3.

Zhao, L., Chen, P., & Jordan, T. (2006). Strain Green's Tensors, Reciprocity, and Their Applications to Seismic Source and Structure Studies. *Bulletin of the Seismological Society of America* Vol. 96, No. 5, pp. 1753–1763, doi: 10.1785/0120050253.

Zhao, L., Jordan, T., Olsen, K., & Chen, P. (2005). Frechet Kernels for Imaging Regional Earth Structure Based on Three-Dimensional Reference Models. *Bulletin of the Seismological Society of America* Vol. 95, No. 6, pp. 2066–2080 doi: 10.1785/0120050081.